ANKARA YILDIRIM BEYAZIT UNIVERSITY GRADUATE SCHOOL OF NATURAL AND APPLIED SCIENCES

FABRICATION AND ANALYSIS OF A DYE SENSITIZED SOLAR CELL: HYDROTHERMALLY GROWN HYBRID PHOTOANODE AND OPAQUE PT COUNTER ELECTRODE

Ph.D. Thesis by

Aycan ATLI

Department of Energy Systems Engineering

January, 2023

ANKARA

FABRICATION AND ANALYSIS OF A DYE SENSITIZED SOLAR CELL: HYDROTHERMALLY GROWN HYBRID PHOTOANODE AND OPAQUE PT COUNTER ELECTRODE

A Thesis Submitted to

The Graduate School of Natural and Applied Sciences of

Ankara Yildirim Beyazit University in Partial Fulfillment of the Requirements for the Degree of Doctor of Philosophy in Energy Systems Engineering, Department of Energy Systems Engineering

by

Aycan ATLI

January, 2023

ANKARA

Ph.D. THESIS EXAMINATION RESULT FORM

We have read the thesis entitled "**FABRICATION AND ANALYSIS OF A DYE SENSITIZED SOLAR CELL: HYDROTHERMALLY GROWN HYBRID PHOTOANODE AND OPAQUE PT COUNTER ELECTRODE**" completed by **AYCAN ATLI** under supervision of **PROF. DR. ABDULLAH YILDIZ** and we certify that in our opinion it is fully adequate, in scope and in quality, as a thesis for the degree of Doctor of Philosophy.

Prof. Dr. Abdullah YILDIZ

Supervisor

Prof. Dr. FAHRETTİN GÖKTAŞ

Thesis Committee Member

Assoc. Prof. Dr. SELÇUK YERCİ

Thesis Committee Member

Prof. Dr. SEFER BORA LİŞESİVDİN

Examining Committee Member

Prof. Dr. ŞİNASİ BARIŞ EMRE

Examining Committee Member

Prof. Dr. Sadettin ORHAN

Director

Graduate School of Natural and Applied Sciences

ETHICAL DECLARATION

I hereby declare that, in this thesis which has been prepared in accordance with the Thesis Writing Manual of Graduate School of Natural and Applied Sciences,

- All data, information and documents are obtained in the framework of academic and ethical rules,
- All information, documents and assessments are presented in accordance with scientific ethics and morals,
- All the materials that have been utilized are fully cited and referenced,
- No change has been made on the utilized materials,
- All the works presented are original,

and in any contrary case of above statements, I accept to renounce all my legal rights.

Date: 2023, January 27 **Signature: _____**

Name & Surname: Aycan ATLI

ACKNOWLEDGEMENTS

I dedicate my deepest thanks to my supervisor, Prof. Dr. Abdullah YILDIZ for his advices, patience, great insight through the development and completion of this dissertation. Working with his research group, I had the chance to gain a multidisciplinary understanding of thinking that included chemistry, physics, materials science and engineering. Prof. YILDIZ's office door was always open if I needed assistance or had questions about my research. His vision, and work ethic have always been an inspiration for me to overcome difficulties in research and life. Through my entire life, I will follow the advice he gave me throughout his mentoring. In addition to my supervisor, I would like to thank the rest of my thesis committee members: Prof. Dr. Fahrettin GÖKTAŞ, Assoc. Prof. Dr. Selçuk YERCİ, Prof. Dr. Sefer Bora LİŞESİVDİN, and Prof. Dr. Şinasi Barış EMRE for their encouragement and insightful comments. Additionally, I want to thank Ankara Yıldırım Beyazıt University, Department of Material Engineering, for their support with the XRD measurement.

I am also thankful to all my friends from laboratory especially Dr. Abdullah ATILGAN, Dr. Kenan ÖZEL, Yusuf YILDIZ, and Esma ATILGAN for their support and for numerous helpful discussions on topics during my thesis work.

Last but not least, I would like to express my very profound gratitude to my parents, my partner İbrahim and my lovely children Ömer and Defne for providing me with unfailing support and continuous encouragement through the process of researching and writing of this thesis. This thesis would not have been completed without them.

Thank you.

2023, January **Aycan ATLI**

FABRICATION AND ANALYSIS OF A DYE SENSITIZED SOLAR CELL: HYDROTHERMALLY GROWN HYBRID PHOTOANODE AND OPAQUE PT COUNTER ELECTRODE

ABSTRACT

A dye-sensitized solar cells is a low-cost solar cell with the advantages of a simple fabrication process and low toxicity. Titanium dioxide and Platinum are the leading actors as photoanode and counter electrodes that come to mind first when dye-sensitized solar cells is mentioned. In this study, different methods including chemical bath deposition, hydrothermal growing, and spin coating methods have been applied successfully to obtain counter electrode and photoanode components. Firstly, the Platinum counter electrode was coated with two different coating methods such as chemical bath and spin coating. The obtained efficiency values are 5.06 percent (R_{ct}, 0.89 $ohm.cm^2$) and 4.31 percent (R_{ct}, 1.44 $ohm.cm^2$), respectively. The difference can be attributed to increased catalytic activity of the Pt films. Then, a hybrid photoanode was prepared by hydrothermal reaction and spin coating. In this stage, the nanoparticles and hydrothermally grown metal oxide nanorod arrays were combined to improve the efficiency of dye-sensitized solar cells and called as hybrid device. The experimental results showed that the efficiency of a hybrid device (5.58 percent). consisting of nanoparticles and nanorods is higher than the one consisting only of nanoparticles (4.95 percent) and nanorods (1.04 percent). The efficiency of cell is improved using hydrothermal techniques to maximize the amount of light absorption and also lower the recombination when light is incident on the cell.

In conclusion, dye-sensitized solar cells are a promising renewable energy technology with great potential for reducing the production cost and increasing the efficiency of solar cells. With continued research and development, dye-sensitized solar cells may eventually become a candidate of the most cost-effective solar cells available on the market.

Keywords: Dye-sensitized solar cell, titanium dioxide, platinum, seed layer, hydrothermal, hybrid solar cell.

BOYA DUYARLI BİR GÜNEŞ PİLİNİN ÜRETİMİ VE ANALİZİ: HİDROTERMAL OLARAK BÜYÜTÜLMÜŞ HİBRİT FOTOANOT VE OPAK PT KARŞIT ELEKTROT

ÖZ

En umut verici yenilenebilir enerji teknolojilerinden biri, boyaya duyarlı güneş pilleridir. Bir boyaya duyarlı güneş pili, basit bir üretim süreci ve düşük toksisite avantajlarına sahip düşük maliyetli bir güneş pilidir. titanyum dioksit ve platin, bu konuda ilk akla gelen fotoanot ve karşı elektrot olarak başrol oyuncularıdır. Bu çalışmada, karşı elektrot ve fotoanot bileşenleri elde etmek için kimyasal banyo biriktirme, hidrotermal büyütme ve döndürmeli kaplama yöntemlerini içeren farklı yöntemler başarıyla uygulanmıştır. İlk olarak Pt karşı elektrot kimyasal banyo ve spin kaplama olmak üzere iki farklı kaplama yöntemi ile kaplanmıştır. Elde edilen verimlilik değerleri sırasıyla yüzde 5,06 (R_{ct}, 0,89 $ohmcm^2$) ve yüzde 4,31 (R_{ct}, 1,44 $ohmcm^2$) şeklindedir. Aradaki fark, platin filmlerinin artan katalitik aktivitesi ile ilişkilendirilmektedir. Daha sonra hibrit fotoanot hidrotermal ve spin kaplama yöntemleri ile hazırlanmıştır. Bu aşamada, DSSC'lerin verimliliğini artırmak için nanopartiküller ve hidrotermal olarak büyütülen metal oksit nanorod dizileri birleştirilmiş ve hibrit cihaz olarak adlandırılmıştır. Deneysel sonuçlar, nanopartiküller ve nanorodlardan oluşan bir hibrit cihazın (yüzde 5.58) verimliliğinin, yalnızca nanopartiküllerlerden (yüzde 4.95) ve nanorodlardan (yüzde 1.04) daha yüksek olduğunu göstermektedir. Güneş pillerinin verimliliği, ışık absorpsiyon miktarını en üst düzeye çıkarmak ve ayrıca hücreye ışık geldiğinde rekombinasyonu azaltmak için hidrotermal teknikler kullanılarak geliştirilmiştir.

Sonuç olarak, boya duyarlı güneş pilleri, üretim maliyetini azaltmak ve güneş pillerinin verimliliğini artırmak için umut verici bir yenilenebilir enerji teknolojisidir. Devam eden araştırma ve geliştirme ile, boya duyarlı güneş pilleri sonunda piyasada mevcut olan en uygun maliyetli güneş pillerinin adayı haline gelebilir.

Anahtar kelimeler: Boya duyarlı güneş hücresi, titanyum dioksit, platin, çekirdek katman, hidrotermal, hibrit güneş hücresi.

CONTENTS

NOMENCLATURE

Roman Letter Symbols

E_c	Energy of conduction band
E_v	Energy of valence band
E_{pa}	Anodic peak potential
E_{pc}	Cathodic peak potential
eV	Electron volt
I_{pa}	Anodic current
I_{pc}	Cathodic current
I_{sc}	Short circuit current
J_{sc}	Short circuit current density
nm	Nanometer
P_{in}	Incident light power
R_s	Series resistance
R_{ce}	Charge transfer resistance at the counter electrode
R_{rec}	Electron recombination resistance at the photoanode
R_{sh}	Shunt resistance
V_{oc}	Open circuit voltage

Greek Letter Symbols

η	Power conversion efficiency
λ	Wavelength
μ	Micrometer
τ_e	Electron lifetime

Acronyms

ACN	Acetonitrile
AFM	Atomic force microscopy
*AM*1.5	Incident air mass 1.5 global spectrum
CB	Conduction band
CE	Counter electrode
CIGS	Copper-indium-gallium selenid

CV	Cyclic voltammetry
DSSC	Dye-sensitized solar cell
EIS	Electrochemical impedance spectroscopy
FF	Fill Factor
FTO	Fluorine-doped tin oxide
HOMO	Highest occupied molecular orbital
LUMO	Lowest unoccupied molecular orbital
M	Molarity
*N*719	$Ru_3(NCS)_2$ dye
NREL	National Renewable Energy Laboratory
PA	Photoanode
Pt	Platinum
PV	Photovoltaic
SEM	Scanning electron microscopy
TiO_2	Titanium dioxide
UV	Ultraviolet
XRD	X-ray diffractometry

LIST OF TABLES

LIST OF FIGURES

CHAPTER 1

INTRODUCTION

Energy is a need for every living being. Not only do we need to consume energy for basic survival needs, but also we have an immense demand for it. The energy demand is constantly increasing around the globe, with non-renewable sources running out rapidly and renewable energy sources becoming more and more popular. The burning of fossil resources causes an increase in global temperature with the effect of greenhouse gases. This increase in temperature in the oceans and terrestrial regions threatens the balance of the world. The problem continues to get worse as the use of fossil fuel energy resources continues to grow. Because of this, there has been a sharp increase in the demand for clean energy. One of the most popular forms of clean energy is solar power. Intergovernmental Panel on Climate publishes a report in each 6-7 years an up-to-date assessment on climate change and the last one was published in February 2022 [1]. According to the report, global warming is more serious implications than ever before. A comment from one expert about the report is that there should be no excuses for a full switch to renewable energy, including costs [2].

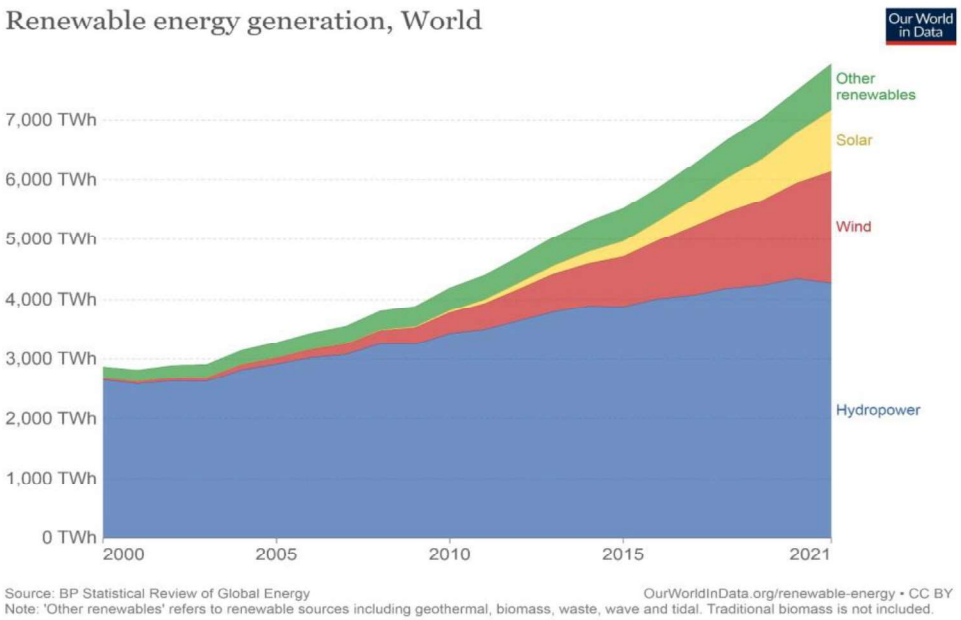

Figure 1.1 Global renewable energy generation chart [3].

Non-renewable resources are limited besides the damage given to nature, and even we are faced with the fact that fossil resources will soon run out completely. If an alternative solution to replace fossil resources is not found urgently, there will be major energy crises. Currently, developed and developing countries are making large investments in various renewable energy technologies.

Renewable energy is a broad term that refers to technologies that use natural resources to generate electricity. The most common renewable energy technologies are solar, wind, and hydropower. Figure 1.1 shows the distribution of energy generation in terms of renewable energy resources. Hydropower has the highest share, followed by wind and solar. The highest portion of hydropower should not mean that it is the most efficient way of producing energy. "Rome wasn't built in a day" and neither is the renewable energy infrastructure. Science needs time to progress. Technological development and scientific studies in recent years have allowed us to utilize solar and wind energy more efficiently. The portions in the figure will likely change as the researchers find more feasible solutions.

There is no such rule that one type of renewable energy is more effective than another. Each has its strengths and weaknesses. The conditions that need to be met for any given renewable energy technology to work are different. Below the three paragraphs explain briefly hydropower, wind and solar energy types, respectively. A summary of the advantages and disadvantages of renewable energy sources are presented briefly in the Table 1.1.

Table 1.1 Comparison of the renewable energy sources

Advantages		**Disadvantages**
Hydropower	Free infinite resource Low maintenance cost Reliability	Dependent on the weather High installation cost Change the natural habitat
Wind	Free infinite resource Clean Low installation cost	High noise for habitats Poor reliability High maintenance cost
Photovoltaic	Free infinite resource Clean Low maintenance cost Simple installation Silent working	High upfront cost Not reliable on night time Weather dependent High space allocation High cost of storage

Hydropower is the way to generate electricity from water. It is the most common renewable energy technology in developing countries. This system must be located close to a water source and there must be enough water flowing downhill for the turbines to turn. There is need a huge capital to start up and maintain a hydroelectric plant.

Wind energy technology is the conversion of wind energy into a useful form of energy, such as electricity. It is environmentally friendly and also has minimal impact on the environment when compared with fossil fuel power plants, which release millions of tons of CO_2 into the atmosphere every year. However, the noise around wind turbines and the maintenance cost of mechanical parts are two major challenges of wind energy.

Solar energy is another renewable energy technology that has become increasingly popular in recent years. The energy of the sun is clean and considered infinite. It is capable of providing the current and future energy consumption of the world. It is even thought that one hour part of the Sun's enormous energy corresponds to the energy consumed by all humanity in one year [4]. As this study is related to a type of solar energy, specifically dye-sensitized solar cells (DSSCs), we focus on solar cells from now on.

A solar cell is the most fundamental unit for the photovoltaic (PV) industry. It captures the sun's energy and converts it into electricity. This technology is user-friendly, scalable and practical as compared to other renewable energy types mentioned earlier. Many PV technologies including inorganic, organic, and hybrid solar cells have been developed for various application reasons throughout the past several years. The high module cost and challenging manufacturing process of silicon-based solar cells limited their use, despite their high conversion rate. Therefore, scientists have focused on developing an alternative solar cell that is cost-effective and has relatively simple production procedures [5]. Among emerging cells, DSSCs are the most effective, low-cost and widely used type.

In this study, well-designed counter electrode (CE) and photoanode electrodes were developed to further boost the efficiency of DSSCs. Different methods including chemical bath deposition, spin coating and hydrothermal growing were used in the CE

and photoanode electrodes of DSSCs. Chemical bath and spin coating were used to obtain the CE, while hydrothermal growth was preferred for photoanode. The efficiency of the resulting solar cells was measured under standard test conditions and compared with available DSSCs performances presented in the literature. The experimental results are detailed in Chapter 5.

1.1 Photovoltaic Technology

Solar cell technology, photovoltaic, is an environmental friendly and cost-effective application area of the solar energy. Solar cells are devices that convert the energy from sunlight into electrical current. There are two main groups of solar cells: wafer-based and thin film-based. They are both good at converting light into electricity, but they have different costs and efficiencies. They are made of different materials. Figure 1.2 demonstrates a comparison in terms of the way they are formed [6].

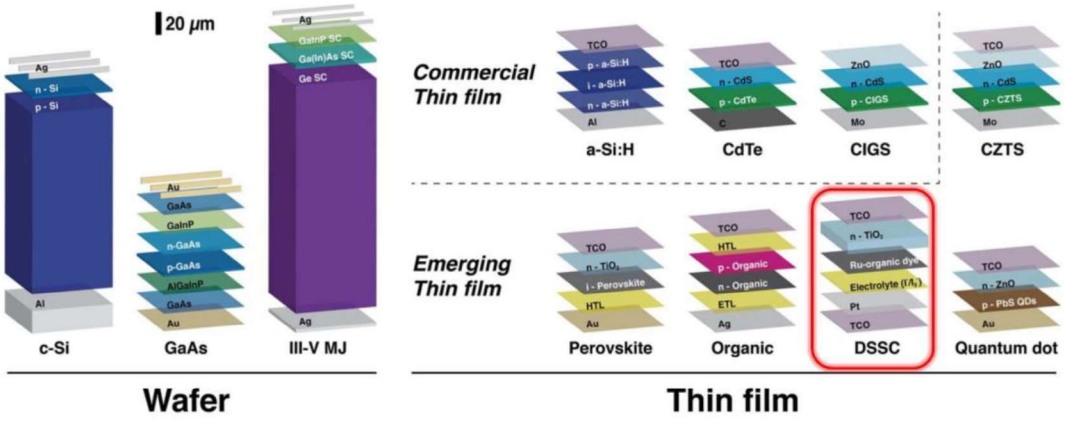

Figure 1.2 Solar cell technologies modified from [6].

Wafer-based solar cells are made of a thin wafer layer of silicon. Crystalline silicon (c-Si) and III-V multi-junctions are a sub-group of this group. Silicon solar cells are composed of wafers by nature and are the most common type in the commercial PV market. In 2020, global sales of silicon solar cells exceeded US$147 billion [7]. This technology has been expensive to manufacture due to the fact that its production requires high purifying costs during materials processing. The record efficiency obtained with

c-Si is 26.7%, which is so close to the theoretical limit of 29% [8, 9].

Gallium-arsenide solar cells is one of the leading III-V type solar cells. It has a small band gap (E_g) and good sensitivity to light. This technology is more efficient than c-Si technology with an efficiency of 27.6% [10]. However, its high price is the biggest obstacle to its spread. It is mainly used in space applications such as satellites [11].

To reduce the manufacturing cost of solar cells, research focus shifted to technologies that need fewer materials such as thin films. Thin film solar cells are made by depositing layers of photovoltaic material on a substrate. Thin film solar cells are cheaper and more flexible than wafer-based ones. This technology allows us to utilize the space on rooftops or solar farms more efficiently. Until now, the commercialized thin film solar cells are amorphous silicon (a-Si), cadmium telluride (CdTe) and copper indium gallium selenide (CIGS). a-Si solar cells have an efficiency of around 10% and they are currently used in small portable electronic devices [12]. CdTe cells have an efficiency of up to 22.1% at lab scale and 18% for commercialized module [13]. CIGS cells have 17.4% of efficiency as the highest efficiency in commercialized size [14].

The high absorption ability of the photo-active material of this sub-group makes the usage of thinner films possible. This enables the lowering of manufacturing costs. Moreover, it is possible to use flexible substrates. On the other hand, the dangerous elements in these technologies, such as cadmium and tellurium in CdTe solar cell or indium and selenium in CIGS solar cell make these technologies not environmentally friendly. The last group of thin films covers emerging technologies such as DSSCs, organic solar cells, perovskites, Copper zinc tin sulfide (CZTS) and quantum dots. They are currently in the research phase and have not yet been fully commercialized. However, it is believed that the remarkable efficiency results in this field will open the doors to mass production once some problems on stability, reliability and toxicity are overcome.

Among these emerging technologies, DSSCs are the most promising as they have low manufacturing costs and are relatively easy to fabricate. Organic solar cells are made from organic materials such as fullerenes and carbon nanotubes. This technology has the potential to be lightweight and flexible. Perovskite solar cells are a relatively new field that has attracted attention lately due to higher efficiencies of 25.7%, low costs

and the possibility of utilizing a wide range of materials [8]. However, the challenging fabrication procedures, vulnerability to heat and moisture limit their commercialization.

DSSCs are the most experienced, environmentally friendly and cost-effective option in this group since 1991 [15]. Considering NREL registrations, the record efficiency for DSSCs is around 13.0% [8]. In addition, unlike c-Si solar cells, DSSCs are also suitable for working under diffuse sunlight. This makes them superior and preferable in many respects for indoor applications and places where sunlight does not reach perpendicular to the surface. The main goal of this thesis is on this valuable solar cell type, DSSC, to increase efficiency of cells by using different techniques as in [16–22].

1.2 Milestones of Photovoltaics

The moment when 19-year-old French scientist Becquerel noticed the electric current under the light between the silver chloride and the platinum (Pt) electrode, was perhaps one of the most critical moments for the solution of the energy needs of the future humanity [23]. That fascinating event was the starting point of the PV journey with the invention of the photovoltaic effect for the first time.

Later, in 1904, Einstein tried to explain this effect theoretically and won the Nobel Prize in 1921 on this subject [24]. However, even before that award, the theory of the photovoltaic effect was proven by Milikan's experiments in 1916 and a method of silicon production developed by Czochralski in 1918 led to the avalanche development of the PV world [25].

In a short time, the PV devices became a hope for space applications and Bell laboratories fabricated solar devices for that in the 1950s [26]. The same laboratory reported that the first traditional silicon solar cell developed with an efficiency of 6% in 1955 [27]. In the 1970s, space applications were improved with the first GaAs heterostructure solar cells which have an efficiency of 20% [28]. However, these cells are expensive.

In 1991, another outshaking event occurred in the PV world with the announcement of O'Regan and Gratzel about a photoelectrochemical cell with a mesoporous structure. They achieved an efficiency of 7.1% [15]. Following the mononuclear dye usage, the

efficiency was improved up to 10% within 2 years [29]. This device type was completely different from the traditional silicon devices with its fundamental working principles which will be explained in the following chapter (Chapter 2). With the development of the dye as a 'donor-chromophore-acceptor', the efficiency reached 13% in a short time. From that day till today, DSSCs continue to develop without decreasing their speed.

1.3 Motivation and Goals of the Thesis

Efforts to improve the efficiency of DSSCs have been an intense focus along with their cheap and easy production costs. Numerous studies have been published on CEs and photoanodes development up to today. Pt and TiO_2 are the most widely used, almost indispensable chemicals for these two electrodes, respectively. This thesis is experimental and its main purpose is to improve the efficiency of device performance by developing variations of procedures while fabricating a DSSC device. There are mainly 3 contributions in this study. The first contribution is related to the CE and the rest of the contributions are on the photoanode.

It is widely known that high catalytic activity is essential for a successful CE. While searching for high catalytic activity, it is noticed that especially the opaque Pt films have often been overlooked. There is limited information in the literature about opaque Pt CE and its DSSC applications. This study presents a contribution to the literature with the optical, morphological, electrochemical and electrical analysis of opaque Pt CEs.

The next contributions are related to photoanode. The electrical properties are important parameters for a successful photoanode besides the high surface area and dye uptake ratio. Electrical properties change as the morphology changes. Therefore, it would be logical to take advantage of the superior aspects of two different morphologies. Although there are many studies on different morphologies obtained by different methods, connection problems still arise in hybrid layer design. Despite the numerous advantages provided by the hybrid photoanode design, this situation negatively affects the performance. One of the motivations of this study is to propose approaches to resolve this inconsistency. Another is to eliminate the analysis deficiencies in the case of combining nanoparticle and nanorod structures, as well as

to explain the situation in terms of optical, electrical, morphological, structural and electrochemical aspects. In addition, an optimization study is planned to be performed on the seed layer, which is a prerequisite for the hydrothermal method. It is predicted that the preparation conditions of this layer will be decisive in the properties of the nanorod layer to be grown on it.

In summary, the motivation of this thesis is to clarify the situation for the hybrid photoanode containing hydrothermal nanorod and very rare opaque Pt CE obtained by hydrothermal method and ultimately aims to increase efficiency with the control of experimental parameters.

The implementation plan for this study consists of the following tasks:

1. Experiment on two different deposition methods for Pt CE films: chemical bath and spin coating methods.
2. Experiment on the seed layer of four TiO_2 thin films used for the further hydrothermal process. (Aqueous $TiCl_4$ solution, chemical bath method, 0.10, 0.15 M)
3. Experiment on the hydrothermal growing of TiO_2 NR films.
4. Fabrication of hybrid photoanode design with nanorod and nanoparticles.
5. Characterizations of the films and analysis of the fabricated devices using X-ray diffractometry (XRD), Atomic force microscopy (AFM), Scanning electron microscopy (SEM), Cyclic voltammetry (CV), Four point probe measurement, Tafel measurement, Electrochemical impedance spectroscopy (EIS) and Current-voltage (I-V) measurement.

1.4 Thesis Outline

Chapter 1 presents an introduction to the thesis topic. It summarizes the classification of the PV technologies and their milestones. It also contains a motivation for this work and outlines the thesis structure. Chapter 2 provides information about DSSCs, their working principles and related literature. It covers the state-of-the-art studies in DSSC field and presents an overview of the requirements for a high-performance

device. Chapter 3 describes the utilized materials, the experimental procedures and characterization methods followed in this study. In this chapter, the reader will find the information on analysis tips of the characterizations. Chapter 4 addresses the theoretical calculations of the performance of a DSSC device. It also mentions the correlation between theory and experiment. Chapter 5 presents the experimental results and provides a discussion of the data obtained from the experiments. Finally, Chapter 6 draws a conclusion and provides possible future directions in DSSCs developments.

CHAPTER 2

BACKGROUND

This section presents fundamental information about the dye-sensitized solar cells and mentions the working principle of DSSCs for readers to have a background. Following that, current literature is summarized in order to provide readers with an updated understanding of the technology and show the position of the work presented in this study.

2.1 Dye-Sensitized Solar Cells

Dye-sensitized solar cells are devices that generate electricity with the light incoming to them. They can work under direct and diffuse light conditions and that property enhances their compatibility with indoor applications. DSSCs have four main components: (1) photoanode, (2) dye, (3) counter electrode (CE), and (4) electrolyte as shown in Figure 2.1.

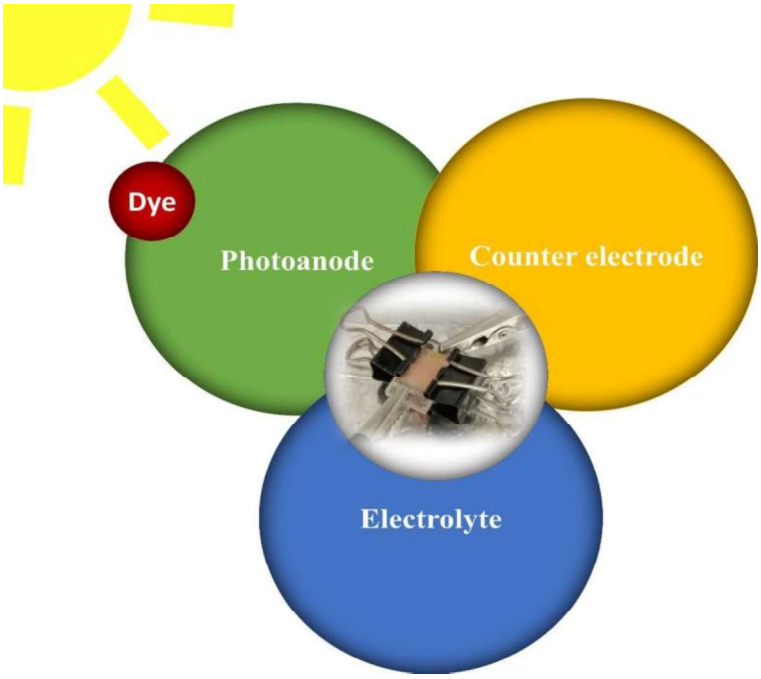

Figure 2.1 Components of a typical DSSC.

A photoanode is the first part of the device that interacts with the incoming light. It consists of a transparent conductive oxide substrate and a metal oxide layer on it. The generally utilized transparent conducting oxides are fluorine-doped tin oxide (FTO) or indium tin oxide (ITO) substrates [30]. A large portion of the incident light should pass through the photoanode and reach the attached dye molecules. The photoanode, in other words, the working electrode, includes mostly wide-band gap metal oxides (MOs) such as TiO_2 , ZnO or SnO_2 [31]. The MO layer in a photoanode is not in a bulky form, it is mostly in a mesoporous form to improve the specific surface area (sSA). The number of dye molecules attached to the layer is directly proportional to sSA. Namely, the number of attached dye molecules increases as the sSA increases. The photoanode can be composed of various dimensional nanostructures. The variations may appear in the following forms [32]:

a. zero-dimensional nanostructures (nanoparticles, nanospheres, and nanocubes),
b. one-dimensional nanostructures (nanorods, nanotubes, nanowires, and nanofibers),
c. two-dimensional nanostructures (nanoflakes, nanosheets, and nanoplates)
d. three-dimensional nanostructures (nanoflowers, pillar structures)

The different morphologies of the nanostructures can be determined according to the experimental conditions such as applied heat, time duration, utilized chemicals, acidity, etc. TiO_2, ZnO, or SnO_2 can be used in the photoanode. Among them, TiO_2 is the most commonly preffered material in DSSC fabrication due to its optical and electrical properties [33]. TiO_2 can be found in one of three different allotrope phases in nature and under synthetic conditions. These are anatase, rutile and brookite. They are a combination of TiO_6 octahedra units [34] and there are both edge and corner sharing for rutile and brookite structures while there is only edge sharing for the anatase structure as demonstrated in Fig.2.2 [35]. The optical band gaps (E_g) of TiO_2 are reported 3.2, 3 and 3-3.45 eV for the anatase, rutile and brookite phases, respectively. It means that the rutile TiO_2 with having a E_g around 3 eV can capture the light up to a wavelength of 413 nm and behave optically transparent above that region [36].

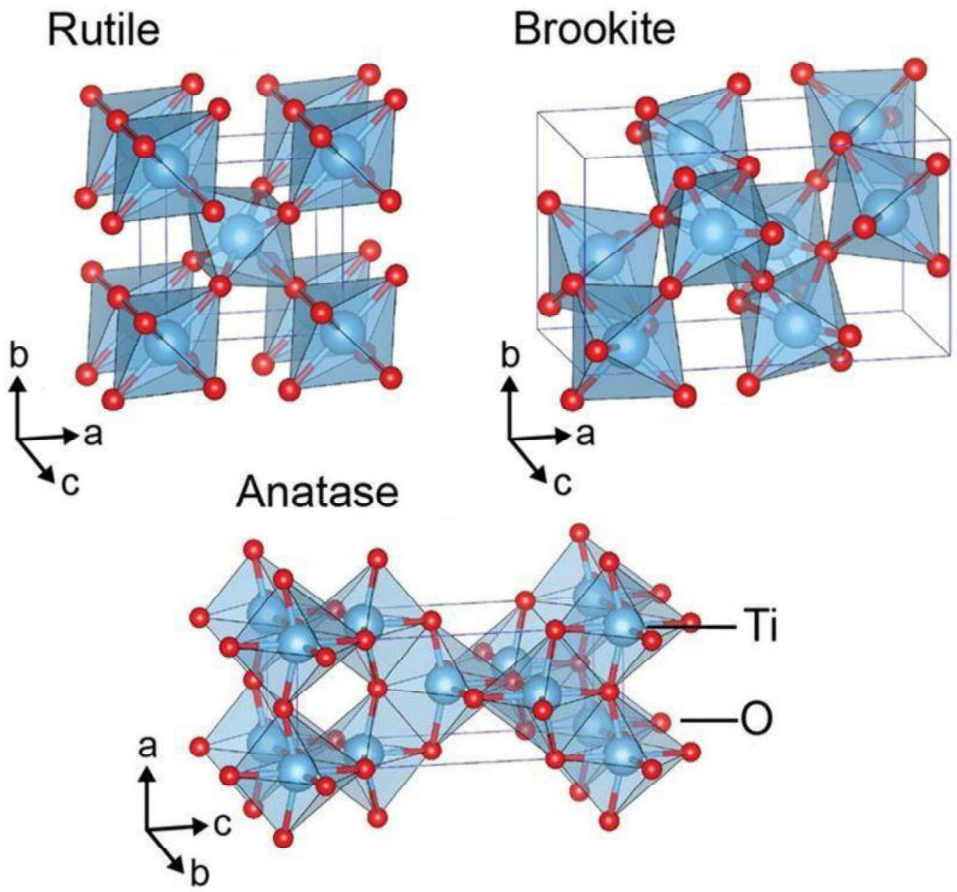

Figure 2.2 Representation of TiO_2 allotropes [37].

The second component of photoanode is the dye. It is a special molecule attached to the MO layer and is responsible for capturing the incident light. It can be classified as an organic and inorganic dye in terms of containing. The differences between these two groups are metals or metal complexes. There is one of the polypyridyl metal complexes of ruthenium, osmium or porphyrin in an inorganic dye. In the literature, the most commonly used reference dye for DSSCs is a brownish-red crystalline dye. The full name of it is di-tetrabutylammoniumcis-bis(isothiocyanato)bis(2,2′-bipyridyl-4,4′-dic arboxylato)ruthenium(II). The abbreviation of it is N719. The dyes are compared with respect to their light absorption coefficients. The dye of N719 has a specific metal to ligand charge transfer peaks at 390 and 531 nm in ethanol solution and the absorption coefficient of N719 is ϱ = 13,312 L mol^{-1} cm^{-1} at 520 nm [38, 39]. Dye molecules has some molecular levels such as lowest unoccupied molecular orbital (LUMO) level

and highest occupied molecular orbital (HOMO) level. These molecular levels are separated by an energy gap. For a proper energy level sequence in a device, the HOMO level of the dye should be greater than the redox potential of the electrolyte and the LUMO level of dye should be greater than the conduction band of photoanode MO. In this way, a sensitized electron can flow from the dye molecule to the metal oxide, TiO_2.

The third component of photoanode is CE, which holds the continuity of the cell with its catalyst layer. The needed energy level asymmetry in the kinetics is provided by the catalyst which makes the electron transfer faster and easier. Metals such as Pt and silver (Ag) or carbon-based materials such as CNTs or graphite combinations, organic conductive polymers can be utilized as a CE in a device. However, many are still competing with Pt and trying to keep up with its performance. With its unique properties, Pt is the most commonly preferred catalyst.

The last component of photoanode is the electrolyte. It is the medium that conducts electricity between dye and CE. It contains a redox couple for the continuity of the dye regeneration. The most common electrolytes used in DSSCs are iodide/triiodide redox couple in a solvent with an additive of ionic liquids. Ionic liquids increase the viscosity of the electrolyte and make ionic transmission harder. At the same time, it improves open circuit voltage (V_{oc}).

A typical device illustration is given in Figure 2.3. Each part has a unique importance in the device, but the main trick is to get a balance and compatibility among the four components. For example, there must be a proper positioning between the metal oxide conduction band in the photoanode and the LUMO level of the dye, otherwise electrons recombined and lost, the performance will drop inevitably.

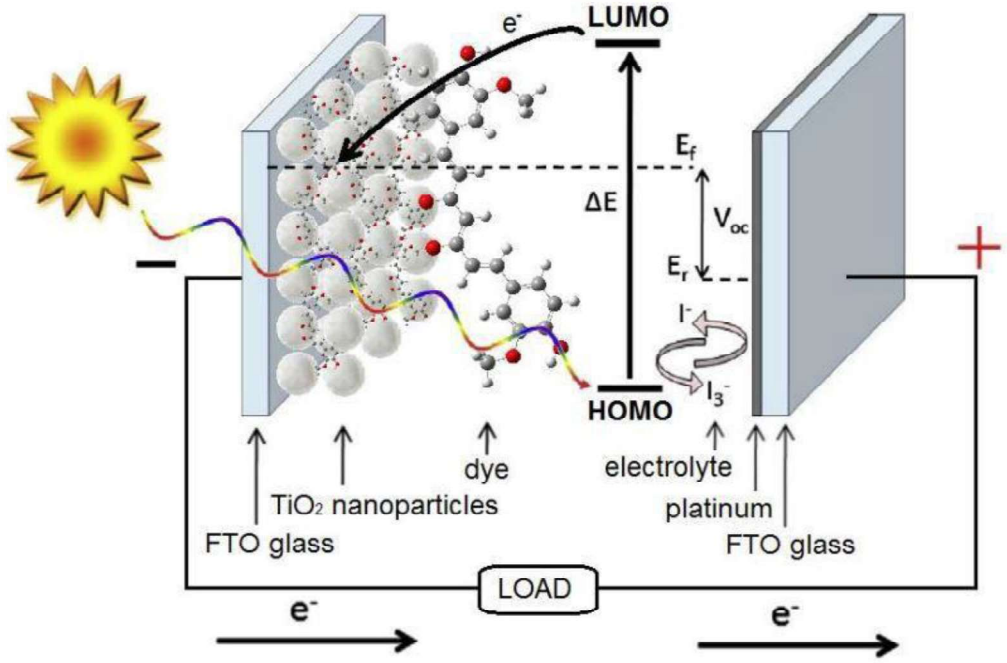

Figure 2.3 Representation of a fundamental DSSC device [40]

2.2 Working Principle of DSSCs

The basic principle behind DSSC is the photovoltaic effect in which the solar energy is converted into electrical energy. In nature, plants, and green living organisms make photosynthesis for energy generation using the sunlight. Inspiring by them, the DSSCs make an imitation of this natural process by using light as an energy source to generate electricity from dye molecules. The light excites the dye molecules which then transfer electrons to the electrode to produce electric current. This subsection will describe the working principle of DSSCs in detail and explain the important parameters that affect the performance of the cells.

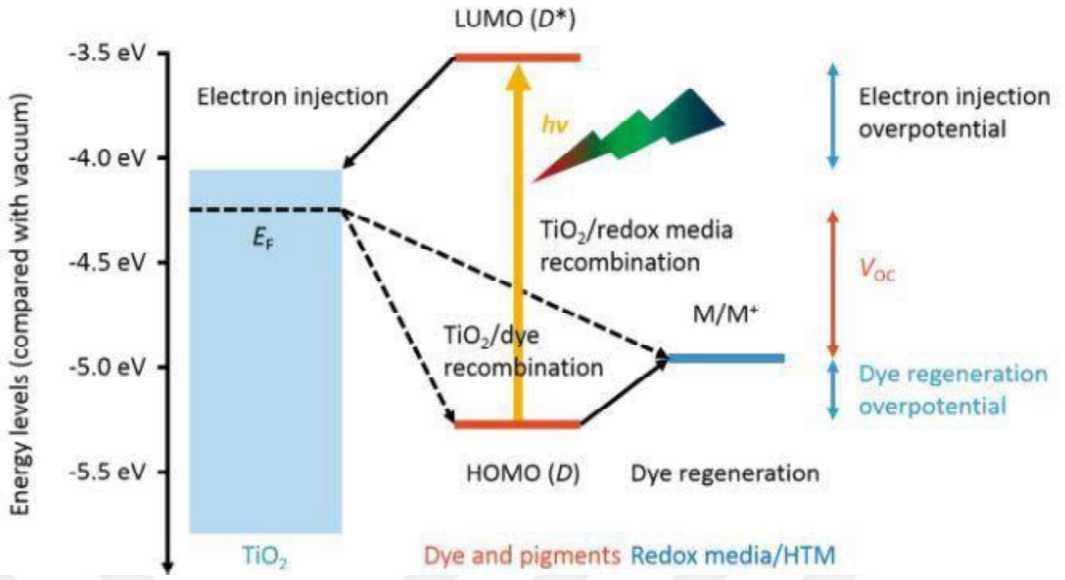

Figure 2.4 Representation of energy levels of a DSSC device [41].

The components of the DSSCs, mentioned in the previous section, have different energy levels compared to vacuum. Figure 2.4 shows these energy levels of the components in a DSSC device. In the first step of the electricity generation cycle, the incident light passes through the photoanode and reaches the dye molecules. Following, the light energy stimulates that dye molecule and excited an electron to a higher energy level as illustrated in Figure 2.4 with the yellow color sign. In other words, an electron jumps from the HOMO level to the LUMO level. This is called as "excited state". The energetic electrons start a journey via electron diffusion protocol. In the contact case, with the equalized fermi energy levels, the electrons pass through to the conduction band of MO. In the next stage, they continue their journey over a load, passing from MO to contact points. When the electrons reach the CE, they are taken back into the device by the catalyst of the device. They then pass from the CE to the electrolyte. The electrolyte completes the cycle with dye regeneration. The oxidized dye descends to the first ground level and is prepared for the next continuity cycle of electron generation with a light pulse on it.

The charge generation mechanism should basically provide 3 events: generation, separation, and collection of the charges. This mechanism differs sharply from conventional p-n solar cells for DSSCs [42, 43]. The charge generation mechanism of this group also differs from the p-n junctions. Therefore, this group is more successful

in compensating for crystal defects and even turning them into advantages in some circumstances. Charge separation, which occurs in a depletion region in the classical structure, takes place in the case of electron excess, where dye excitation occurs for DSSCs. It should also be noted that while the movement of electrons and holes is concerned in the classical p-n structure, only the movement of the electron is followed for DSSCs. The path taken by the electron between the dominant diffusion motion and the energy levels can be counted as a charge separation step. Afterwards, the collection of electrons at the counter electrode point eventually completes the charge generation mechanism. Thus, an electric current is created.

The electron follows a path by diffusion movement from a higher energy level to a lower energy level. This path is just like a ladder, the electron encountering a high step has barrier energy to overcome. It should also be kept in mind that this barrier is an undesirable barrier for the conduction of current because they cause the movement of electrons in the opposite direction and increase the leakage current. This is an undesired recombination event that deteriorates the device's performance.

2.3 Essential Properties for the DSSC Components

In order to achieve the desired performance, the counter electrode (Figure 2.5), the photoanode (Figure 2.6), dye and electrolyte components are expected to provide some specific properties. It is possible to apply various characterization methods and evaluate the results on both the coated films and the whole device. However, the components must have the following characteristics to have a high device performance in general: for counter electrode [44]:

* It should possess a high catalytic activity towards ionic electrolyte to achieve a faster regeneration of the cell.

* Electrical conductivity of a CE is also critical. Lower charge transfer resistance addresses the expectations with high catalytic activity.

* High optical reflectivity is desired to benefit more from light. Before the light leaving the cell, the back reflection towards dye molecules enhances the J_{sc}.

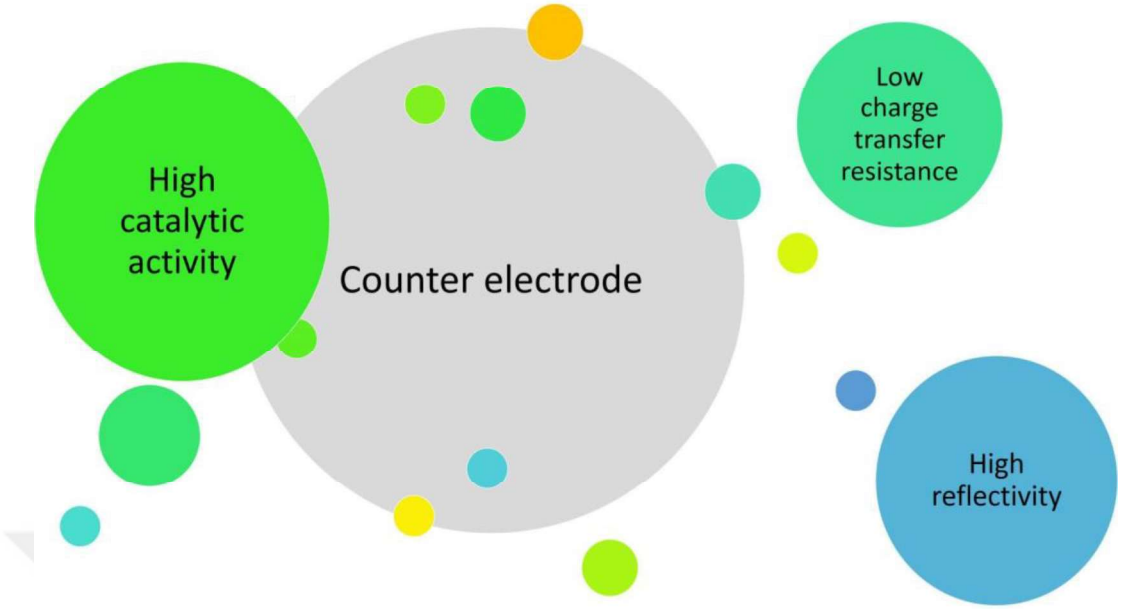

Figure 2.5 High quality CE properties.

* CE should have a chemical stability to stand with especially the chemicals inside of the electrolyte

* Similar to photoanode component, having a high surface area of the CE is expected, and it means for having a higher catalytic activity. The chance of an electron regeneration is increased with high number of the active sites.

* Adhesion properties of the film on the substrate is vital. Otherwise, it can start peeling off or dissolving in electrolyte would be detrimental for the device.

for photoanode [45]:

* Optical transmittance in the conductive layer should be as high as possible, thus the incident light can reach the dye molecules.

* It should have a large inner surface area to ensuring sufficient dye adhesion on it. A large number of dye molecules provide a high J_{sc}.

* It should have a good electrical conduction property to allow the photo-

generated current to pass over it,

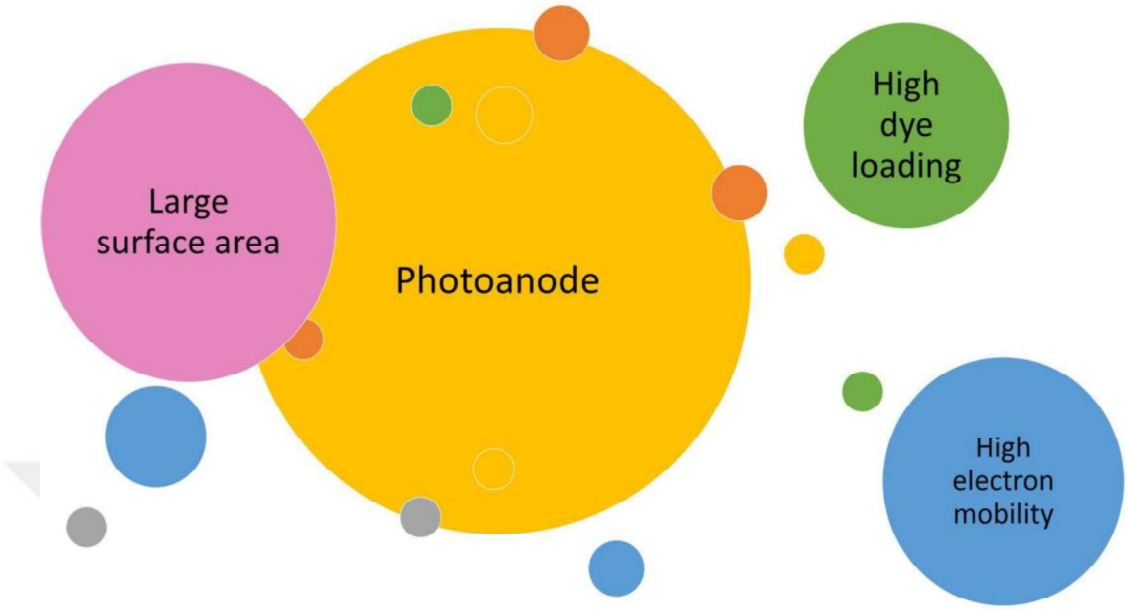

Figure 2.6 High quality photoanode properties.

* The photoanode should have a lower conduction band (CB) level compared to the LUMO level of the dye molecules to allow easy electron transport. A higher energy level than CB of photoanode behaves as a barrier for transport and decreases the current density.

* Keeping in mind the driving force caused by diffusion with hopping mechanism in that kind of device, the thickness should not be over the electron diffusion path length. At the same time, it should have high electron mobility. Otherwise, electrons will be recombined before reaching the contact points.

for electrolyte [46]:

* Lower conflict in the absorption region of the selected dye, especially in the visible region is important. Because it may reduce the capability of dye-sensitized photo-generation.

* Corrosion is not the desired case. If the electrolyte contains corrosive ingredients, then it may harm the electrodes and destroy the working device conditions. It should be chemically inert.

* Having a fast diffusion of charge carriers, and high ionic conductivity are required to provide the high dye-regeneration process. The low viscosity of the electrolyte favors that.

for dye [46]:

* High extinction coefficient is an important criterion for dye selection.

* As possible as high and narrow light absorption in the visible spectrum is expected to have a high photo-current.

* The selected dye should possess a higher level of lowest unoccupied molecular orbital (LUMO) compared to TiO_2 CB, the difference corresponds to a driving force for electron injection. A lower highest occupied molecular orbital (HOMO) level compared to redox electrolyte is also required to lead a driving force for dye regeneration [47].

* A lower tendency to agglomerate on the TiO_2 surface is needed. Binding selections of the dye affect the device performances, monolayer connection of dye is preferred among others.

* The small molecular size of the dye is favorable so that more molecules can be attached to the surface of the photoanode.

2.4 The State-of-the-art in DSSCs

This study covers three different experimental stage basically. Therefore, the literature is divided into 3 subsections. The first subsection focuses on the literature about Pt counter electrode deposition methods while the second and the third subsections present literature about seed layer and hydrotermally grown photoanode for DSSCs, respectively.

2.4.1 Literature on Pt CEs for DSSCs

There are two main dominant methods of obtaining Pt NP in the literature: solution-based methods such as thermal or chemical reduction, and physical methods such as sputtering. Below some relevant studies from each method is highlighted.

The solution-based approaches are the most preferred method in the literature. In solution-based approaches, the solution can be applied to the film surface using one of the following deposition processes: spin coating, chemical bath deposition, or spray coating.

Hashmi et *al*. compared two different solutions-based approaches: thermal and chemical reduction. The solution they used is 40 mM of H_2PtCl_6 in isopropanol. They chose the sodium borohydride ($NaBH_4$) aqueous solution as a chemical reducing agent. During the coating process, they encountered with the in-homogeneity case of the coating and as a solution to this, they proposed to keep the substrate under UV-ozone light just before coating. In their study, they reported that thermal platinization tends to form small Pt nanoparticles compared to the chemical reduction method. Indeed, the SEM image of it looks almost identical to the bare FTO. It is hard to recognize Pt nanoparticles. Another point in their results is that bigger Pt particles in the range of 20-40 nm can be formed by the chemical method.

Calogero et *al*. compared 3 different methods on Pt CE: thermal decomposition, sputtering and coating of the synthesized NPs [48]. Among these methods, sputtering with the efficiency of 3.90% and NP coating with the efficiency of 3.77% yielded promising results. For the solution part, they utilized tetraoctylammonium bromide (TOAB), and $NaBH_4$ chemicals. The high reflectivity of the film was highlighted only for the case of sputtered Pt film having a lower transmittance.

Similarly, Wang et *al*. applied chemical reduction method using $NaBH_4$ agent and added Triton X-100, a kind of conditioner, to the solution [49]. They stated that the color of this mixture changing from yellow to black is an important indicator of Pt NP formation. Then, they obtained a Pt NP coated film by using the dipping method. They obtained a higher catalytic activity of CE and higher efficiency of DSSC (6.95%) compared to the one with a CE of chemical reduction method (6.64%). The EIS results with a lower value of R_{ct} were also consistent with the performance. The transparency of the films for both of the methods is around 60%, but there is no remark on the reflectivity of the films.

Tsai et *al*. also worked on chemically and thermally reduced Pt films [50]. They utilized $NaBH_4$ agent for chemical reduction of a Pt film and applied a paste with doctor blade for the thermal reduction of an other Pt film. They obtained better catalytic activity for the thermally reduced Pt film with 7.66 of efficiency.

Iefonova et *al*. utilized the sputtering and spray deposition methods in their study. For the spray deposition, they utilized a solution of Pt NPs in acetone. They made a comparison between the sputtered Pt film (6.46%) and the spray-deposited Pt film (6.17%) in terms of device performance and CE catalytic activity [51]. Additionally, the optical properties were different for the films, the sputtered film was opaque and the spray-deposited one was transparent. The sputtered Pt film had a higher catalytic activity. This situation was also in consistent with the J_{sc} and η values. However, the sputtering method is quite expensive, the spray deposition method has been proposed considering the large-scale coating possibilities and costs.

Wang et *al*. evaluated a Pt electrode coated with the sputter method as a reference and they reported that it had approximately 15% transparency in the wavelength range of 300-800 nm [52]. They also emphasized that that Pt film has high reflectivity. This is a preferable advantage for a counter electrode. However, they commented that the opacity of the Pt film would not be suitable for bi-facial applications and reported that its measured efficiency when light coming from the back was 1.6%.

According to the studies listed in Table 2.1, sputtering has a high cost and the chemical reduction method frequently needs a reducing agent, which means an extra step to remove it after the reaction occurs. Moreover, the coating methodology and detailed analysis of the optical, electrical and catalytic properties of opaque Pt films obtained by chemical bath deposition in the role of a DSSC CE have not been addressed sufficiently in the literature. This thesis study contributes to the literature in this respect.

Table 2.1 Literature on deposition methods of Pt CEs

Author	Method	J_{sc} (mA/cm^2)	V_{oc} (V)	FF	η (%)
Calogero et *al*. [48]	Drop casting of NPs	10.14	0.66	0.56	3.77
	Sputtering	11.28	0.64	0.54	3.90
Wang et *al*. [49]	Dip coating	14.23	0.76	0.64	6.95
Tsai et *al*. [50]	Thermal reduction	16.01	0.76	0.63	7.66
	Chemical reduction	16.34	0.70	0.65	7.43
Iefanova et *al*. [51]	Spray deposition	11.24	0.820	0.67	6.17
	Sputtering	10.85	0.825	0.72	6.46
Wang et *al*. [52]	Sputtering	15.37	0.71	0.69	7.52
Hashmi et *al*. [53]	Chemical Reduction	11.70	0.67	0.54	4.30
	Thermal Reduction	11.17	0.67	0.65	5.10

2.4.2 Literature on Seed Layers for DSSCs

A seed layer is frequently a prerequisite to form a well-organized nanorod growth on the surface. The homogeneity of the seed layer makes a significant difference in the growth and related device performance. When the literature is examined, it was observed that different thin seed layers can be obtained by using different substrates, coating methods, precursors and recipes as in [54–61].

In some studies, nanorods were grown by hydrothermal method without a seed layer. For the TiO_2 NR which was tried to be grown directly on FTO substrate without a seed layer, the preferred phase is still rutile as compared to anatase. The reason of that magic is the lower lattice mismatch (2%) between the FTO and rutile TiO_2 [54]. However, in this case the direction of the rods will be disordered and will not be perpendicular to the substrate surface [54]. A proposed seed layer is that motivate an oriented growth for FTO substrate. Even for the other substrates, it is strictly mandatory to be able to grow a nanorod layer.

For example Wang et *al*. tried to obtain a nanorod array by hydrothermal method on different substrates such as silicon, sapphire and FTO [55]. They found that TiO_2 NR array can be grown even on sapphire if the seed layer step is not skipped. For the seed layer, 0.075 M of titanium tetraisopropoxide (TTIP) dissolved in isopropanol and applied by drop casting method. The DSSC device obtained with FTO substrate

achieved 1.10% of efficiency.

Considering the precursor choice for the seed layer, $TiCl_4$ is a suitable candidate for the forming of a rutile film with a slow and controlled rate of hydrolysis among other candidates such as $TiCl_3$, TTIP, titanium ethoxide [56].

Kalb et *al*. investigated the effects of three different methods of sputtering, evaporation, and spin-coating on seed layer properties [57]. When these methods are taken into account, the first noticeable details are the pinholes in the layer obtained by the sputtering method, the necessity of lithography masks for e-beam application and the application complexity. They reported an opinion over the solution-based coating of the seed layer was more practical, cheaper and more prevalent way.

As Liao et *al*. discussed in their work, the presence of the seed layer is critical to the morphology and orientation of the film that will subsequently grow and affect the performance of the device. They utilized a spin coated seed layer as a base for the TiO_2 NR array. The optimum TTIP solution molarity was found in the range of 0-0.075 M and 0.025 M with 1.48% of efficiency [58]. They recognized that 0.05 M is not enough to undertake the role of the seed layer so the performance is close to the bare one. The highest molarity (0.075) is overrated and the moderate ones have challenges to each other. Their explanation for enhanced performance with an optimized seed layer is that the increase in dye absorption reduced charge recombination value and controlled the device performance.

Jin et *al*. mentioned that the presence of a rutile seed layer increases the nucleation surface [59]. It is a guide for the TiO_2 NRs that will grow on these signed areas during the hydrothermal process. The solution molarity utilized for the seed layer formation determines the density of nucleation sites. Jin et *al*. studied different molarities of aqueous $TiCl_4$ solution and reported that 0.4M of solution coated seed layer is better than others with 2.91% of efficiency. They also stated that the existence of a seed layer reduces the recombination as behaving as a dense blocking layer.

Yuan et *al*. obtained a seed layer by chemical bath method with 0.15 M of aqueous

$TiCl_4$ at 70°C for 30 minutes and then they managed to grow quite long nanorods (13 μm) on it [60]. They anticipated that the existence of a seed layer helped to grow such long nanorods by improving the adhesion between NRs and FTO substrate. Otherwise, the peeling of such a long layer would be inevitable. The maximum device efficiency with a grown layer with a seed layer was reported 2.0% without any additional etching treatment.

Similar adhesion strengthens the effect of the seed layer was also reported in the study of Wan et *al*. [61]. They applied 0.3 M $TiCl_4$ aqueous solution at 70°C for 2h as a seed layer. Thanks to that seed layer, in hydrothermal stage, $TiCl_4$ in solution transformed into rutile TiO_2 nanorods by rapid hydrolysis. Moreover, even though they repeated the hydrothermal growth stage several times, the powerful adhesion of the seed layer has prevented the peeling of the quite long nanorods from the surface.

Table 2.2 Literature on deposition methods of TiO_2 seed layer

Author	Method	J_{sc} (mA/cm^2)	V_{oc} (V)	FF	η (%)
Wang et *al*. [55]	TTIP, Drop-wise	NA	NA	NA	1.10
Liao et *al*. [58]	TTIP, Spin coating	3.48	0.76	0.58	1.48
Jin et *al*. [59]	$TiCl_4$, Chemical bath	6.15	0.77	0.61	2.90
Yuan et *al*. [60]	$TiCl_4$, Chemical bath	3.91	0.69	0.74	2.00
Wan et *al*. [61]	$TiCl_4$, Chemical bath	3.65	0.76	0.48	1.34

According to the studies listed in Table 2.2, the wider range of molarity should be scanned, and the selection of the precursor and deposition method is also quite important for the quality of the seed layer. In this thesis, a quality mark, a figure of merit is proposed following optical, electrical and morphological analyzes for the planned seed layer. This thesis study contributes to the literature in this respect.

2.4.3 Literature on Hydrothermally Grown Photoanodes for DSSCs

The hydrothermal growing provides many advantages. It allows TiO_2 NR array formation easily and more cheaply. This enriches the design of the classical nanoparticle photoanode completely. The factors affecting the growth of the TiO_2 NR array are reviewed in the following paragraphs in detail. These can be itemized as temperature, time, acidity, and precursor selection etc. This literature summary also

covers hybrid photoanode design examples with different nanostructure combinations.

Iraj et *al*. grown TiO_2 nanorods and fabricated devices comparing the temperature, time, precursor concentration, and acidity [62]. It was reported that with increasing temperature, the reaction fastens and nanorods get larger. The increased gradient of time in that experiment provided the changing of mostly the length of the rods and the aspect ratio. After a long reaction time, the nanorods start to the peeling off. With increasing the $TiCl_4$ precursor concentration, it was concluded that the density of the grown layer and aspect ratio of the nanorods increased along with the morphological property changes. As a final observation regarding acidity, a high acidity of the solution mostly increases the aspect ratio of nanorods.

In another study, Ghoderao et *al*. investigated the growth of nanorod structures on FTO substrate at different temperatures (150-180 ˚C) [63]. Among these temperatures, the highest efficiency was recorded as 1.79% at 180 ˚C. The study concluded that the reaction temperature affects the growth rate.

Liang et *al*. used the hydrothermal method in two different steps in [64]. TiO_2 nanorod structure was obtained by the method they applied with titanium butoxide precursor at 150 ˚C for 12 hours. Afterward, they observed the formation of anatase branches on the nanorod structure with aqueous solutions of ammonium hexaflurotitanate. It was the second stage of the experiment about optimization of the surface area and the spacing between nanorods. It was noted that with the anatase branches added to the structure in the second stage, the surface area increased to a large extent and provided a connection between the rutile nanorods. The best result was obtained as 2.4% of efficiency of 2 hours. The performance was determined as 1.1% for nanorods only, without the second hydrothermal part.

Pawar et *al*. worked on a rutile TiO_2 nanostar over nanorods with different amounts of TTIP in the range of 0.1 mL to 0.5 mL [65]. This study was carried out at a higher temperature (180 ˚C) and in a 3 hours. The highest efficiency of 1.6% was achieved with 0.3 mL of TTIP. XRD results point out a polycrystalline TiO_2 structure containing a rutile phase. The crystallite size of rutile nanorods was reported that increased with boosting of the TTIP amount. The E_g of the films decreased from 3.11 eV to 3.05 eV

and get closer to bulk rutile E_g (3.02 eV).

Ahmad et *al*. studied on two different hydrothermally grown TiO_2 morphologies: nanorod and nanoflowers [66]. They coated microsize flowers on top of the nanorods and achieved a deteriorate hybrid structure. The study, drawing attention to the low FF value in the hybrid structure, argued that the low efficiency was due to the weak electrical connection between the layers.

Feng et *al*. worked on the combination of NR and NP in hierarchical structure [67]. With the hydrothermal method applied to the nanoparticle coated film, sprouting NR structures were obtained by leaking through the particles. In the smart hybrid structure series obtained by increasing the amount of precursor, and the highest efficiency was measured as 8.62% with the volume ratio of with moderate precursor concentration. Increment of roughly 30% of efficiency compared to the NP reference device was explained with superior light scattering. The faster electron transport and better dye absorption ability.

Yu et *al*. explored the duration of $TiCl_4$ treatment layer applied on hydrothermally grown TiO_2 NR layer applied by chemical bath method [68]. They reported that NP formation observed by the wet chemical method over a 24-hour period. They discovered that the surface area and surface roughness increased with these added NPs. The efficiency obtained for the film containing NR and NP was found as 3.47%.

Jiang et *al*. firstly grown a nanorod layer by hydrothermal and etch this by a laser pattern [69]. Afterwards, a hybrid structure was obtained by applying the TiO_2 NP layer with the doctor blade method. The efficiency values obtained for NP, NR and Hybrid structure were reported as 4.0%, 4.8%, and 5.1%, respectively.

In another hybrid work, Ahmed et *al*. applied an TiO_2 NP layer top of the hydrothermally grown TiO_2 NR layer [70]. The efficiency values obtained for NP, NR and Hybrid structure were reported as 1.37%, 4.76%, and 7.37%, respectively. The detail in this work is that binder free TiO_2 NP layer applied before the porous NP layer to increase the compatibility between the NR and NP layers. It was strengthened the connection and helped the hybrid structure to reveal its high dye absorption and electron transmission properties.

Shobana et al. obtained 0.30% of efficiency only for nanorod, and 4.23% of efficiency in nanoparticle and nanorod combined hybrid structure [71]. They did not mention any about treatment layers and highlighted the synergistic effect between nanorods and nanoparticles.

Table 2.3 presents a brief summary of hydrothermally grown hybrid structured photoanodes investigated by researchers.

Table 2.3 Literature on hydrothermally grown photoanodes for DSSCs

Author	Method	J_{sc} (mA/cm^2)	V_{oc} (V)	FF	η (%)
Iraj et *al*. [62]	$TiCl_4$, 170 C 4.5h	4.15	0.76	0.59	1.86
Ghoderao et *al*. [63]	TTIP, 180 C 5h	2.9	0.76	0.8	1.79
Liang et *al*. [64]	TBT, 150 C 12 h	2.57	0.76	0.54	1.10
Pawar et *al*. [65]	TBT, 180 C 3h	1.46	0.69	0.45	1.60
	TBT, 150 C, 5h	NR 2.98	0.74	0.68	1.52
Ahmad et *al*. [66]	Two step hydrothermal	NP 14.08	0.68	0.68	6.56
	Bottom layer: NRs	11.29⋆	0.77	0.49	4.27
Feng et *al*. [67]	TBT, 150 C 6h	NP:16.20	0.67	0.56	6.12
	Bottom layer: NPs	18.66⋆	0.69	0.67	8.62
	TBT, 160 C, 18h	NR:3.20	0.76	0.66	1.61
Yu et *al*. [68]	$TiCl_4$ treatment (CBD, 33 h)	NP:10.86	0.70	0.50	3.80
	Bottom layer: NPs	6.99⋆	0.81	0.61	3.47
Jiang et *al*. [69]	TBT, 175 C 14h	NA NA	NA	NA	NP:4
	Bottom layer: NRs		NA	NA	4.8⋆
	TTIP, 150 C, 4h	NR 2.86	0.74	0.70	1.37
Ahmed et *al*. [70]	Binder free paste	NP 11.42	0.72	0.64	5.01
	Bottom layer: NRs	17.10⋆	0.76	0.58	7.37

⋆shows the result for Hybrid device.

As shown in the studies in Table 2.3, there are many possibilities to make a hybrid photoanode design. However, investigating this design with hydrothermal methods brings with it some difficult compatibility problems. This case is overlooked and limited information on it in the literature and it deserves further investigation on it. This work has a problem-solving approach on that incompatibility issue between nanorods and nanoparticles.

CHAPTER 3

MATERIALS AND METHODS

This chapter presents the utilized chemicals and explains the specific experimental procedures for deposition of the films and fabrication stages of the devices in this work. In addition, the application stages of the experimental methods such as chemical bath deposition, hydrothermal growth, spin coating are described in this section.

3.1 Materials Utilized in the Experiments

Fluorine doped tin oxide coated glass substrates were employed as a substrate for all stages of the experiments. These substrates have a sheet resistance of 7Ω/sq and were obtained from Sigma Aldrich (735167). Acetone (Sigma Aldrich, 0.32201), de-ionized water, and ethanol (Merck, 100983) are used as cleaning chemicals. Chloroplatinic acid (H_2PtCl_6, Sigma Aldrich, 520896) and isopropyl alcohol (Sigma Aldrich, 278475) were utilized for the CE.

Experiments with photoanode electrodes include several steps. Therefore, we used Degussa P25 powder (Evonik, Rutile and Anatase mixture), titanium butoxide (TBT, Sigma Aldrich, 244112), titanium tetrachloride ($TiCl_4$, Sigma Aldrich, 280566), titanium tetraisopropoxide (TTIP, Sigma Aldrich, 205273) chemicals as TiO_2 source in photoanode deposition phase. The supplementary chemicals required are hydrochloric acid (HCl, Merck, 100317), nitric acid (HNO_3, Merck,30709), methanol (Merck,106009) ethyl cellulose (Sigma Aldrich, 46070 and 46080), and terpineol (Sigma Aldrich, 86480). N719 dye was purchased from Dyesol (MS003190). The liquid electrolyte compounds utilized were 4-tert-Butylpyridine (TBP, 142379), 1-Propyl-3-methylimidazolium iodide (BMIMI, 713066), iodine (I_2, 207772), guanidine thiocyanate (GTC, G6639), acetonitrile (ACN, 34851), and valeronitrile (155098). All of the purchased compounds were utilized as it is without being purified.

3.2 Experimental Process Details

This section covers the experimental details of the Pt CE, seed layer optimization and hydrothermal hybrid device fabrication. The experimental data were collected from at least three batches of cells for each type of film or device, and average values were used to define the performance characteristics.

3.2.1 Pt Film Deposition and Device Fabrication Process

FTO coated substrates were cleaned using ethanol, acetone and de-ionized water using an ultrasonic cleaner for 10 minutes before the coating process. This cleaning process was done for all the substrates (photoanode and CEs) before any deposition process.

10 mM of H_2PtCl_6 dissolved in isopropanol. It was mixed using a magnetic stirrer for 2 hours at room temperature. This solution was used for two different types of deposition: the spin coating and chemical bath deposition [72]. The process is summarized in Figure 3.1.

The utilized spin coating recipe for this work was 2000 rpm spinning speed for 20 seconds. This was repeated 20 times to obtain a reasonable coating. 25 μL of the solution was utilized per coating cycle. The spin coated Pt film was denoted for the rest of the work as a sample of S1.

The utilized chemical bath deposition recipe for this work was immersing the substrate inside the previously prepared chemical solution at 75˚C for 30 min. The coated Pt film was denoted for the rest of the work as a sample of S2. S1 and S2 films were heated at 450 ˚C for 30 min. This heating process is for the coated metallic Pt to be reduced to an active Pt particle containing film surface. As summary, these electrocatalytically active Pt films served as CEs for the DSSCs.

The photoanode of devices is composed of only TiO_2 nanoparticles. For compact layer formation, the cleaned films were immersed in the prepared solution chemical bath for 1 minute. Afterwards, P25 powder, ethyl cellulose and terpineol were mixed to have a paste. It was applied by a spin coating device at 2000 rpm and 3000 rpm for 30 seconds, respectively.

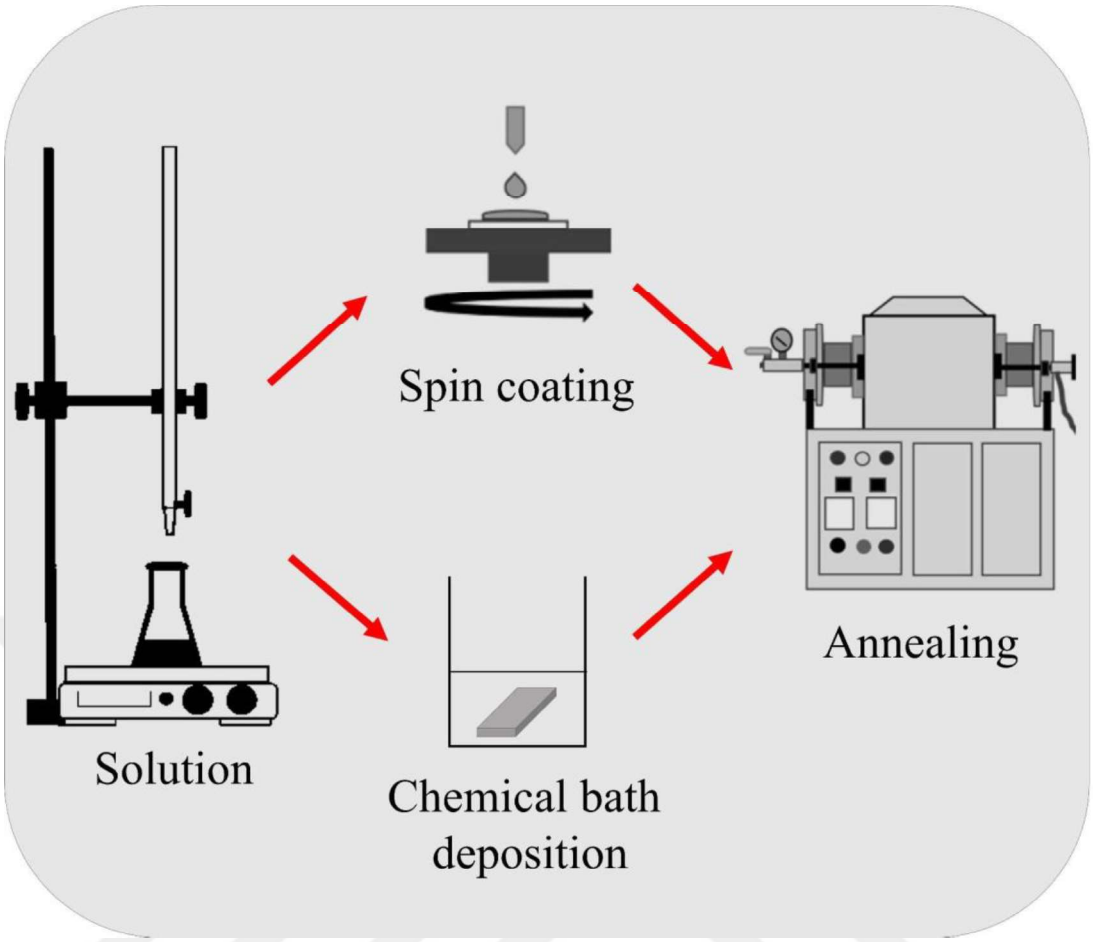

Figure 3.1 Representation of Pt CE process.

0.3 mM N719 dye dissolved in methanol. The photoanodes stayed in this dye solution overnight in dark for the loading. Following the taking out from the solution, the dye-loaded electrodes were rinsed with ethanol and dried in air.

A liquid electrolyte was prepared by stirring the 0.6 M BMIMI, 0.5 M TBP, 0.05 M I_2, 0.1 M GTC in 85:15 volumetric ratio of acetonitrile/valeronitrile solvent.

After preparing all components separately, to assemble a device TiO_2 and Pt films on FTO substrates got together in a sandwich form while the conductive sides are both insides. The prepared liquid electrolyte was injected between these two electrodes.

3.2.2 Seed Layer Deposition Process

The usage of $TiCl_4$ is a substantially dangerous and grueling process. A need for practical usage has occurred and a stock solution of it was prepared. 2M of aqueous $TiCl_4$ solution was prepared in an ice bath at about 0 ˚C. When a $TiCl_4$ solution isrequired for the following steps, the stock $TiCl_4$ solution will be used.

For the seed layer usage, the main stock solution was diluted to a lower molarity of 100 mM and 150 mM. Cleaned FTO glass substrates were immersed in this solution for different time intervals such as 40 min and 60.

The films are named s104, s154, s106, and s156 which the first two digits symbolized the molarity of the solution (100 mM, 150 mM) and the last third digit shows the duration of the bath process (40 min, 60 min) as listed in Table 3.1.

Table 3.1 Nomenclature for the seed layer optimization film samples.

Time/Molarity	0.10 M	0.15 M
40 min	s104	s154
60 min	s106	s156

3.2.3 Hybrid Device Fabrication Process with Hydrothermal Method

For this part of the experiments, s154 seed layer proposed in the previous part was selected and applied as a seed layer or blocking layer for the other coatings. An aqueous $TiCl_4$ solution was applied as a seed layer onto the cleaned FTO glass. Viscous paste prepared with the given recipe above applied by spin coated at 4000 rpm and coated as two layers and annealed at 450˚C for 1 h. The TiO_2 NPs coated photoanode called as S3 in this work.

For the hydrothermal growth process, a seed layered FTO was positioned with conducting side facing down at an angle into the Teflon autoclave box. HCl and de-ionized water were mixed in a volume ratio of 1:1 (30 ml total) to obtain a clear solution. Then, 0.5 ml of titanium butoxide was added to the solution. Growing of the films with hydrothermal process were realized at 150˚C for 4 h. After annealing process at 450˚C for 30 min, the films exposed to a rinsing with de-ionized water. The TiO_2 NRs coated photoanode will be called as S4 in this work.

Subsequently, a viscous NP paste was deposited onto another TiO_2 NR film by spin coating; this was denoted as Hybrid without buffer layer (Hybrid wo BL) for the film as S6 in this work.

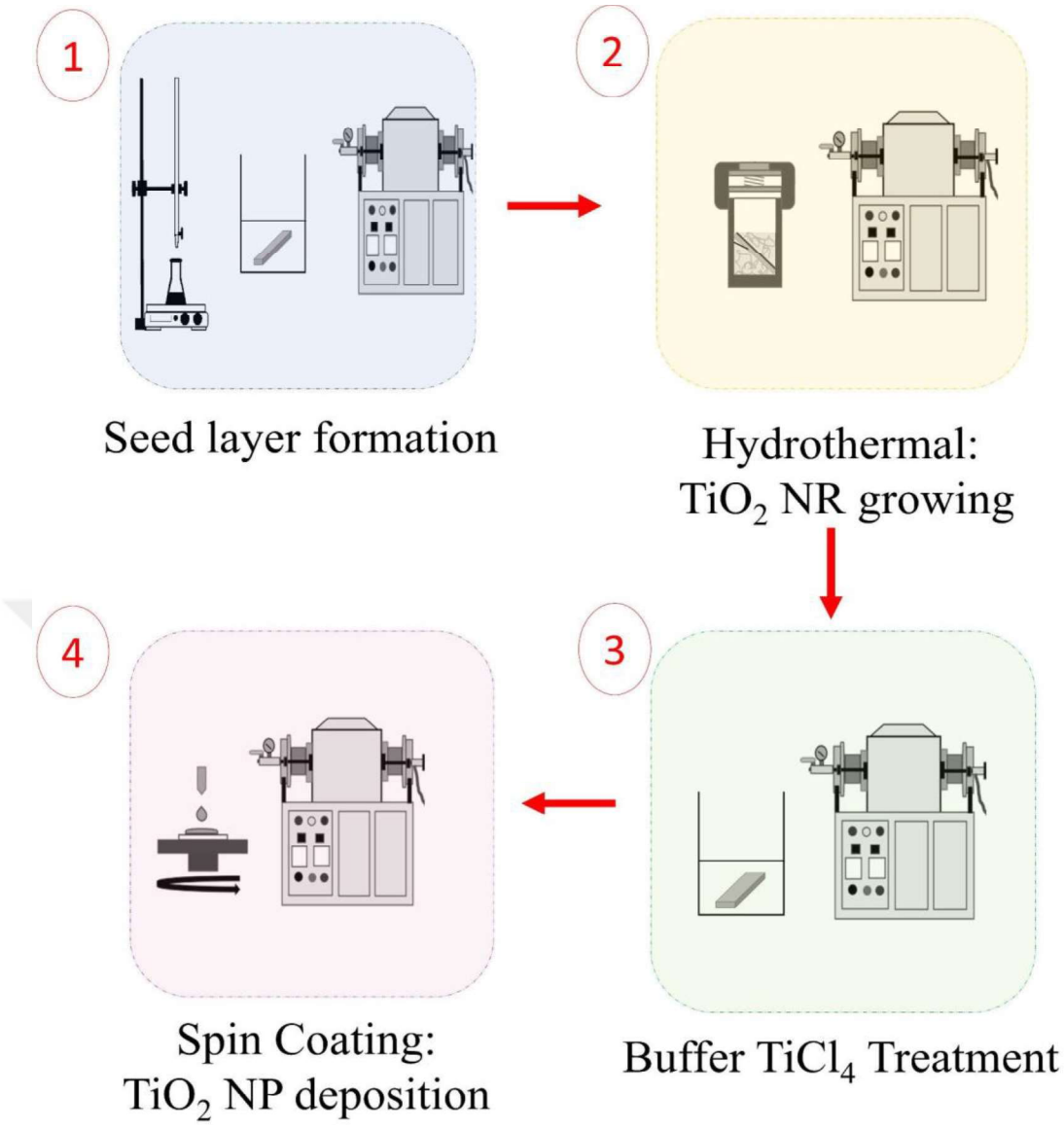

Figure 3.2 Representation of hybrid photoanode deposition process.

The grown hydrothermal layer was treated with aqueous 0.2 M of $TiCl_4$ solution at 30˚C for 24 h BL to allow the integrity of the contact points. With the integration of a buffer layer between NR and NPs, a hybrid device, S5 was obtained.

After all deposition stages, heating was applied. With the effect of heat, the organics in the environment are burned, leaving behind a void.

The prepared photoanodes and CEs were clamped together. A liquid electrolyte contains

0.6 M BMIMI, 0.5 M TBP, 0.05 M I2, 0.1 M GTC in 85:15 volumetric ratio of acetonitrile and valeronitrile solvents.

Five batches of Pt films, seed layers and TiO_2 films were prepared under identical conditions. The average results and the selected results will be discussed in Chapter 5.

3.3 Thin Film Deposition Methods

This section covers the thin film deposition methods used in this study. Chemical bath deposition, hydrothermal growth and spin coating will be described, respectively.

3.3.1 Chemical Bath Deposition

Chemical bath deposition (CBD) is a simple and practical method to obtain thin films. This is a kind of wet chemical process. This process requires no vacuum, pressure, or complex instruments, and it makes this method highly attractive to researchers. The details of the process depend on the type of material being used, but generally, the material will be dissolved in a liquid or gas and then deposited onto a substrate in a chemical bath. This technique is mostly preferred for thin film studies with its comparable quality to other expensive methods. The targeted thickness with this deposition method is highly dependent on solution time and molarity.

3.3.2 Hydrothermal Growth

The word hydrothermal, in its technical sense, first brings to mind high temperature and high pressure concepts. These two words are also the magic for that method. This method includes liquid solvent, theoretically water. With a high temperature and pressure condition, water arrives a supercritical point. This point refers to an interesting mixture of the phases because at the high temperature and pressure, the inter-atomic bonds are broken and reconnected in a different equilibrium point, resulting in enormous novel nanostructures. The other supporting chemicals have a power to control over the hydrolysis ratio of the precursor. It is possible to obtain a powdered particle synthesis or the structures grown directly on a surface with this method. Experimental parameters that affect the final product can be listed as reaction temperature, time, acidity of the solution, precursor utilization rate, position of the substrate (up or down, angled position, etc.) in this method. Production conditions do not require very high technology. High pressure and chemical resistant sealed containers are sufficient. It is the most salient feature of the such a simple method is that high crystal quality anhydrous, crystalline particles resulted. In addition to the particle sizes, the morphology can also be controlled. The morphologies that can be

achieved with this method have a very wide range from spherical particles [73] to rods [74], and from wires [75], to nanotubes [76].

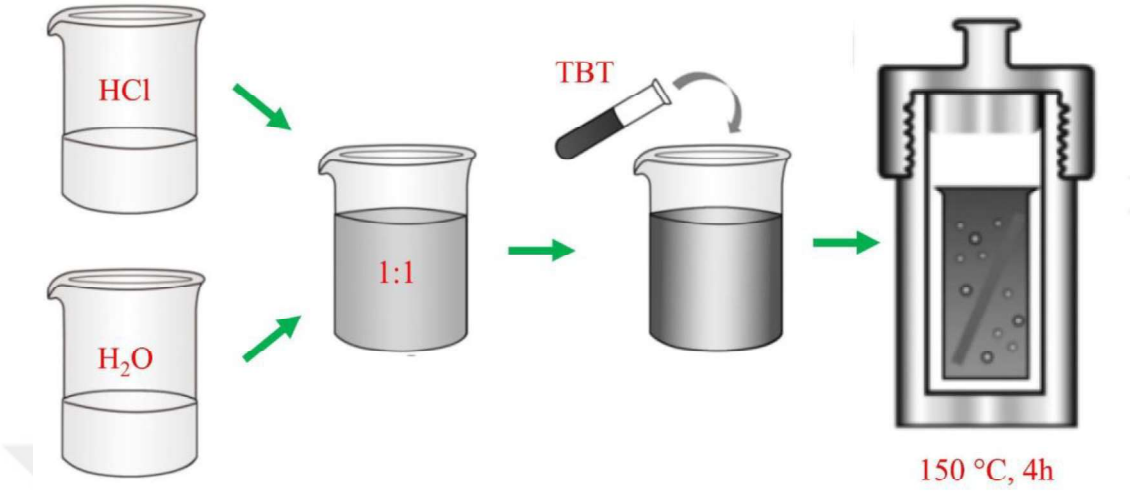

Figure 3.3 Representation of hydrothermal process steps (modified from [77]).

Rutile formation is strongly supported in a highly acidic environment in the hydrothermal method [78]. Titanium salts, which are used as the starting source of the NR array, react with water very quickly. The acid utilized in the experiment controls the TiO_2 hydrolysis and nucleation rate in the synthesis. It is critical to maintaining the hydrolysis ratio under control. Otherwise, TiO_2 can be completely hydrolyzed with water very quickly. This process will eventually result in irregular titanium structures of various sizes and shapes. In the presence of any acid, it is anticipated that the crystal forms rutile nanorods in a specific orientation if specifically Cl ions are present in the aqueous medium [58].

3.4 Characterization Methods

This section contains how the properties of the deposited films, and fabricated devices are evaluated. Most of the characterizations were conducted in laboratories of the Department of Energy Systems Engineering, Ankara Yıldırım Beyazıt University (AYBU), Ankara, Turkey except X-ray diffractometry. It was measured at the Department of Metallurgical and Materials Engineering in the same university. Field emission scanning electron microscopy was accomplished at AYBU Central Laboratory.

3.4.1 Optical Characterizations

UV-vis spectroscopy is a technique that allows measuring transmittance, absorption, and reflectance that informs about the optical properties of the film. Summation of all these possible states of matter-light interactions are equal to one.

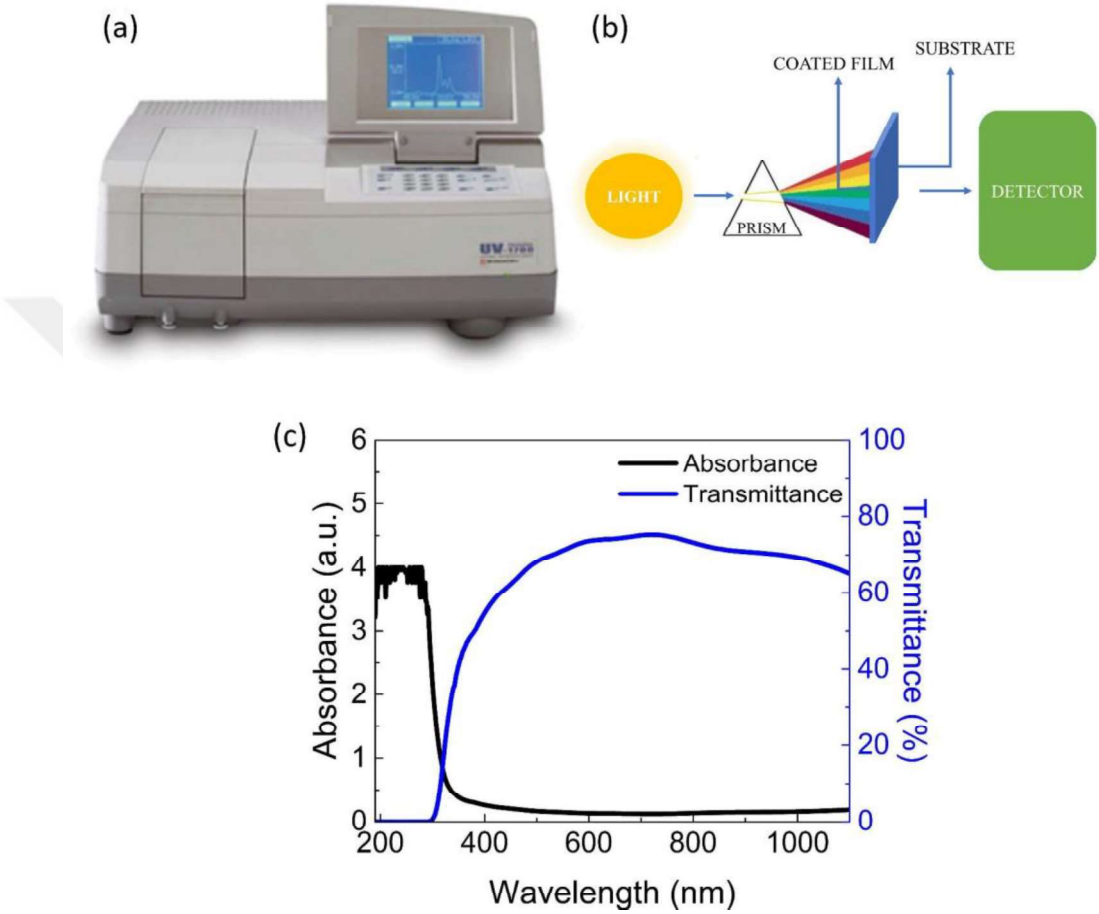

Figure 3.4 (a) UV-vis device photo (b) Schematic of UV-vis spectrophotometer device (c) an example UV-vis plot of FTO substrate.

The computer-controlled Schimadzu 1700 model device was used in this study. This device can measure the transmittance and absorbance in the wavelengths between 190 nm and 1100 nm Figure 3.4. It is controlled by software called UV Probe.

A monochromator is an optical device that splits the light beam source and sends it to the material at a specific range of wavelength. During the measurement, the light transmitted to and passing through the film is recorded as with percent sensitivity. By measuring the transmittance data as a percentage, the absorption profile can be

estimated by ignoring the reflectance. The absorbance unit is considered to be an arbitrary unit.

3.4.2 Structural Characterizations

X-Ray Diffractometry (XRD) is a non-destructive method to investigate the structural properties inside the material. Atomic and molecular identities can be discovered with this method.

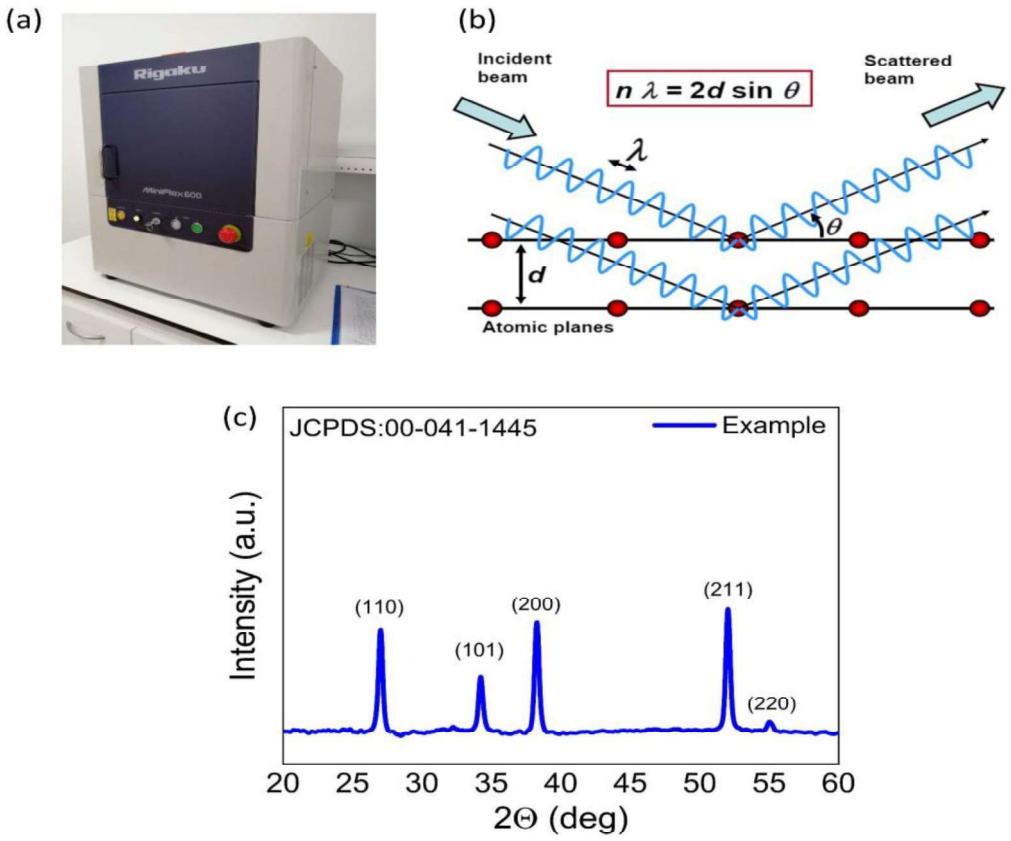

Figure 3.5 (a) A photo of XRD device, (b) an schematic of Bragg's law [79] (c) an example XRD diffraction of FTO substrate.

The incident X-rays diffract on a film or powder material to a known degree. The measurement was performed as a scan with a predefined scan rate. In this work the theta (2θ) adjusted from 20 ˚ to 60 ˚ scan at the speed of 4 ˚/min and step size of 0.02˚.If there is a match with a direction in the specific angle and crystalline plane, then a peak point appears on the plot. High intensity narrow peaks indicate high crystal quality. With this characterization method, many properties of films such as chemical composition, amorphousness, single or poly crystallinity, crystal defects, doping atoms, crystallographic orientation, lattice parameters, grain size, etc. can be examined. In

addition, information about the content of unknown material can be obtained by using diffraction spectrum and JCPDS (Joint Committee on Powder Diffraction Standards) cards without damaging any sample.

3.4.3 Morphological Characterizations

Morphological characterizations in this work cover two different microscopic methods: atomic force microscopy and field-emission scanning electron microscopy.

Atomic force microscopy (AFM) is a technique that allows getting topographical information about the films. The film sample is scanned in x-y directions line by line. The device has a special piezo material (tip on the edge of the cantilever) to sense the surface height. When the sample film is close enough to the tip, then the film is bound to the tip of the cantilever. The cantilever moves as a result of the pushing or pulling force exerted on it by the atoms. A laser beam is spotted onto the tip and the position of the reflected beam changes related to the height pattern. This gives a z-direction height information throughout x-y directions. The reflected laser beam is also detected with a detector. The software connected to the computer monitors this movement and saves the z plane data for scanning in the x-y planes. The device utilized in this work is Quesant Q-scope AFM. There are three different working modes: contact, non-contact and taping. Contact mode may destroy the film surface during the measurement. Thus, the non-contact mode was selected for our studies. An example of the device photo, the illustration of the working principle and an example of a topographical image are delineated in Figure 3.6. As can be deducted from the example measurement graph, the color indexed height information is obtained up to a few microns.

Field-emission scanning electron microscopy (FE-SEM) is a powerful microscopy technique that allows the analysis of the surface morphology by accelerated high-energy

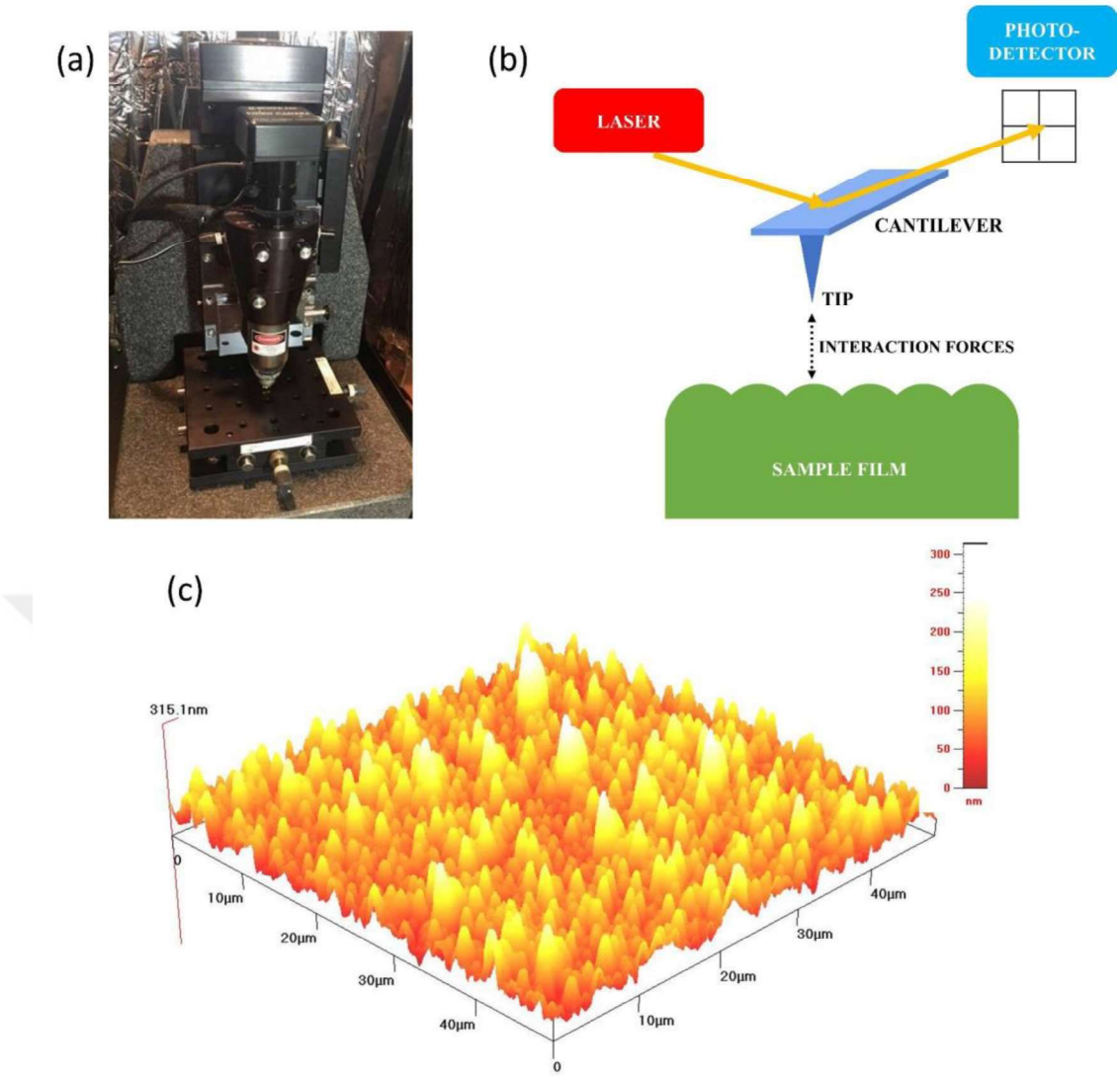

Figure 3.6 (a) A photo of AFM device, (b) schematic of AFM working principle (c) an example image taken by AFM.

electron beams from the surface of the film. It measures the size, shape, thickness and roughness of the objects. It allows measuring even the small details of an object that is not possible to see with the naked eye. Inside the device, an accelerated electron beam interacts with the sample and finally produces an image of the surface on a screen.

This measurement can provide information on surface properties, particle sizes, and porosity for both of the electrodes. Furthermore, under appropriate conditions, the thickness of the films can be estimated. Hitachi SU5000 model FE-SEM device was used in this study. Figure 3.7 shows device photo, working principle schema, and an example SEM image. A free software, Gwyddion, was used to determine the particle sizes on the SEM image.

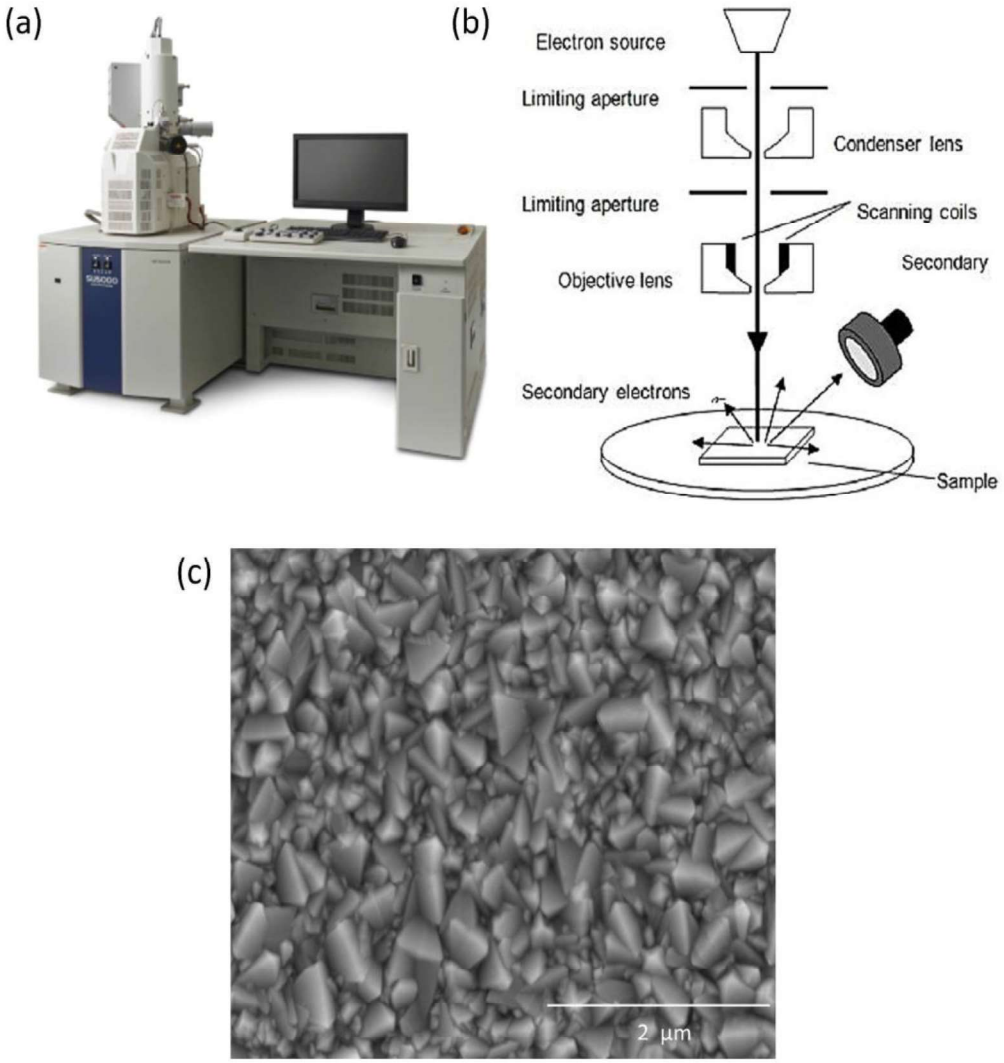

Figure 3.7 (a) Photo of SEM device [80], (b) schematic illustration inside of the SEM device [81] (c) an example SEM image of FTO film surface.

3.4.4 CV Measurement

This technique measures the current response of the films, by scanning in a potential range at a predetermined speed from one value to another, then back to the starting point. It is a quite amenable technique to determine the reduction and oxidation potentials. The measurement is carried out in an ionic liquid in the presence of a working electrode, CE and an Ag/AgCl reference electrode. It was conducted with a Gamry 1000E device and the analyzes were made with its special software. Measurements can also be recorded in the target voltage range, at different scan rates, or with multiple repetitions. The Figure 3.8 shows the photo of the test station, measurement set up, and an example

plot of CV. Analysis of these voltammograms reveals the electrochemical stability of CEs. [82].

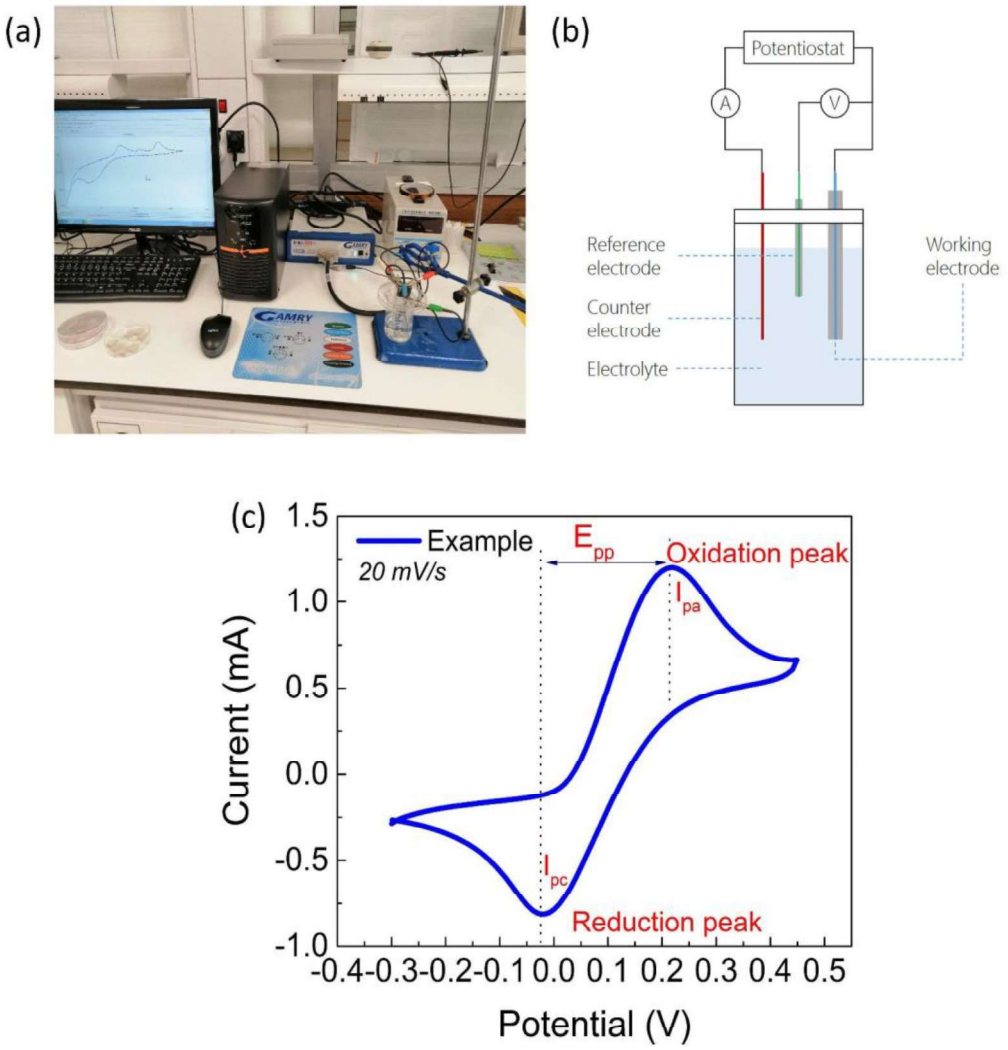

Figure 3.8 (a) A photo of the test station, (b) cyclic voltammetry measurement configuration [83], and (c) an example cyclic voltammogram.

A turning point appears on the bottom of the x-axis shows a cathodic reaction and the upper side shows an anodic reaction on the electrode. The corresponding current and voltage values are denoted as cathodic current (I_{pc}) and cathodic potential (E_{pc}) which are associated with reduction of I^{-}_{3}. The ΔE_{pp} corresponds to a peak to peak potential difference potential between the oxidation and reduction peaks.

3.4.5 Tafel Polarization Measurement

Tafel polarization is a characterization tool to investigate electrical properties. The

same Gamry 1000E device is used to measure the Tafel polarization in the experiments. Symmetric film electrodes were combined in a dummy cell form and evaluated towards the negative and positive regions of voltage. Considering the current response of a film towards applied potential the graph divided into 3 regions: These zones are lower potential (<±0.12 V), middle potential (Tafel zone) and higher potential (diffusion).

The J_0 is the exchange current density and J_{lim} is the limiting diffusion current density values, respectively. The slope of the anodic/cathodic polarization can be used to approximate J_0, while the anodic curve's intersection with the y-axis can be used to determine J_{lim}.

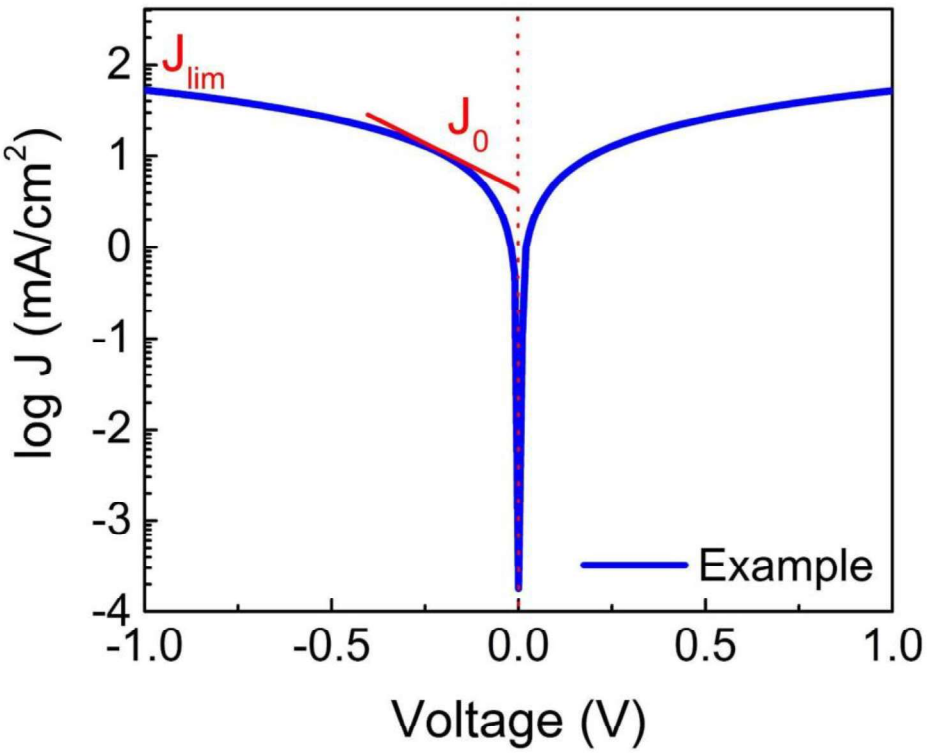

Figure 3.9 An example of tafel plot.

3.4.6 EIS Measurement

The electrochemical interface spectroscopy (EIS) is a technique that provides analysis information about the current response of the device against the low AC voltage applied on it and the resistance (R), capacitance (C) and inductance (L) of the device at its interfaces. Impedances were obtained using a potentiostat device (Gamry, 1000E) and

analyzed in the related Gamry software.

Two different types of plot can be produced with this measurement which are nyquist and bode plots as shown in Figure 3.10. Nyquist plot is the representation of the real and imaginary resistances. The Bode plot shows the frequency dependent phase transitions of the system.

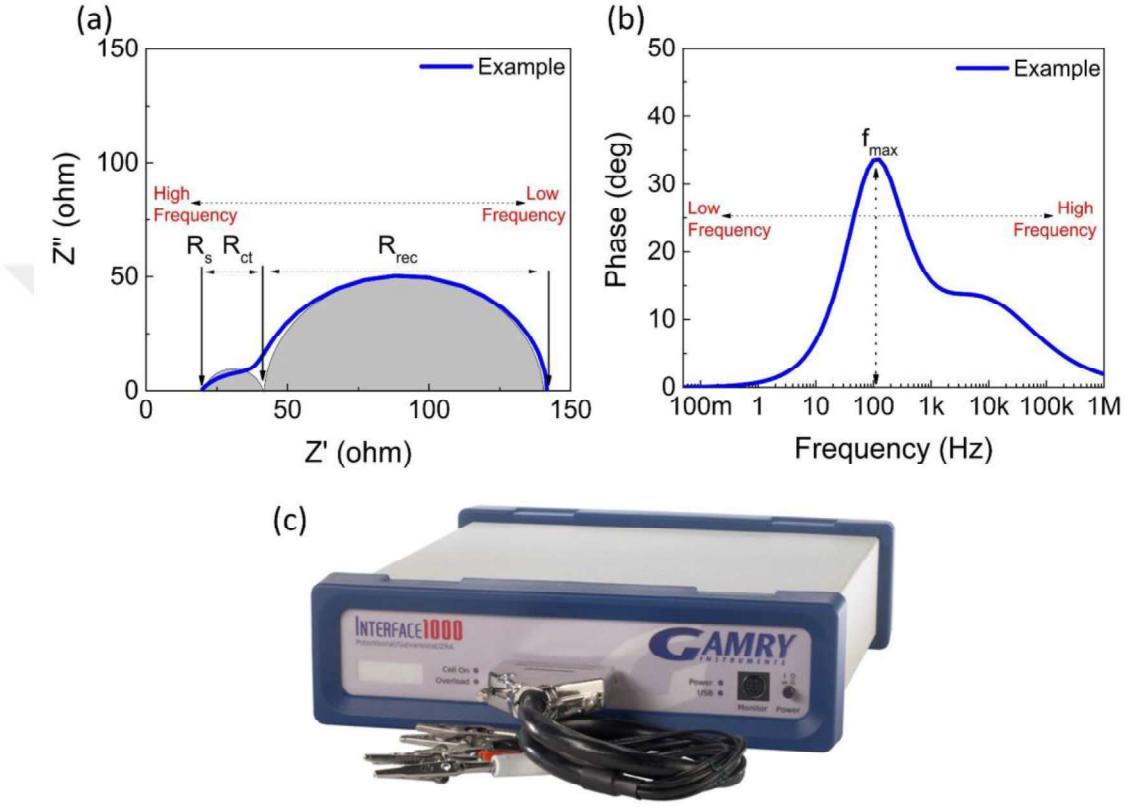

Figure 3.10 (a) A nyquist plot of the EIS measurement, (b) a Bode plot of the EIS measurement, and (c) a photo of the device [84].

The setup configuration should comprise a photoanode and a CE with electrolyte in order to evaluate a device using this measurement. The measurement is conducted in frequency dependency and gives the real and imaginary resistance results. The measurement data is evaluated with a specific equivalent circuit model shown in Figure 3.11 [85, 86]. This model also symbolizes the interface resistances between the layers. For a typical DSSC, the model contains three resistances: series (R_{s-eis}), charge-transfer (R_{ct}), and recombination (R_{rec}). R_{s-eis} corresponds to the first intersection point on the real axis in the high-frequency region. R_{ct} corresponds to the difference between the first and second intersection points. R_{rec} is the difference between the second and third point intersecting the real axis. The selected

measurement frequency region varies from 0.1mHz to 1MHz.

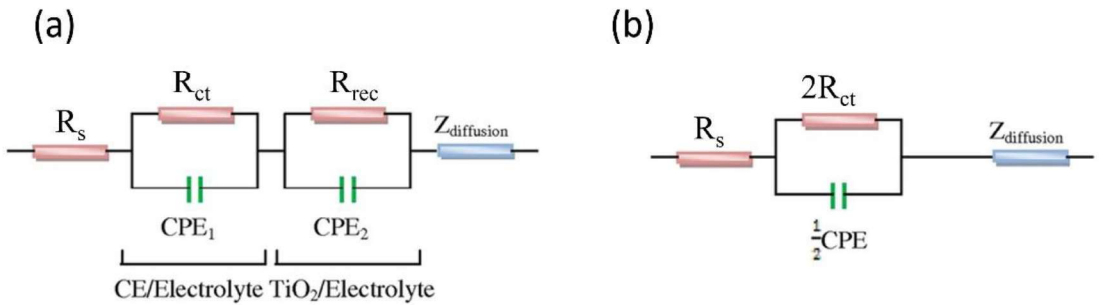

Figure 3.11 (a) An equivalent circuit of device modified by [85], (b) an equivalent circuit of dummy cell for Pt films [85].

A symmetric dummy cell measurement should be performed if a focus needed on the performance of any of the electrodes. Two identical films (CE/electrolyte/CE) are assembled into a device configuration in this study in order to investigate the interfacial charge-transfer kinetics of the CEs. This time the equivalent circuit model covers two resistances as series (R_s), charge-transfer (R_{ct}). The selected measurement frequency region varies from 100 Hz to 10kHz.

3.4.7 Electrical Characterizations

Electrical characterizations are sheet resistance measurements for the films and I-V measurements for the DSSCs.

The sheet resistance of a film can be measured with a four-point probe system (Lucas Lab) as shown in Figure 3.12. The unit of the sheet resistance is ohm per square. This device is connected to a sourcemeter (Keithley, 2400) to determine the sheet resistance of the deposited films. This technique lay out measuring the current and voltage in defined four-point probes.

Testing for mechanical adhesion is another application for this measurement method (sheet resistance). It provides data on the mechanical stability of the coated film. Weight is applied to a tape glued to the film surface to achieve effective adherence. The sheet resistance measurement is then repeated to see if the removed tape causes deformation in the film.

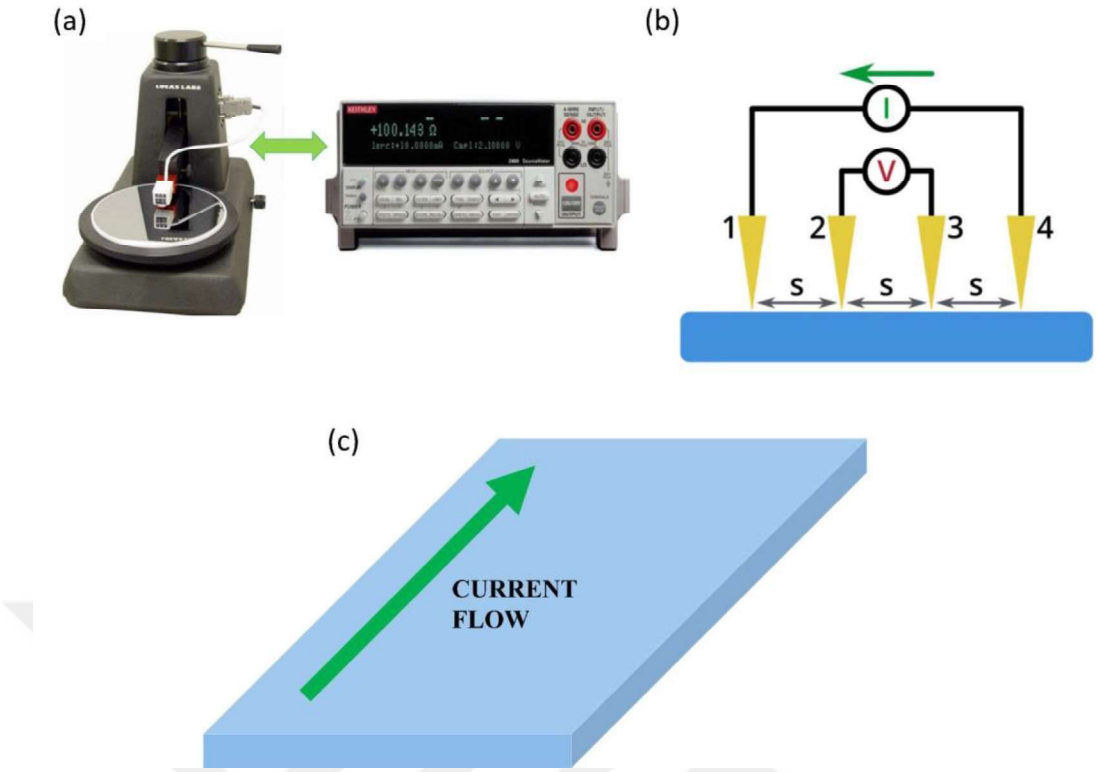

Figure 3.12 (a) A photo of sheet resistance measurement system, (b) a schematic illustration of the four point probe device (c) a representation of the measurement direction.

The overall device performance was evaluated with a I-V measurement setup. In this method, the measured current value is recorded under forward potential scanning. The fact that the device's I-V characteristics indicate a negative current at a positive voltage region dependent on light illumination is proof that the developed device is a solar cell. It corresponds to the fourth region of the I-V plot. In this work, ABET 10500 low cost solar simulator was combined with the same sourcemeter to have an I-V test station. The sourcemeter controls the voltage and the corresponding current was recorded with free software (Kickstart) under the incident light. The standardized measurement was carried out under AM 1.5, 1000 W/m^2 of sunlight simulation. An example of a test station and a working principle schema and an example plot are illustrated in Figure 3.13.

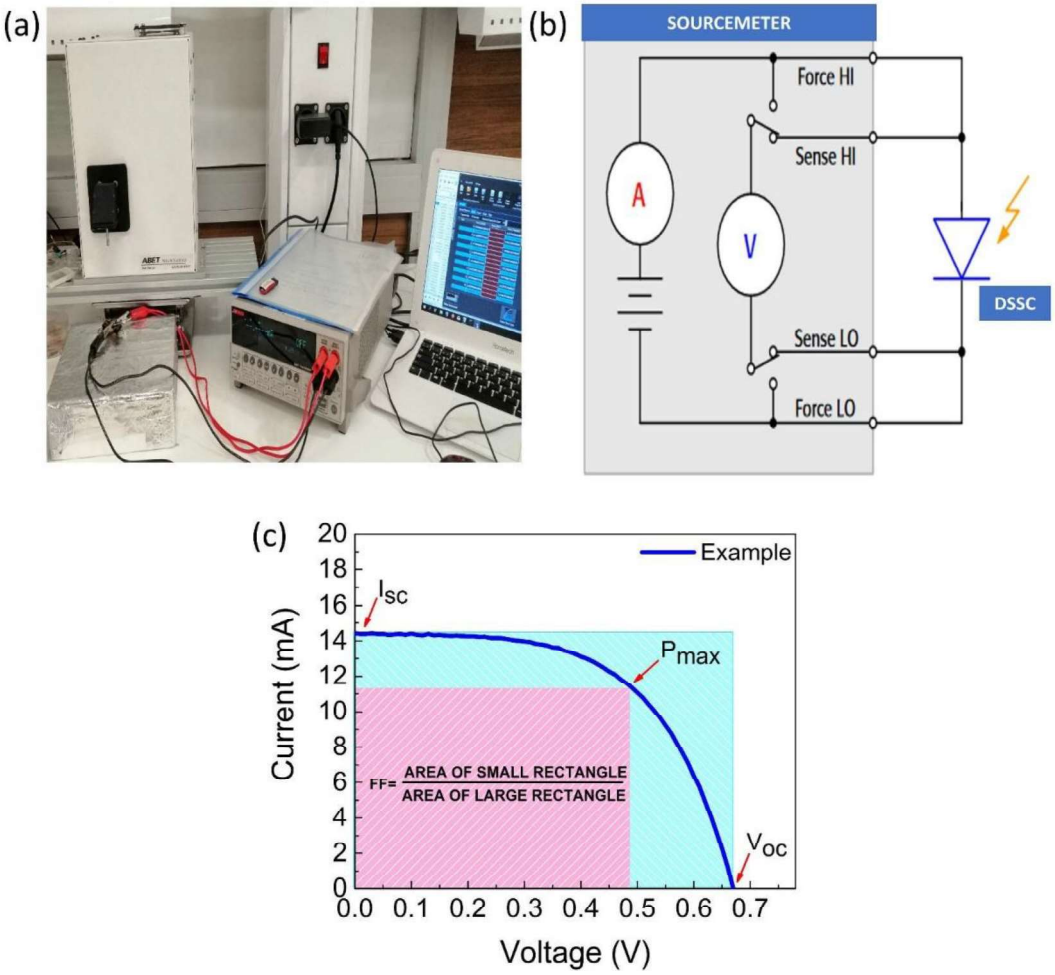

Figure 3.13 (a) A photo of I-V test station and, (b) working principle of the sourcemeter modified from [87] (c) an example of I-V plot.

CHAPTER 4

THEORETICAL CALCULATIONS

This section describes how the data obtained from the characterizations contribute to the evaluation of the film or device performance in the light of theoretical knowledge.
Electrical Analysis on Device Performance

The evaluation parameters on the device performance are short circuit current I_{sc}, short circuit current density J_{sc}, open circuit voltage V_{oc}, fill factor (FF), and power conversion efficiency (η). The maximum recorded current value is referred to as the I_{sc} at the location where the externally applied potential value is zero. To eliminate the effect of device area, measured current is divided into area and the J_{sc} was obtained as shown in Equation 4.1.

$$J_{sc} = I_{sc}/area \tag{4.1}$$

The point where the external circuit potential is equal to the maximum potential of the cell and no current occurs is called the V_{oc}. In other words, it also corresponds to a turning point as the current changes from negative to positive under the applied voltage.

FF is a metric how much the measured current and voltage curve resembles a square. It can be calculated as a ratio of multiplication of maximum current and voltage over multiplication of I_{sc} and V_{oc} as shown in Equation 4.2.

$$FF = I_{max} * V_{max} / I_{sc} * V_{oc} \tag{4.2}$$

The device efficiency is the ratio of the electrical power it can produce in response to the light power on it.

$$\eta = P_{max} / P_{in} = V_{max}.I_{max} / P_{in} = V_{oc} * I_{sc} * FF / P_{in} \tag{4.3}$$

A solar cell can be modeled using a single diode circuit model. In the circuit, the DSSC corresponds to a diode and creates a current in one direction under sunlight. The resistances of series (R_s) and shunt (R_{sh}) represent the parasitic parts in the device. R_s consists of ohmic losses at the point of contact with metal junctions. R_{sh} represents the alternative multiple paths that lead to current splitting.

R_s and R_{sh} have a direct effect on FF of the device. But note that when the R_s is high, then the high R_{sh} is not sufficient to control the current [88]. Because R_s is serial resistance and the electrons are mandatory to face with that of the high resistance on the way. High value of R_s lowers the the J_{sc} value. Lower R_{sh} value leads to an decrease in J_{sc} rather than V_{oc}. The explanation of this case is that there is more than one suitable path between two contact points, and this leads to division of the current.

$$R_s = (I_{sc} - I_{max}) / (V_{max} - 0) \tag{4.4}$$

$$R_{sh} = (I_{max} - 0) / (V_{oc} - V_{max}) \tag{4.5}$$

Until now, the I-V analysis has been performed under ordinary light illumination. However, the analysis of the I-V measurement under dark conditions, gives an information about device stability and diode characteristics such as leakage current [82]. This dark current has an opposite direction the photo-generated current and has a relationship with V_{oc}. The higher leakage current means a lower value of V_{oc} in the device.

The net current can be considered as the sum of the dark current and the photo-generated current as depicted in Equation 4.6.

$$J_{net} = J_{sc} - J_{dark} = J_{sc} - J_0 \tag{4.6}$$

The following subsections explain how structural, optical, morphological, catalytic properties affects the electrical performance of the device theoretically.

4.1 Structural Analysis on Device Performance

Crystalline size can be calculated with the data extracted from XRD measurement by the Debye Scherrer formula as shown in Equation 4.7 [89, 90].

$$d = k\lambda / \beta cos\theta \tag{4.7}$$

where d is crystalline sizes, k is a constant (0.94), λ is the X-ray wavelength (1.54 A, Cu α radiation), and β is the full width at half maximum (FWHM) of the peak.

The crystallite size is inversely proportional to grain boundaries. Namely, the bigger the crystallite size is, the less the number of grain boundaries in a film. This is important because each of the grain boundaries is an obstacle for the electron throughout the

transport and lowers the J_{sc} and decrease the performance [91].

Another reflection of the higher grain sizes can be correlated for the electron lifetime parameter achieved by EIS measurement. Electron lifetime is the longest path time for an electron without facing an obstacle. When the grain size is larger, then electron transport longer time and it means the film has a higher electron lifetime [92]. The high crystallinity of the nanorod structure also ensures the fast electron transmission [63]. It extends the maximum path that the electron can take without recombination, which in other words is the lifetime of the electron.

Another formula related to XRD measurement data is on weight percentages of the phases. As stated, before in Chapter 2, TiO_2 has three different phases: anatase, rutile, and brookite. The distribution of those phases can be determined with the Spurr's Equation 4.8 [93, 94] in a weight percentage as given below:

$$\text{Weight of anatase: } 1/\left(1+1.26*I_{rutile}/I_{anatase}\right) \tag{4.8}$$

where the $I_{anatase}$ and I_{rutile} is the intensity of the peaks anatase or rutile. This information makes the understanding of the electronic band states. Knowledge of this distribution can provide an interpretation of its electronic properties. For example, it is known that the presence of the anatase phase in the photoanode supports dye absorption relative to the rutile phase. Or, the dominance of the rutile phase may again be proof that the electrical conduction will be faster.

4.2 Optical Analysis on Device Performance

Optical measurements are constructed to determine the extent to which the film transmits, absorbs or reflects the light. The wavelength range corresponding to the absorption of the film provides an analysis of its electronic band structure properties. For example, the E_g of the material can be determined from the absorbance measurement with the following Equation 4.9.

$$E_g = h.v = h.c/\lambda_{onset} = 1240/\lambda_{onset} \tag{4.9}$$

The obtained E_g value is especially important in the evaluation of the photoanode component. Depending on the different morphological features and the dominant phase, the E_g value can be different. For example, the anatase phase has an E_g of 3.2

eV, while 3.0 eV for the rutile phase. The determination of this parameter is important for the evaluation of optical properties. In addition, the V_{oc} value of the device is also affected depending on the band gap and the associated Fermi level. Since V_{oc} is by definition dependent on the fermi level and the redox level of the electrolyte, a higher V_{oc} is predicted for the higher fermi level [95].

4.3 Morphological Analysis on Device Performance

A higher root mean square (RMS) roughness value indicates a higher active surface area [96]. Having a higher surface area for the both case of photoanode and CE, are desired [97]. The higher roughness is reported to decrease in electron mobility due to scattering [98, 99]. First of all, it means that the interactions between the light matter will be changed and for a photoanode, a higher surface area means a higher dye loading. For a CE, a higher amount of reaction sites increases the catalytic activity [100].

4.4 Sheet Resistivity Measurement on Film Quality

The Equation 4.13 is applied to analyze the measurement results.

$$R_{sheet} = (\pi . V) / (I . ln2) \tag{4.10}$$

where R_{sheet} is sheet resistance, π over ln2 is a geometric constant, V is voltage and I is current. With this constant this measurement becomes independent over size of the film and provides a strong characterization on electrical properties. Measurement should be repeated multiple points to fair evaluation of the coating. The average of the measurements makes available comments on grain size. For example, smaller grain size leads to higher sheet resistance of the film [101].

4.5 Catalytic Activity on Device Performance

The reaction stated in Equation 4.11 occurred in a CE surface is a cathodic reduction. This allows for the reduction of triiodide of the electrolyte sufficiently. This catalytic activity that CE has can be measured in three different techniques (CV, Tafel Polarization, EIS) explained in the previous chapter (Chapter 3).

$$I_3^- + 2e^- = 3I^- \text{ (cathodic reaction)} \tag{4.1}$$

CV: Higher I_{pc} value indicates a better catalytic activity. Redox peak currents and the square root of the scan rates expected to be in a linear trend. This linearity validates the only limiting factor is the diffusion of the $I^-/I(_3)^-$ ion pair [102].

Furthermore when the reduction and oxidation peaks are close to each other, in other words, the ΔE_{pp} value is low, it shows the reversibility of the measured reaction [103].

CV measurement explains the catalytic properties of the CE and mostly in accordance with I-V results [104].

Tafel: Better electrocatalytic performance can be achieved with a higher exchange current density (J_0) and a higher limiting diffusion current density (J_{lim}).

If the value of J_0 is lower for a case, the larger value of J_{lim} is expected for the same sample case. There is an inverse relation between them. The value of R_{ct} is an important to evaluate the catalytic activity in a film.

EIS: R_s and R_{ct} values are obtained from EIS measurement. Especially the value of R_{ct} is critical for the CE film quality. Because, the value of R_{ct} is an important to evaluate the catalytic activity in a film. The equation given below is a kind of way for the proof of the trend for the charge transfer resistance R_{ct} obtained with another measurement (Tafel polarization measurement). The highly ordered correlation between the values and group trend is good.

$$J_0 = R.T / n.F.R_{ct} \tag{4.12}$$

where R_{ct} is the charge-transfer resistance measured by EIS. The terms T (absolute temperature), n (number of exchanged electrons), R (gas constant), and F (Faraday's constant) are all used in the formula.

J_0 obtained by Tafel measurement and R_{ct} obtained by impedance measurement are expected to be inversely proportional. As a result of high R_{ct}, low current value can be obtained.

In summary, higher catalytic activity increases J_{sc} and device performance in particular. Indicators of high catalytic activity can be expressed as lower R_{ct} value, higher J_0 and J_{lim} value.

4.6 Figure of Merit Evaluation for Thin Films

The quality of the thin films can be reasonably judged with a specific parameter called as 'Figure of Merit' (FOM). The evaluation of the optical and electrical requirements for a transparent metal oxide film makes easier to select the most appropriate film. Up to now, many versions of this parameter has been progressed in the literature [105–107]. However, the following is the most preferred version developed by Haacke, given in Equation 4.13 [108]:

$$FOM = T^{10} / R_{sh} \tag{4.13}$$

CHAPTER 5

RESULTS AND DISCUSSION

Based on the publication [72] “Opaque Pt counter electrodes for dye-sensitized solar cells", Atli, A., & Yildiz, A. (2022). International Journal of Energy Research, 46(5),6543-6552, this section is reproduced (or “reproduced in part") with permission from International Journal of Energy Research, License 2023 John Wiley and Sons Publisher.

Based on the accepted and soon to be published study [109] “Hybrid TiO_2 nanorods combined with a buffer layer for dye-sensitized solar cells", Atli, A., & Yildiz, A. (2022). Applied Solar Energy, Volume 58, Issue 3, this section is reproduced (or “reproduced in part") with permission from Applied Solar Energy, 2023 by Springer Nature Publisher.

This chapter contains mainly 3 sections to present the experimental results. The first part shares and discusses the outcomes of various techniques to be used as a CE for characterizing deposited Pt films in terms of optical, electrical, morphological, catalytic analysis, and device characterization. The second and the third parts of the chapter cover the development progress on the photoanode. In the first phase, it is necessary to optimize TiO_2 seed layer in terms of optical, electrical, and morphological features. Therefore, the second subsection presents the preliminary investigations for the hydrothermal growth of TiO_2 nanostructures. The results and discussions of optical, structural, morphological, and electrical characterizations of hydrothermally produced hybrid TiO_2 nanostructures are addressed in the final section of this chapter.

5.1 Characteristics of Opaque and Transparent Pt CEs for DSSCs

In this section, the studies on CE selection were presented. Opaque and transparent

Pt films were obtained for the CE by using the chemical bath method and spin coating methods. Optical, morphological and catalytic performances of Pt films were evaluated. Within a DSSC device, these films were used as a CE and the electrical performance of the devices was compared to each other.

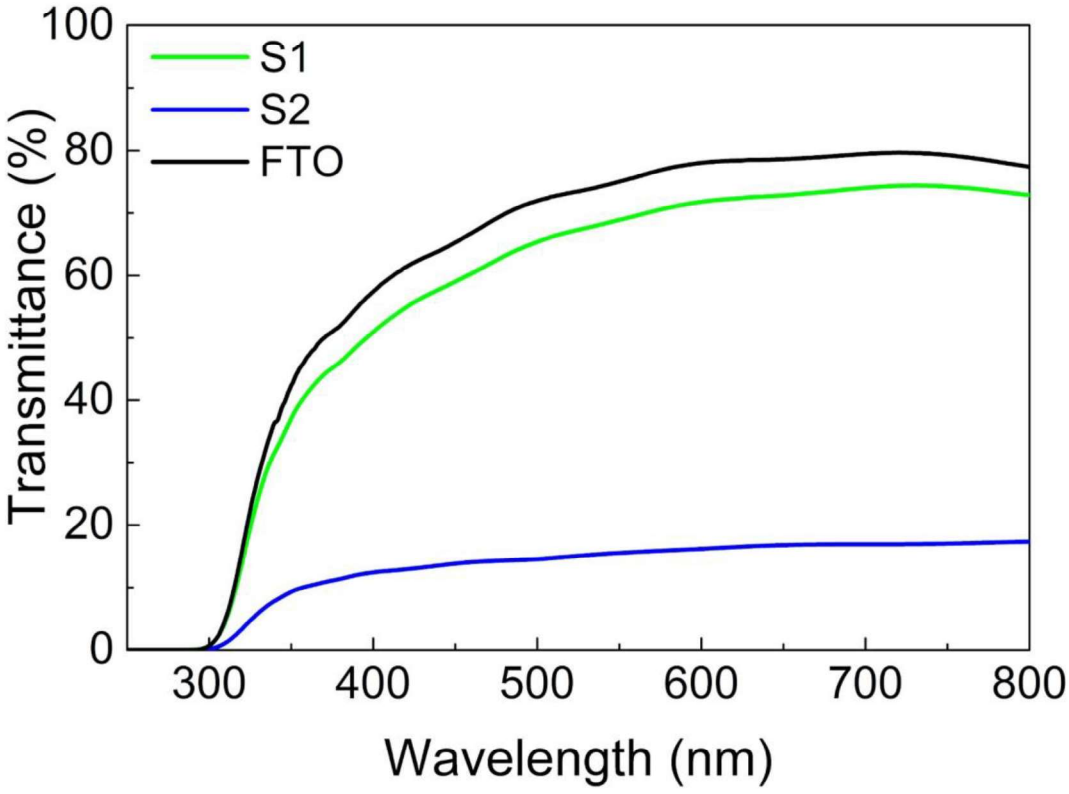

Figure 5.1 Transmittance spectra of S1 and S2 films.

5.1.1 UV-vis Results of Pt CEs

The optical properties of a CE are as much important as a photoanode of the device. Figure 5.1 shows the transmittance spectra of the reference FTO, S1 and S2 films. The transmittance and absorbance measurement results of the films were obtained by two different coating methods: chemical bath, spin coating. The selected method creates a difference in optical characteristics. While the optical transmittance is nearly the same as FTO for the S1 film, it is less than 20% for the S2 film. It is thought that with this decrease in optical transmittance, there should be also a change in absorbance and reflectance as mentioned before in Chapter 2. The difference in absorbance and

reflection is highly dependent on the surface morphological properties. It is expected that with a high surface roughness value of the reflection of the light increases. This case is provided for S2 film. S2 film performs more scattering and reflection of the light. To clarify this situation, an indirect measurement strategy based on absorbance measurement was applied as a next step.

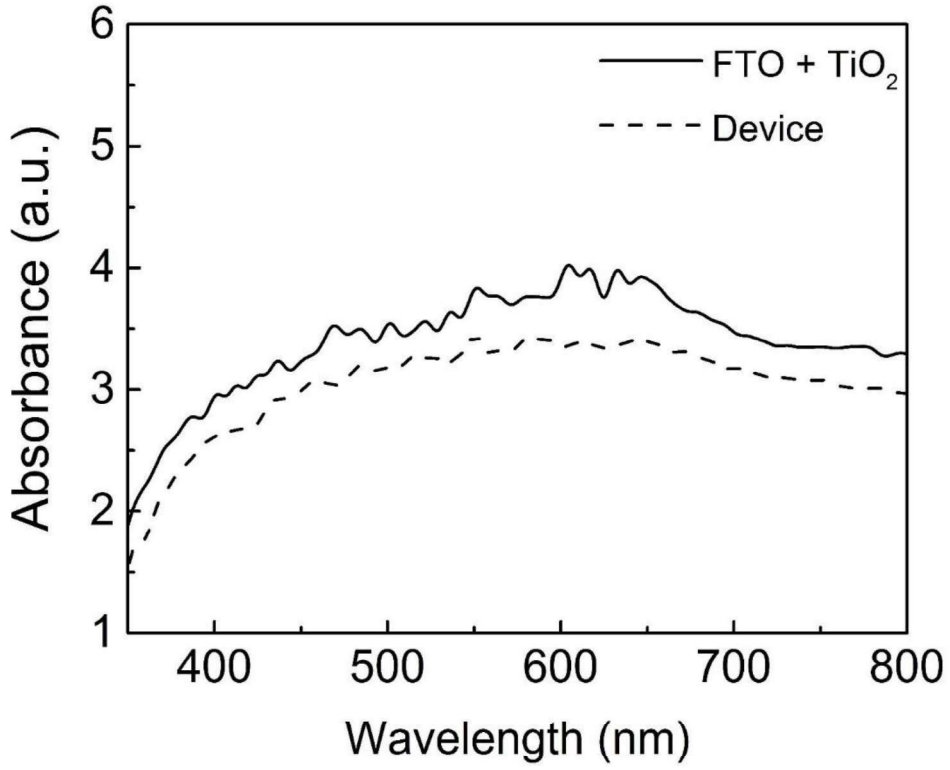

Figure 5.2 Indirect absorbance spectra of FTO and TiO_2 film combinations.

Figure 5.2, Figure 5.3 and Figure 5.4 shows the absorbance spectra of the bare FTO, S1 and S2 films. Figure 5.3 represents a reference measurement. The absorbance measurements performed for the optical evaluation of the device help to understanding and proof of reflective property of the films in an indirect way. For the dye-loaded TiO_2 film, the light came from the glass surface side, and for the Pt-coated film from the Pt-coated film. This provided an opportunity to evaluate the device, just like the operating conditions. First, the combination of these two films (photoanode and CE) was measured and recorded with the label "device". The difference is clearly visible

between operation-stage device and total of the films. The absorbance value decreased significantly in the case of the device configuration. This is due to enhanced reflections on the Pt side that reflect light back to the photoanode layer.

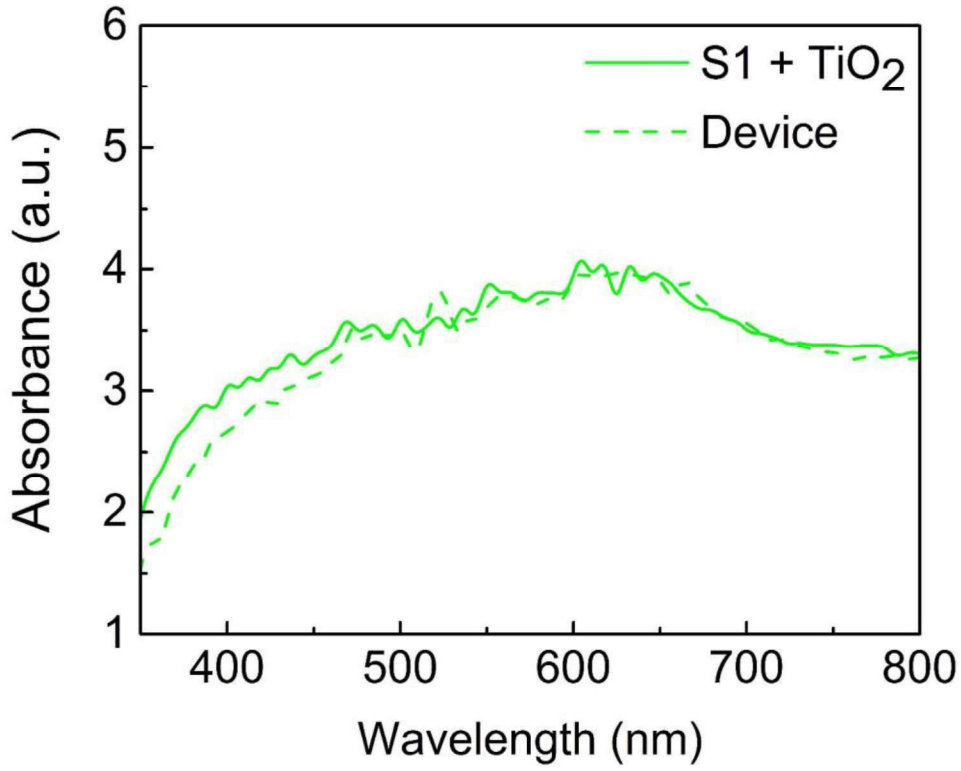

Figure 5.3 Indirect absorbance spectra of S1 film and TiO_2 film combinations.

Figure 5.4 shows that S2 has a higher light harvesting capability than S1 in Figure 5.3 [109]. S2 film, with its mirror effect and enhanced surface roughness, reflected more light. As a CE the S2 film's high reflectivity is anticipated to contribute the device performance in optical aspect.

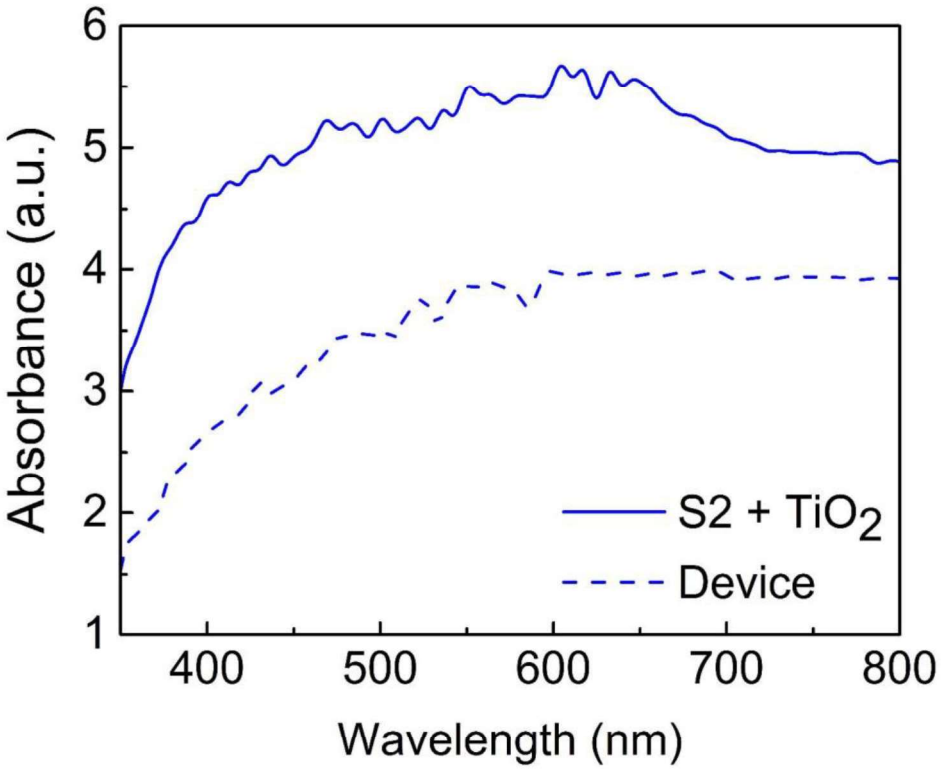

Figure 5.4 Indirect absorbance spectra of S2 film and TiO_2 film combinations.

5.1.2 AFM Results of Pt CEs

Figure 5.5 shows the AFM images of the deposited films. The obtained RMS values are 42 nm and 113 nm for the S1 and S2, respectively. S2 has a high RMS, which suggests a larger active surface area. A high active surface area film implies that catalytic reactions can happen in more areas and result in increased catalytic activity [110].

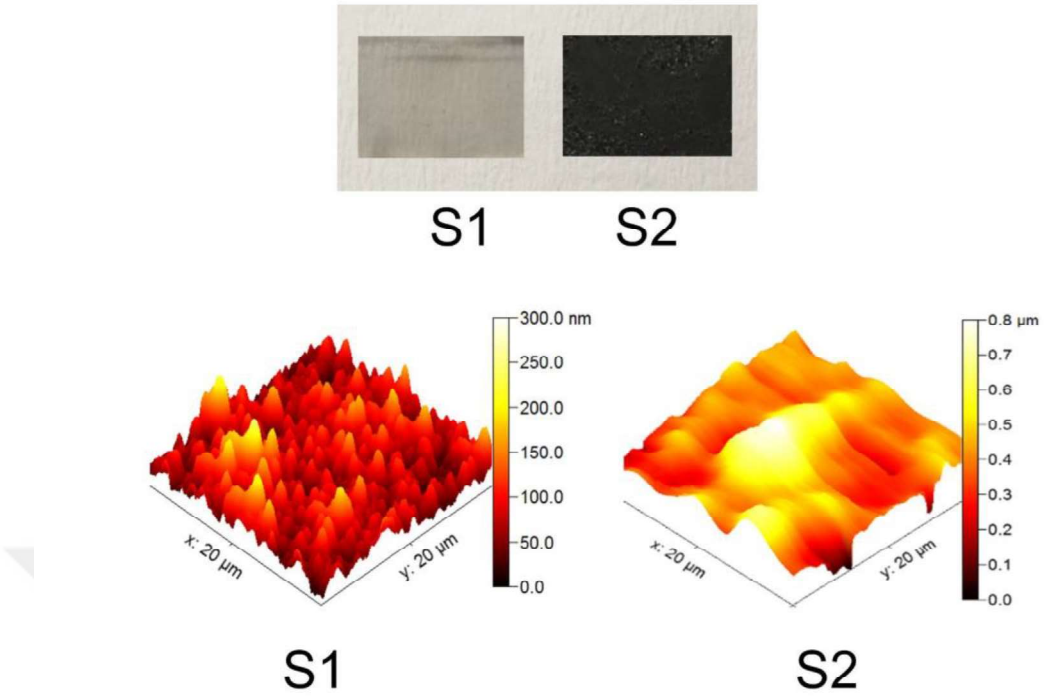

Figure 5.5 Visual photos and AFM images of S1 and S2 CEs.

Figure 5.5 shows the physical photo of the films for a qualitative comparison. Even by looking at these films without any special equipment, it is clear that they vary significantly in appearance. S2 seems different due to its dark opaque black state on a white reference paper, in contrast to S1, which is identical to FTO in appearance.

5.1.3 SEM Results of Pt CEs

Top-view SEM images of the S1 and S2 films and particle size distributions of Pt NPs are presented in Figure 5.6. The mean particle sizes for Pt NPs in S1 and S2 films were determined as 4.72 and 25.87 nm, respectively. It was anticipated that the Pt particles would be uniformly scattered on FTO for the S1 film. However, because of the tiny Pt particles, FTO substrate underneath was still evident for S1 film. The Pt

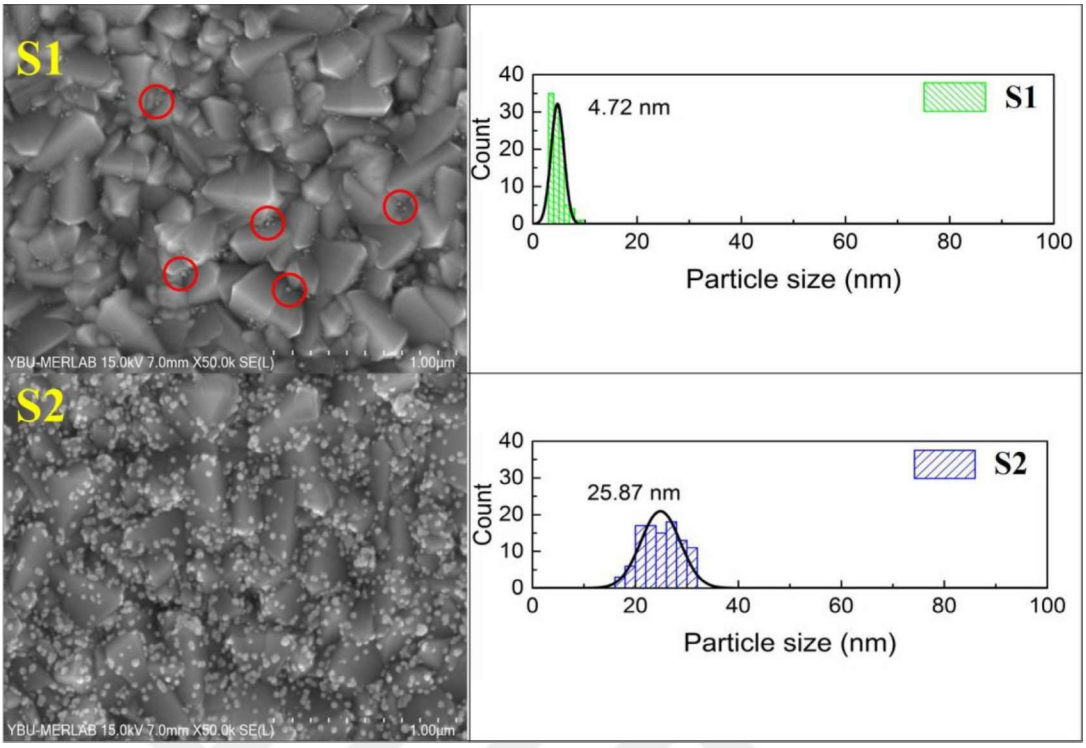

Figure 5.6 SEM images and particle size distribution of S1 and S2 CEs.

particles on S2 film were relatively larger and spherical. A similar view of Pt particles and particle distribution range was reported in an electrochemical deposition studies previously presented in [53, 111].

The literature generally predicts that tiny nanoparticles with larger surfaces will perform better in terms of catalytic activity [112]. However, one should not ignore the detrimental impact of the increased number of grain boundaries brought on by small-sized particles [113]. Evaluation of the catalytic properties with Tafel and EIS would be made the case clearer.

The lower transmittance of S2 can also be attributed to the larger particle size of Pt and its better surface coverage of the particles on FTO [53]. The greater the particles that scatter the light, the longer the optical path of the light becomes [114]. Additionally, when examining the SEM images, high coverage of the FTO establishes a homogeneous film and this increases the possibility of light interactions and reflections. For the CE role, the highly reflective surface of the S2 film and the surface morphology that supports it will be beneficial for the optical path in the device compared to the S1 film.

5.1.4 EIS Results of Pt CEs

Figure 5.7 shows the Nyquist plots of the Pt films. The Table 5.1 contains the detailed impedance values of R_{s-eis}, R_{ct}, and R_{rec}. A smaller R_{s-eis} value of S2 with of 2.17Ωcm^2 means that it has better adhesion on FTO substrate [115]. This value has an effect on the electron flow rate at the CE/electrolyte interface. Encountering a small resistance will improve the reduction reaction performance (I^-/I_{3-}) at the electrolyte/electrode interface. The reported R_{ct} values are 1.44, and 0.89 Ωcm^2 for the S1 and S2, respectively. The order of them is in the range of the findings of the literature [116, 117].

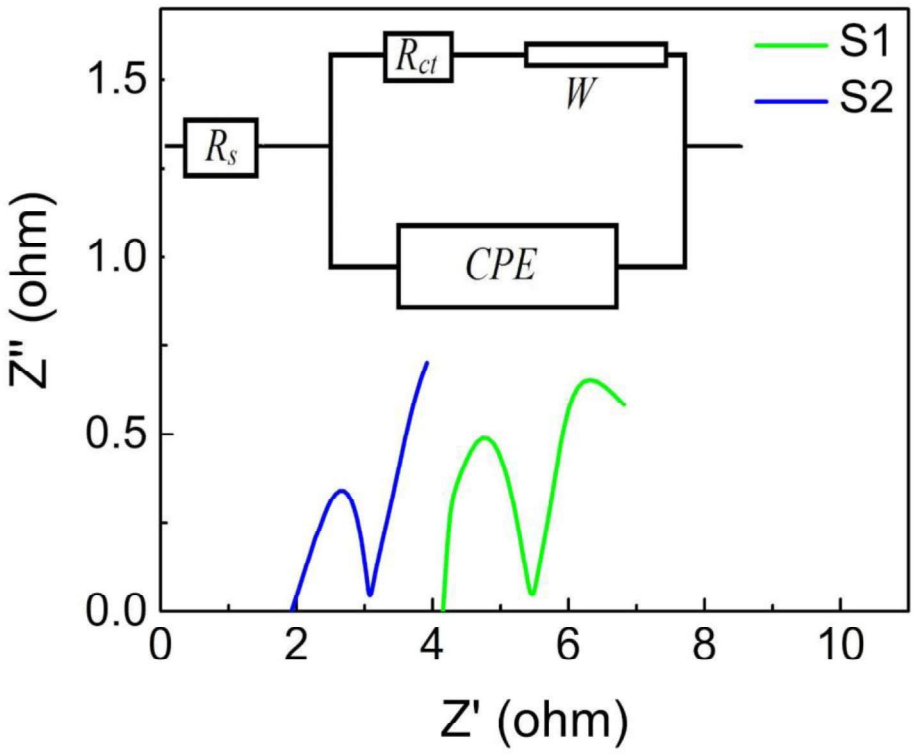

Figure 5.7 Nyquist plot of S1 and S2 films. Inset shows the equivalent circuit of the dummy cell.

5.1.5 Tafel Polarization Results of Pt CEs

Figure 5.8 displays Tafel polarization plots of the Pt films. The estimated parameters of J_0, J_{lim} are listed in Table 5.1.

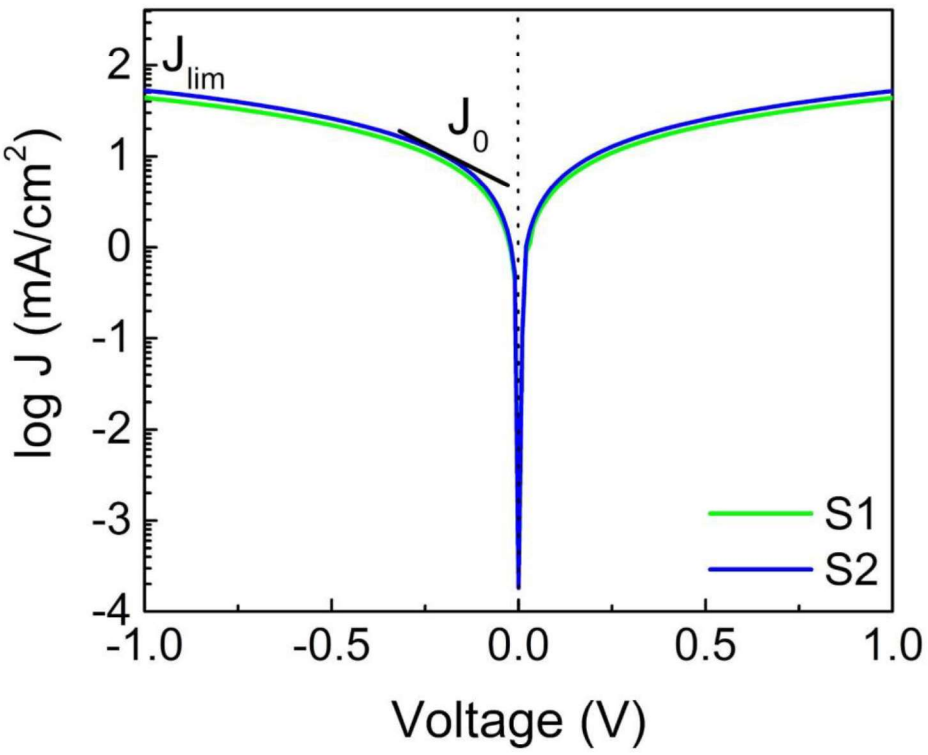

Figure 5.8 Tafel plot of S1 and S2 films.

The value of J_{lim} is 43.85 and 54.32 mA/cm^2 for S1 and S2 in CE, respectively. It means that S2 has a higher diffusion coefficient as in [118] and this explains the higher electrocatalytic activity for the S2 film [119].

Table 5.1 EIS parameters of the S1 and S2 film

Pt film	R_s (Ω cm^2)	R_{ct} (Ω cm^2)	J_0 (mA/cm^2)	J_{lim} (mA/cm^2)
S1	4.02	1.44	3.26	43.85
S2	2.17	0.89	4.12	54.32

As explained in Chapter 4, the J_0 obtained from Tafel was inversely proportional to the R_{ct} obtained from EIS measurements. With the higher values of J_0 and J_{lim} the S2

film. had a higher catalytic activity over S1 film. The reduction peak of I_3^- was higher for S2 compared to the S1 one. Given this situation, overall device performance should be superior for S2 film.

5.1.6 CV Results of Pt CEs

To investigate the catalytic properties, the Figure 5.9 illustrates the CV curves of the S1 and S2 films at a scan rate of 50 mV/s in the potential interval of −0.3 to 0.45 V. For the S1 and S2 films, the I_{pc} values were −0.56 mA and −1.18 mA, respectively. With a higher I_{pc} value, S2 has better catalytic activity than S1. These CV results also validate the I-V results in a similar trend to the literature. [104].

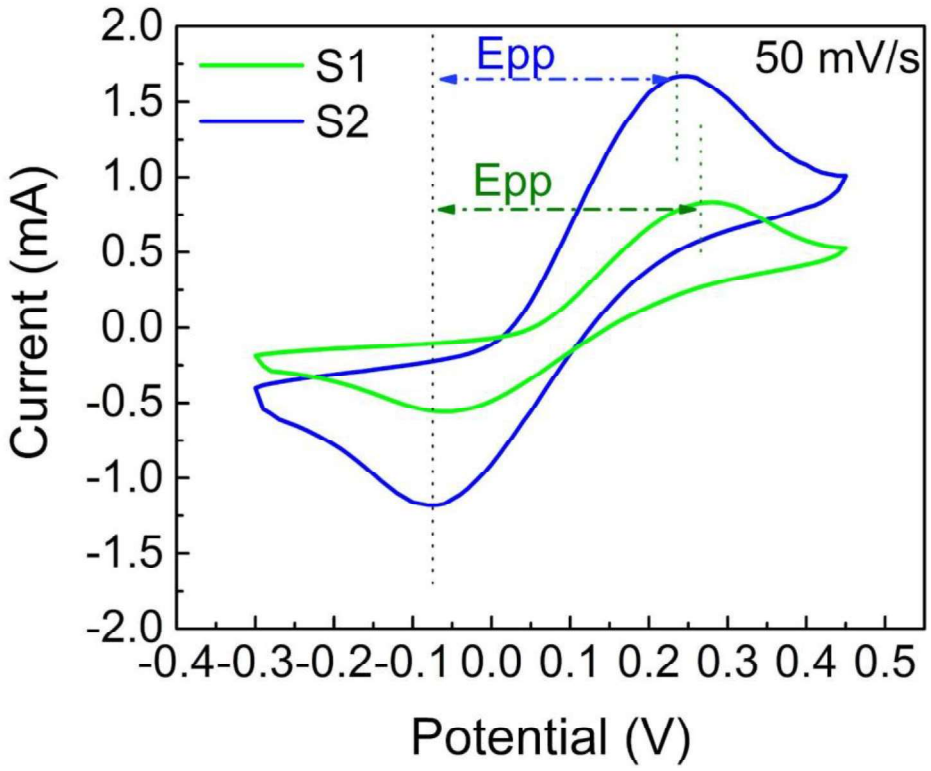

Figure 5.9 Cyclic Voltammograms of S1 and S2 films at 50 mV/s scan rate.

The relationship between the redox peak currents and the square root of the scan rates is shown in Figure 5.10, which should be a linear trend. Investigated scan rates are of 10, 25, 50, 75, and 100 mV/s.

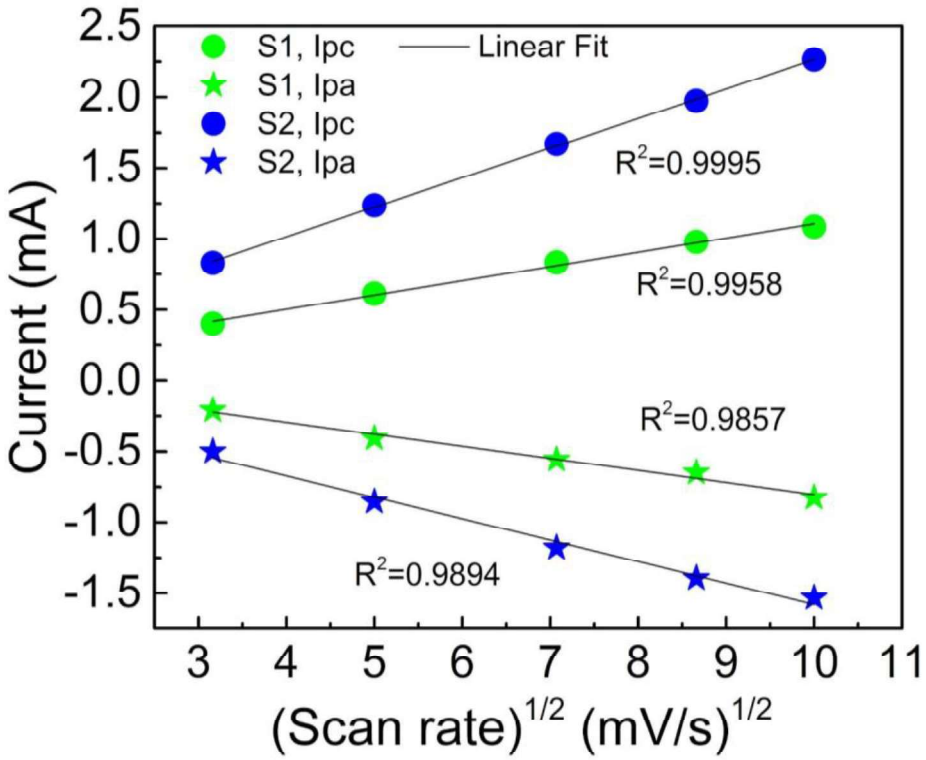

Figure 5.10 Root of the scan rate of CE vs anodic and cathodic current of CEs

Figure 5.11 shows the test results to examine the electrochemical stability of the films with 100 continuous scan cycles. Sudden current drops can be expected if the film is unstable. The fact that there is no fluctuation in any current value in the voltage range determined in repeated measurements is proof of the stability of the film against I^-/I^- reaction.

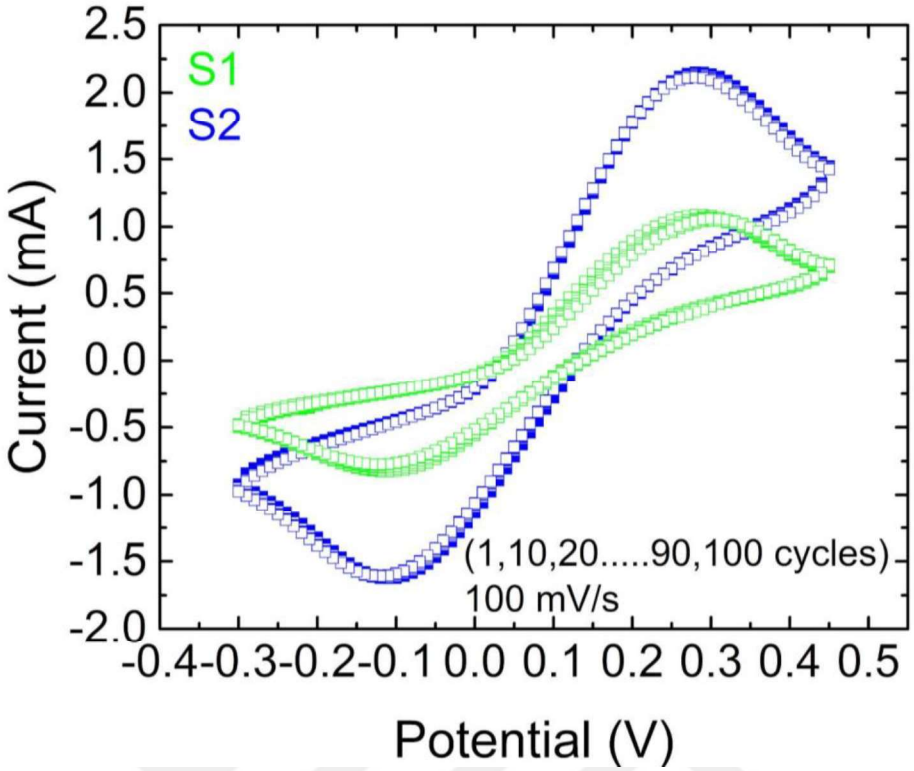

Figure 5.11 100 cyclic cycles of S1 and S2 films

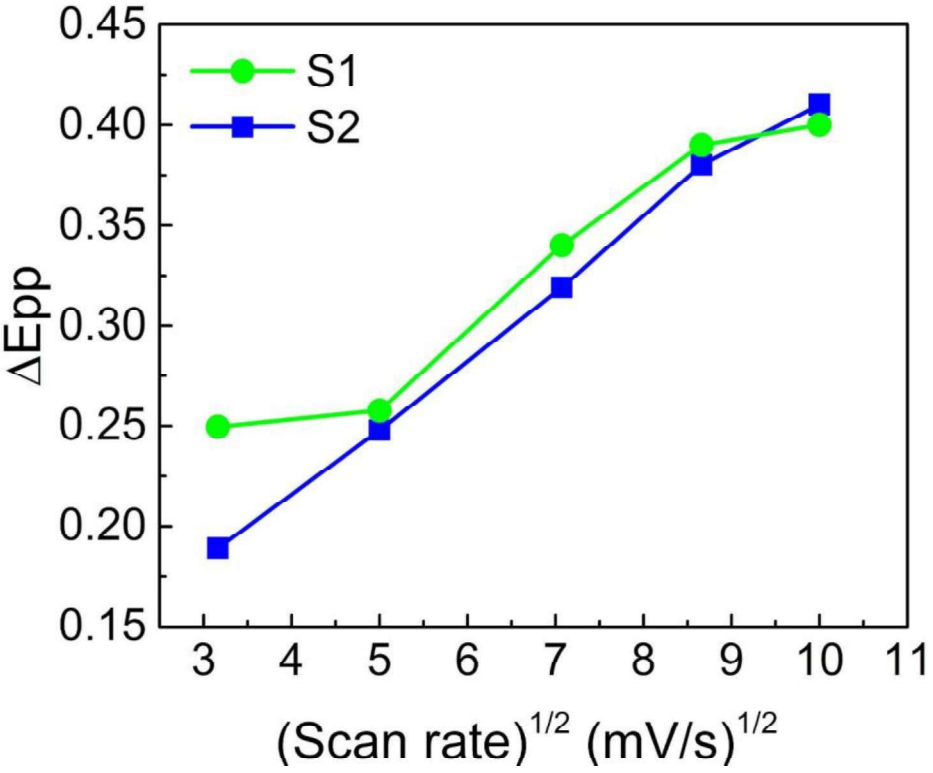

Figure 5.12 Peak to peak current values vs root of scan rates for S1 and S2 films.

Figure 5.12 presents a graph examining the relationship between the square root of scan rate and E_{pp}. E_{pp} measured 0.34 and 0.31 mV for S1 and S2 films. At the same time, S2 with a small ΔE_{pp} inversely proportional to the electron transfer rate can achieve higher electron transfer [85]. Having a small ΔE_{pp} and high electron transfer are desirable features in terms of device performance. In conclusion, the film with a higher cathodic current value and a lower ΔE_{pp} value exhibits high catalytic activity [120]. For the S2 film, both cases are provided.

5.1.7 Photovoltaic Results of Pt CEs

Figure 5.13 depicts the electrical performance of DSSCs using CBD and spin coating Pt films. The measurements were taken both in the dark and in the AM 1.5 1 sun. The dark I-V plots were very close to each other, and the V_{oc} value was slightly higher than when measured under the light as similar to [82, 121, 122].

The device performance achieved with the S2 CE was superior to that with the S1. The measured efficiency values were recorded as 4.31% and 5.06% for the device with S1 CE and devices with S2 CE, respectively. The performance increase between the two η was determined as 17.4%.

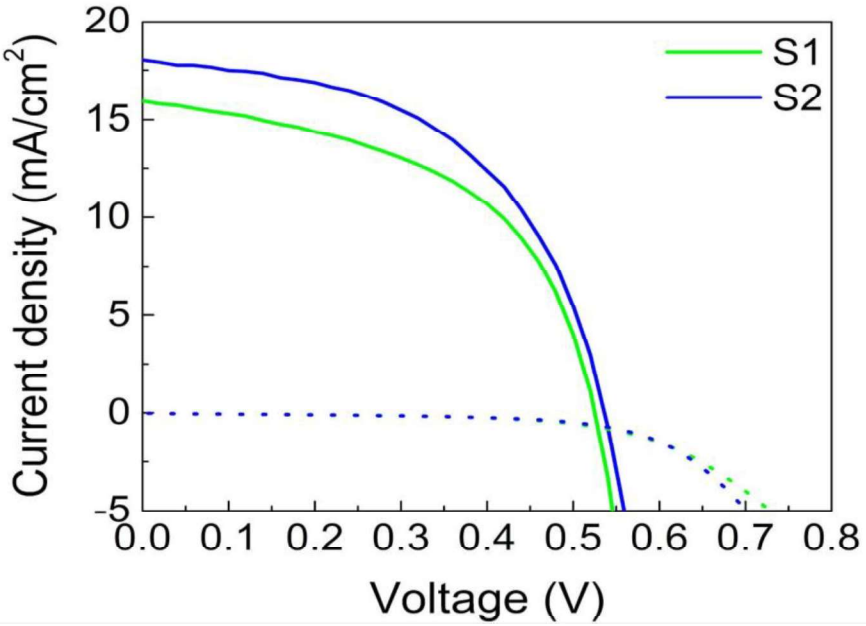

Figure 5.13 The light (solid lines) and dark (dotted lines) I-V plots of S1 and S2 films.

Table 5.2 I-V characteristics of S1 and S2 films (standard deviation is calculated with the five batches of the measurements)

Devices	J_{sc} (mA/cm^2)	V_{oc} (V)	FF	η (%)
S1	15.93 ± 0.01	0.52 ± 0.02	0.52 ± 0.01	4.31 ± 0.16
S2	18.03 ± 0.40	0.54 ± 0.02	0.52 ± 0.02	5.06 ± 0.07

According to the results shown in Table 5.2, the adhesion of the film to FTO is similar on both devices with similar FF value [115]. The superior performance of DSSC obtained by S2 CE is due to the high catalytic activity of Pt films obtained by different methods, which is demonstrated by Tafel and CV measurements. It also resulted in significant improvement for J_{sc}. It may even be associated with a synergistic effect consisting of higher reflectivity, favorable charge transport resistance and better catalytic activity of S2 CE. In the end, these findings offer convincing proof that DSSC productivity with opaque Pt produced with CBD opens up the possibility of DSSC productivity being further increased.

5.1.8 Tape Adhesion Test Results of Pt CEs

Figure 5.14 shows the sheet resistance stability of the deposited films. A 3M removable tape was stuck on the films and after peeling off to check the adhesion of the film, the sheet resistances were measured. Average sheet resistance measurement values provide an indication of the electrical stability of the film.

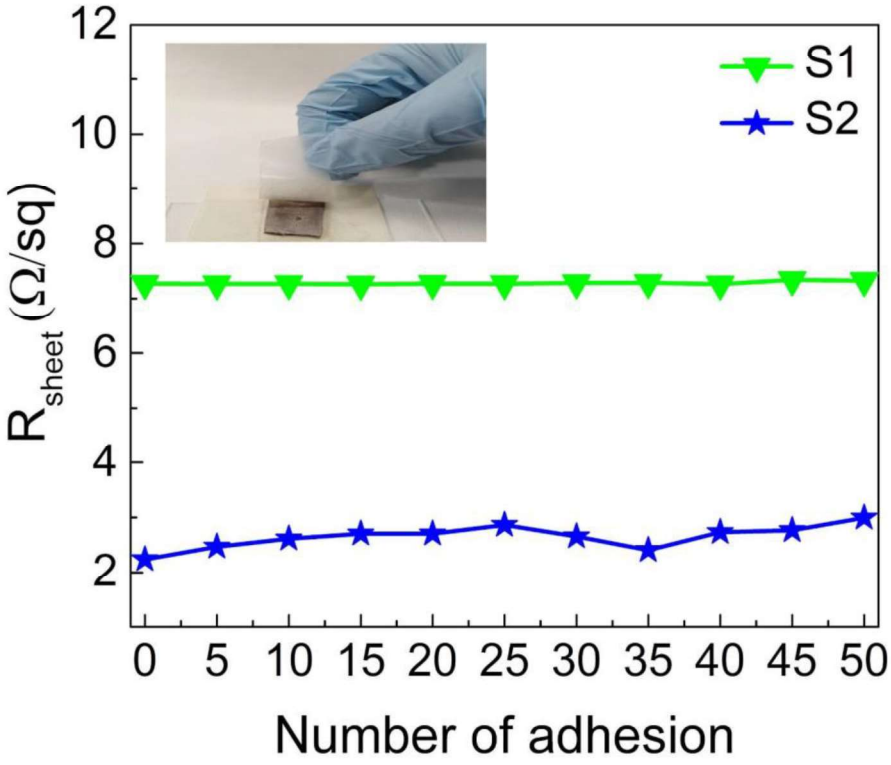

Figure 5.14 The sheet resistance plot (lines are for the eye guide) of S1 and S2 films. Inset shows a photo for tape removal from the film surface.

5.2 Characteristics of TiO_2 Seed Layers Deposition

In this part, the studies on the prerequisite seed layer for hydrothermal deposition were presented. The optical, morphological, and electrical properties of chemically produced TiO_2 films were investigated.

5.2.1 Uv-vis Results of TiO_2 Seed Layers

Figure 5.15 shows the optical transmittance properties of the films obtained with different molarity and time durations in the range from 200 nm to 1100 nm. Average transmittance values for the visible region (400-800 nm) were calculated in Table 5.4 as 0.67, 0.62, 0.65, 0.64, 0.62 for FTO s104, s154, s106, and s156, respectively.

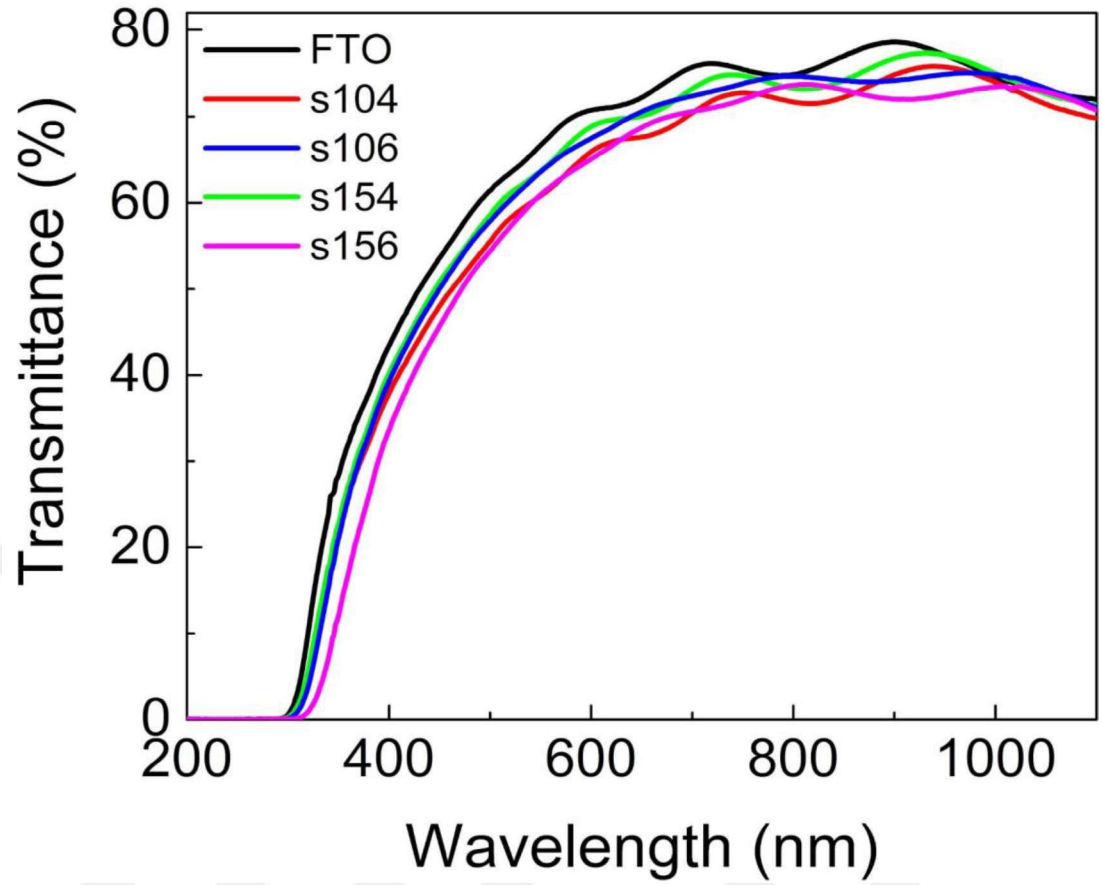

Figure 5.15 Transmittance spectra of the films loaded 0.10 M, 0.15 M of aqueous $TiCl_4$ solution for 40 and 60 min dipping time.

Increasing immersion time does not make a significant difference for the low molarity (0.10 M) case. In the case of higher molarity (0.15 M) the shorter immersion time supplies lower transparency compared to the longer one. With the effect of time, the comparison between s104 and s106 shows a drop in the transmittance might be related to the incomplete growth of the film. Smaller grains might be induced a lower transparency of the film. Considering the films of s106 and s156, the film transmittance decreased as expected with the increasing immersion time. The higher solution molarity induces a lower optical transmittance. It is thought that the surface properties of the film have an important role in the optical properties, rather than the increase in thickness of the film. The high optical transmittance for s154 can be explained by the low surface roughness.

Figure 5.16 shows the optical absorbance of the films obtained with different molarity and bath durations. E_g can be calculated via Tauc plot given inset of the Figure 5.16. The calculated E_g values are 3.14 eV, 3.14 eV, 3.07 eV, and 2.95 eV for the films of s104, s154, s106, and s156. The E_g decreases from 3.14 to 2.95 eV with increasing in immersion time of the films. When the solution molarity change is examined, the light absorption of the film increases with increasing molarity and the value of E_g decreases [123].

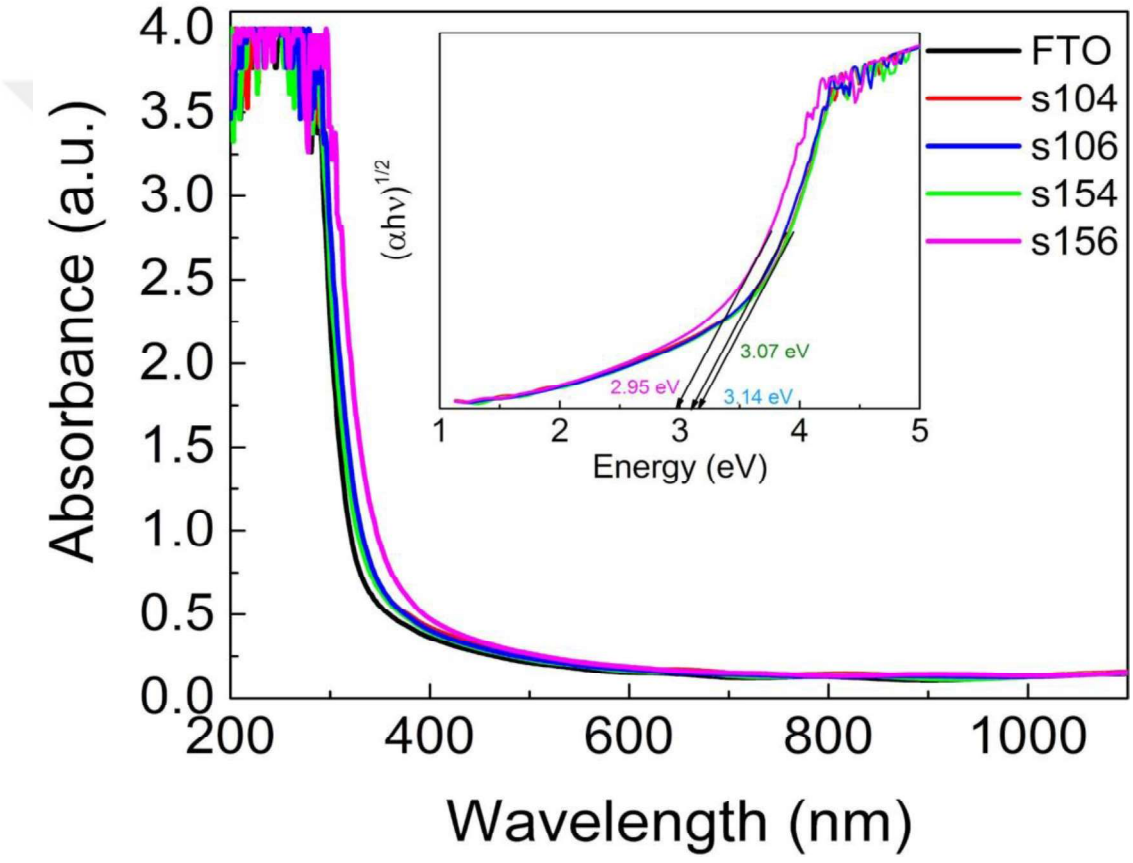

Figure 5.16 Absorbance spectra of the films loaded 0.1M, 0.15M of aqueous $TiCl_4$ solution for 40 and 60 min dipping time.

5.2.2 Sheet Resistance Measurement Results of TiO_2 Seed Layers

The Table 5.3 presents the sheet resistance measurement results of the TiO_2 films.

Table 5.3 Sheet resistance values of TiO_2 seed layer coated FTO films.

Seed layer	Avg. R_{sh} $\Omega\,cm^{-1}$	Delta R_{sh} $\Omega\,cm^{-1}$
s104	10.22	17.25
s106	11.45	31.30
s154	9.65	10.72
s156	10.32	18.17

5.2.3 AFM Results of TiO_2 Seed Layers

The 3D topographical images captured by AFM are displayed in Figure 5.17. Estimated surface roughness values of the TiO_2 are 41.06, 32.76, 39.77 and 63.56 nm for the films denoted as s104, s154, s106, and s156, respectively. A high surface roughness indicates that the film has a large height difference. As the time duration increases, for example, for the s104-s106 and the s154-s156 pairs, it is expected that the surface roughness value would decrease with the more effective filling of the FTO valleys. Films generally become smoother as molarity and time duration for CBD increase except for s156. In the case of s156, the value of the surface roughness is increased. Seen by SEM images, the porosity of the s156 is also quite different from others. The increased surface roughness of s156 might be resulted in an extra porous structure [124]. This can be explained by a high agglomeration of the particles with increasing solution molarity and immersion time. The smallest value of the surface roughness of the s154 film explains the high value of optical transmittance with lower conflict between light and matter.

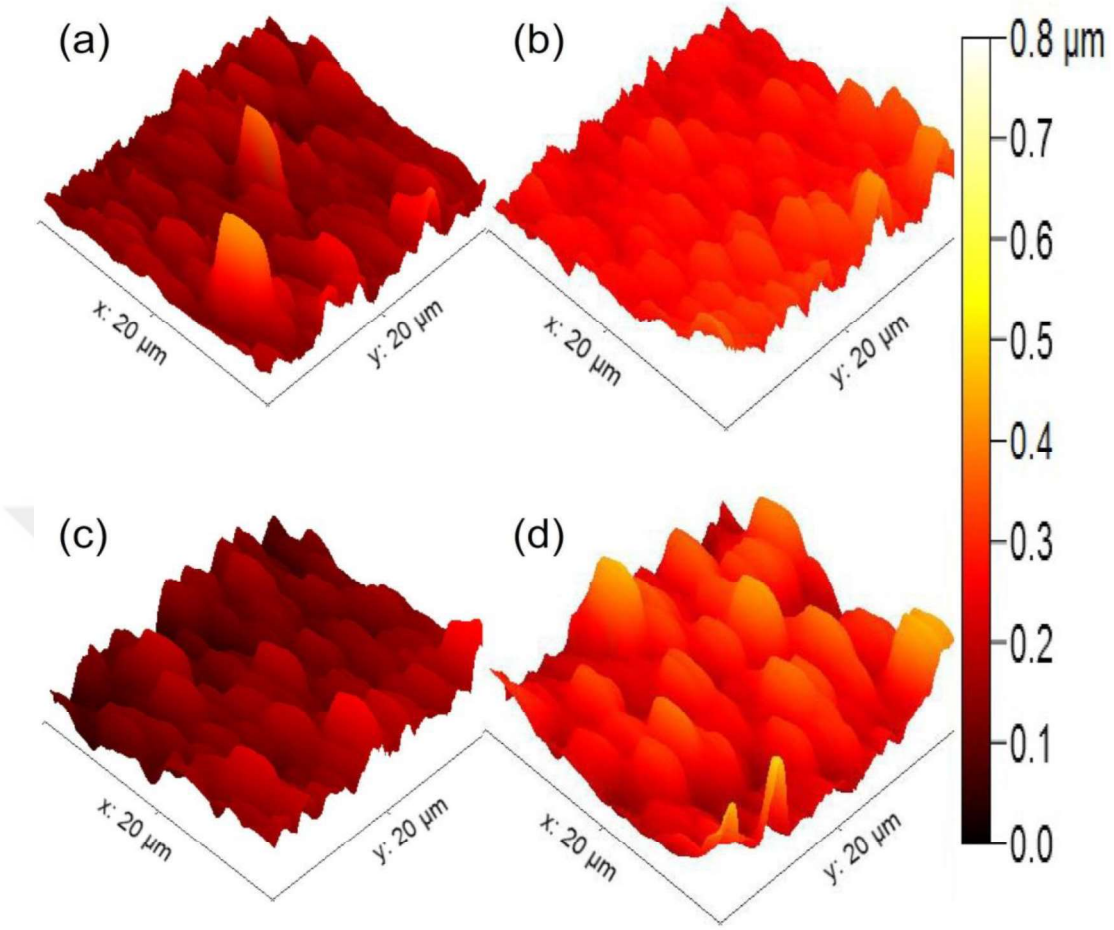

Figure 5.17 AFM images of the films 0.1M, 0.15M of aqueous $TiCl_4$ solution loaded for 40 and 60 min dipping time.

5.2.4 SEM Results of TiO_2 Seed Layers

Figure 5.18 shows the top-view SEM pictures of the TiO_2 films. The homogeneity of the film coating is expected to increase with increasing molarity and time duration. Figure 5.18a and Figure 5.18c have slightly blurred compared to bare FTO. However, with the increase in molarity for Figure 5.18b and Figure 5.18d, soft-edged structures became evident, where the film coverage was more efficiently, and the sharp corners of the particles were relatively diminished.

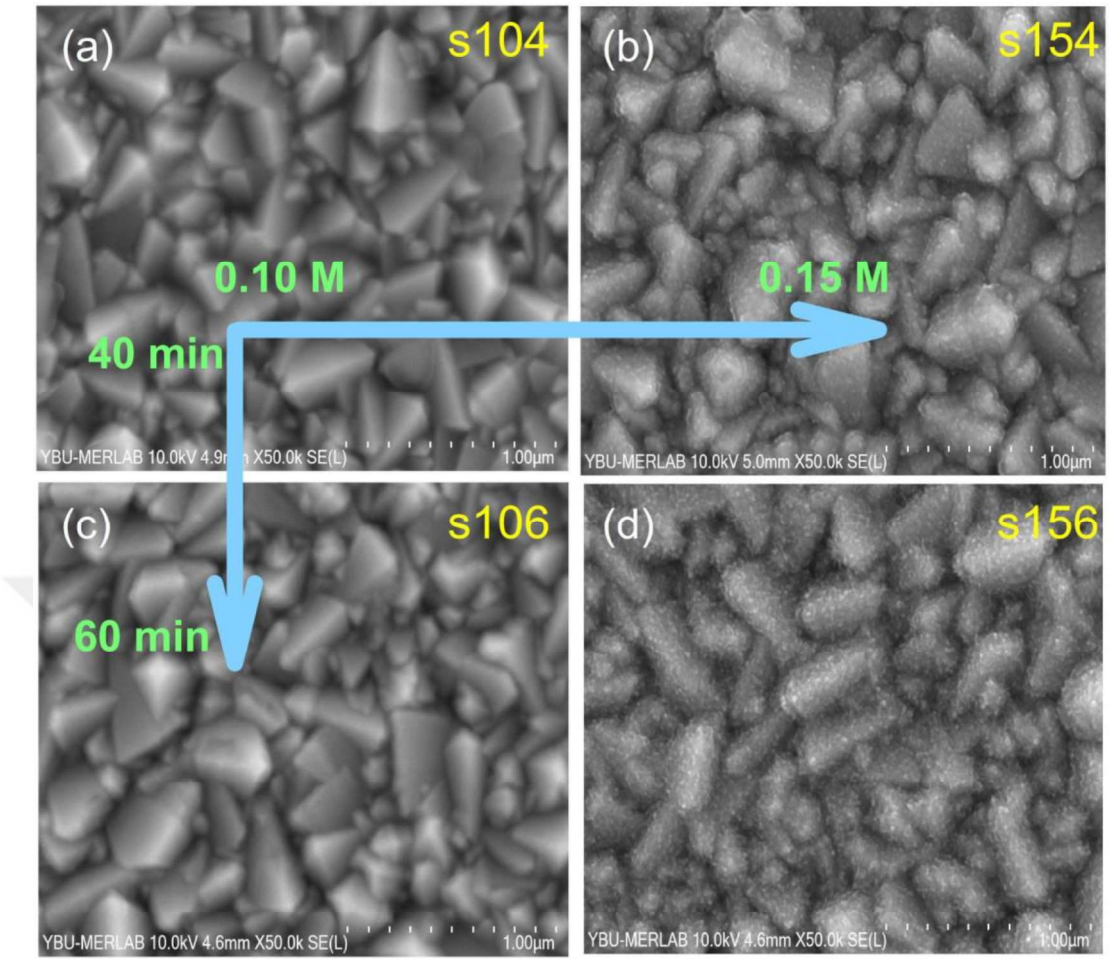

Figure 5.18 SEM images of the films loaded 0.1M, 0.15M of aqueous $TiCl_4$ solution for 40 and 60 min dipping time.

5.2.5 Tafel Polarization Results of TiO_2 Seed Layers

Tafel analysis was accomplished to further evaluation of the film coverage and investigation of the blockage effect. Figure 5.19 shows the Tafel plots of the films that were recorded in a simple device configuration with Pt CE and electrolyte. The homogeneous and fully coating of the film results in a lower current value that can be obtained at the same voltage value [125]. Deposited films with lower molarity (0.10

M) have a lower surface coverage compared to its counterparts. In addition, a significant increase in film homogeneity and blocking effect was observed with

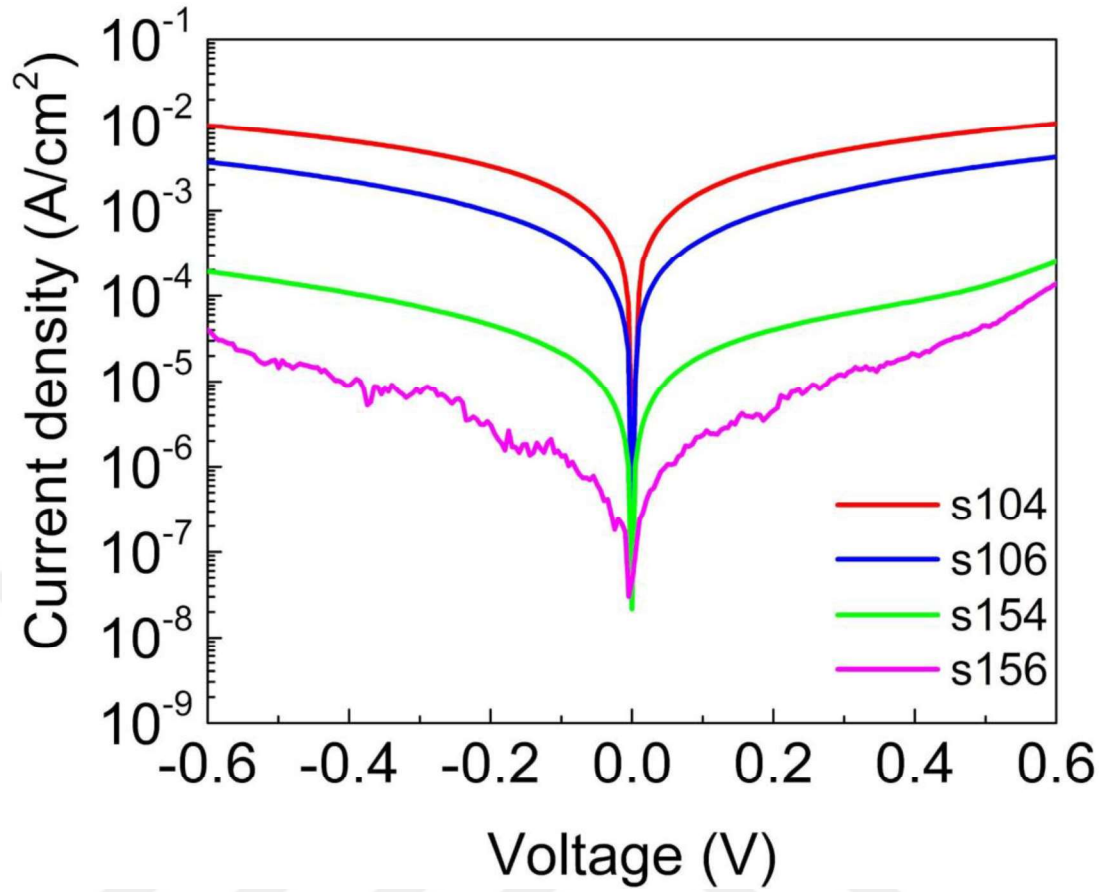

Figure 5.19 Tafel plots of the films loaded 0.1M, 0.15M of aqueous $TiCl_4$ solution for 40 and 60 min dipping time.

increasing coating time. If only the thickness factor were effective, the transparency would have to be lower for s154 in this case.

5.2.6 Figure of Merit Estimation of TiO_2 Seed Layers

Figure 5.20 shows the calculated FOM values of the 100 mM and 150 mM of different duration bath deposited TiO_2 films. Table 5.4 also summarizes numerically the optical, electrical and surface properties of the films. The final analysis of the electrical and optical properties of the films reveals that the film (s154) having higher solution molarity (0.15 M) and shorter deposition time exhibits a higher value of FOM among others. The lower surface roughness of s154 film dictates the high transmittance of the film.

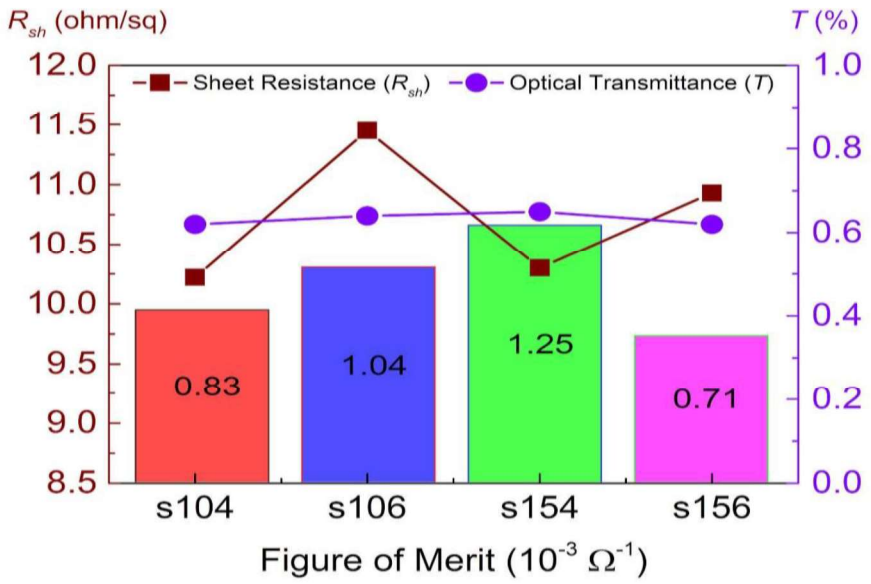

Figure 5.20 FOM of the films loaded 0.1M, 0.15M of aqueous $TiCl_4$ solution for 40 and 60 min dipping time.

FOM of bare FTO is 2.1 x 10^{-3} and higher than TiO_2 coated films. Considering the experimental conditions, it is not surprising that the optical and electrical properties of the TiO_2 film deteriorate due to the insulating nature with increasing molarity and time [126, 127]. Even though there are no significant differences in optical properties, at a critical point, the highest optical transmittance combined with the lowest sheet resistance value yields the highest FOM value. A decrease in the number of grain boundaries reduces surface roughness and sheet resistance while increasing transmittance.

Table 5.4 FOM characteristics of TiO_2 seed layers

Seed layer	T (%)	E_g (eV)	R_{sh} (Ω cm)	FOM	RMS (nm)
S104	0.62	3.14	10.22	0.83	41.06
S154	0.65	3.14	10.3	1.20	32.76
S106	0.64	3.07	11.45	1.00	39.77
S156	0.62	2.95	10.93	0.71	63.56

Overall, with short immersion time and high solution molarity produced s154 film exhibited high transmittance, low surface roughness, and low sheet resistance. These properties make it a suitable candidate as a seed layer for the hydrothermal process.

5.3 Characteristics of the Hybrid Devices

5.3.1 Uv-vis Results of Hybrid Devices

Figure 5.21 shows the absorbance graphs of the TiO_2 films after dye loading for the TiO_2 NP, TiO_2 NR, Hybrid, and Hybrid without BL, respectively. The TiO_2 NR film had the lowest dye absorption due to its surface area. The absorbance graph of the hybrid structure, which was a combination of two layers, was greater. Because of the BL treatment, the absorbance of the Hybrid PA increased in the visible area [128]. The reduced absorbance spectra of Hybrid without BL compared to TiO_2 NP can be attributable to reflection losses caused by nanorods [69]. Although the optical perspective regarded these reflections as a loss, the final structure benefited immensely from the electrical bridging points and precise band alignment tolerance. Despite having comparable anatase-rutile weight ratios, the anatase crystal size in TiO_2 NP (20.16 nm) was bigger than in hybrid without BL (18.39 nm), which supported its higher absorbance graph. [129]. Because the rutile phase was more prominent in the photoanode without BL (53.09%), it was expected to have a lower absorbance than TiO_2 NR (99.98%).

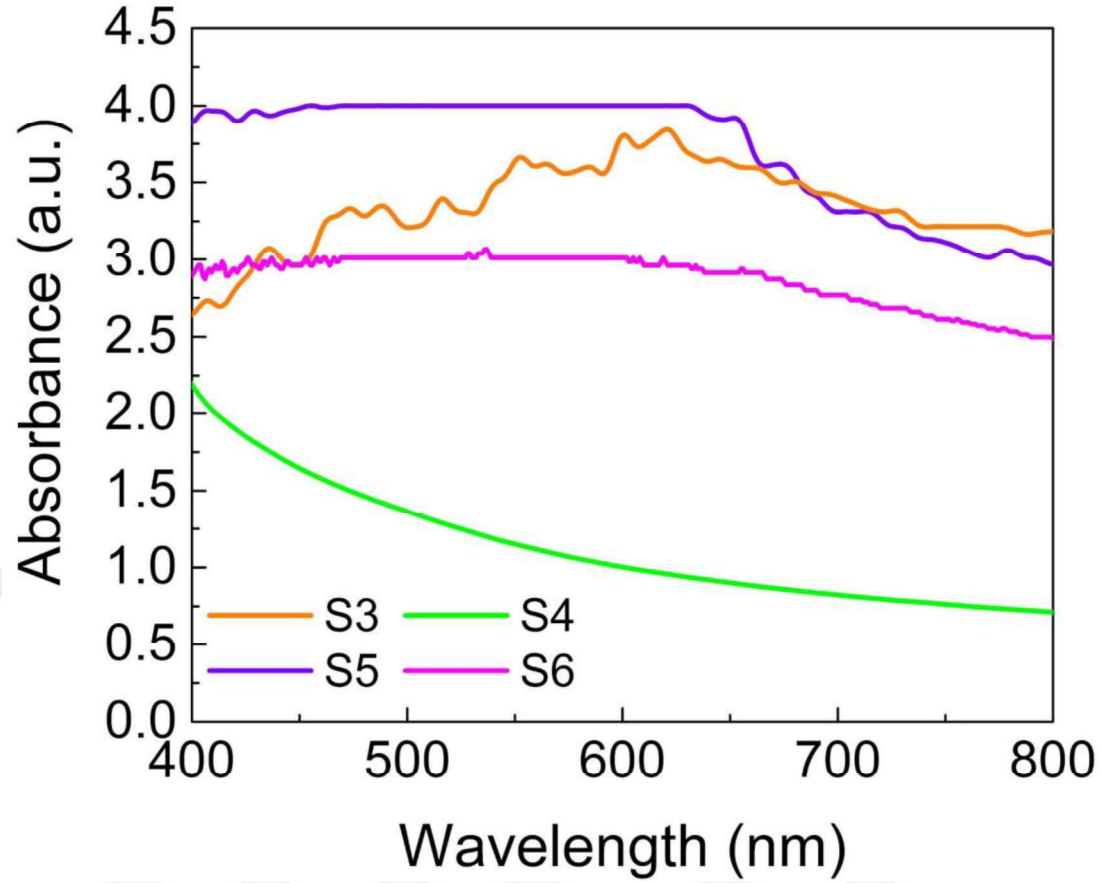

Figure 5.21 UV-vis absorbance spectra of S3, S4, S5 and S6 films.

5.3.2 XRD Results of Hybrid Devices

Figure 5.22 shows the XRD pattern of the PAs of TiO_2 NP, TiO_2 NR Hybrid and Hybrid without BL, respectively. The diffraction pattern of hydrothermally grown TiO_2 NR film has dominant rutile (JCPDS No: 01-076-1939) (101) peak at 35.99˚. There is no clear anatase peak in the linear scale. The remaining peaks are from the FTO substrate (JCPDS No: 00-041-1445). Because of the low-intensity peaks, commenting on the linear plot of the XRD plot may be difficult. As a result, Figure 5.23 provides the logarithmic plot of XRD. It enables a more intimate view of each peak.

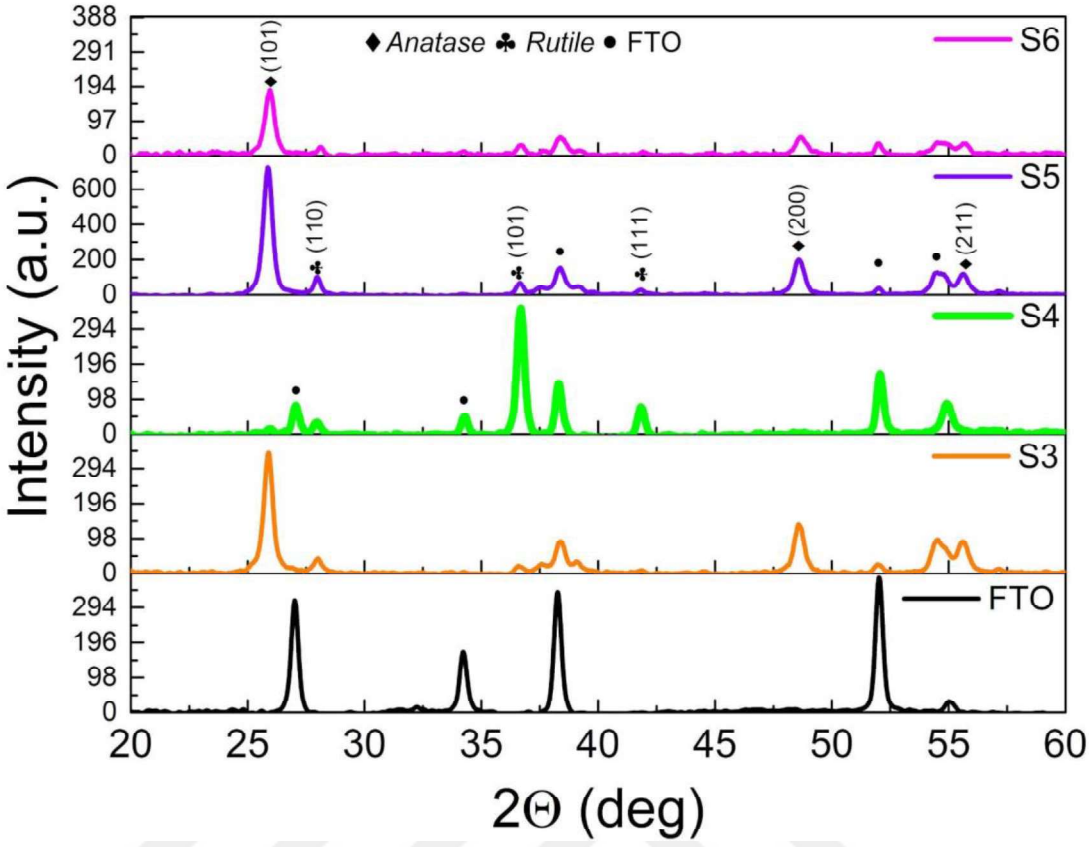

Figure 5.22 Linear XRD pattern for S3, S4, S5 and S6 films.

The weight fraction of anatase compared to rutile was calculated with Debye-Scherrer formula as 46.71%, 0.02%, 56.12%, 46.91% for the TiO_2 NP, TiO_2 NR, Hybrid, and Hybrid without BL, respectively. The TiO_2 NP layer contains anatase and rutile phases. As predicted by the literature, the TiO_2 NR layer is primarily composed of the rutile phase [130].While the weight fraction of the rutile drops (from 53.09 to 43.88%), the addition of BL increases the intensity of the rutile's crystalline size (from 23.62 nm to 41.61 nm).

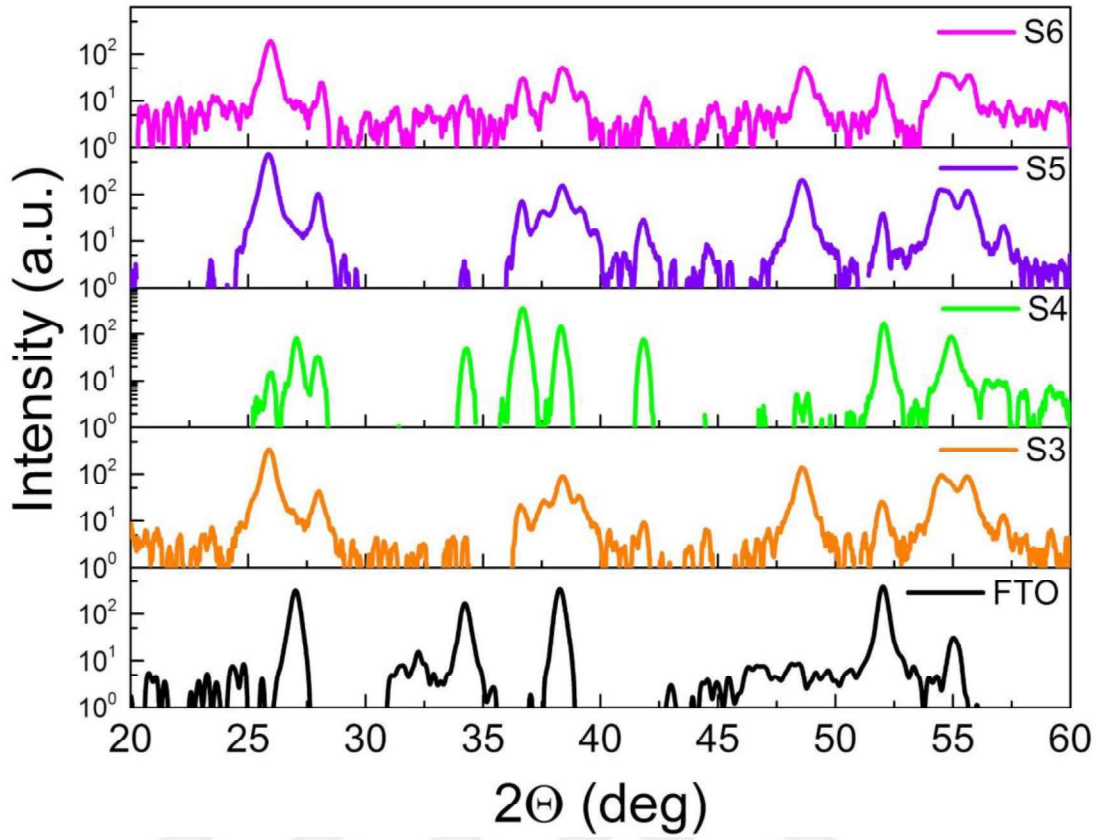

Figure 5.23 Logarithmic XRD pattern for S3, S4, S5 and S6.

Table 5.5 XRD characteristics of hybrid photoanodes

Photoanodes	Crystalline Sizes (nm)		Weight Fractions (%)	
	Anatase (101)	Rutile (101)	Anatase (101)	Rutile (101)
S3	20.16	23.66	46.71	53.29
S4	-	29.44	0.02	99.98
S5	18.80	41.61	56.12	43.88
S6	18.39	23.62	46.91	53.09

This indicates that the BL caused the growth of larger rutile particles in the connection links between NRs and NPs. TiO_2 forms an amorphous pattern when *TiCl*4 based-BL is applied at ambient temperature [131]. According to their weight fractions, this causes anatase to appear more frequently in our case. Additionally, the accumulation of particles can cause rutile's crystallite size to rise [132].

5.3.3 SEM Results of Hybrid Devices

Figure 5.24, Figure 5.25, Figure 5.26 show the top images of the TiO_2 NP (S3), TiO_2 NR (S4), Hybrid (S5) photoanodes, while Figure 5.28, Figure 5.27 show the cross-sectional images of Hybrid without BL (S6), and Hybrid (S5) photoanodes. Because both TiO_2 NP and hybrid films have a top mesoporous layer, their top perspectives are comparable. Figure 5.25 clearly presents the nanorod growth of the TiO_2. The thickness of the Hybrid without BL and Hybrid photoanodes are estimated as 5.37 and 5.84 μm, respectively.

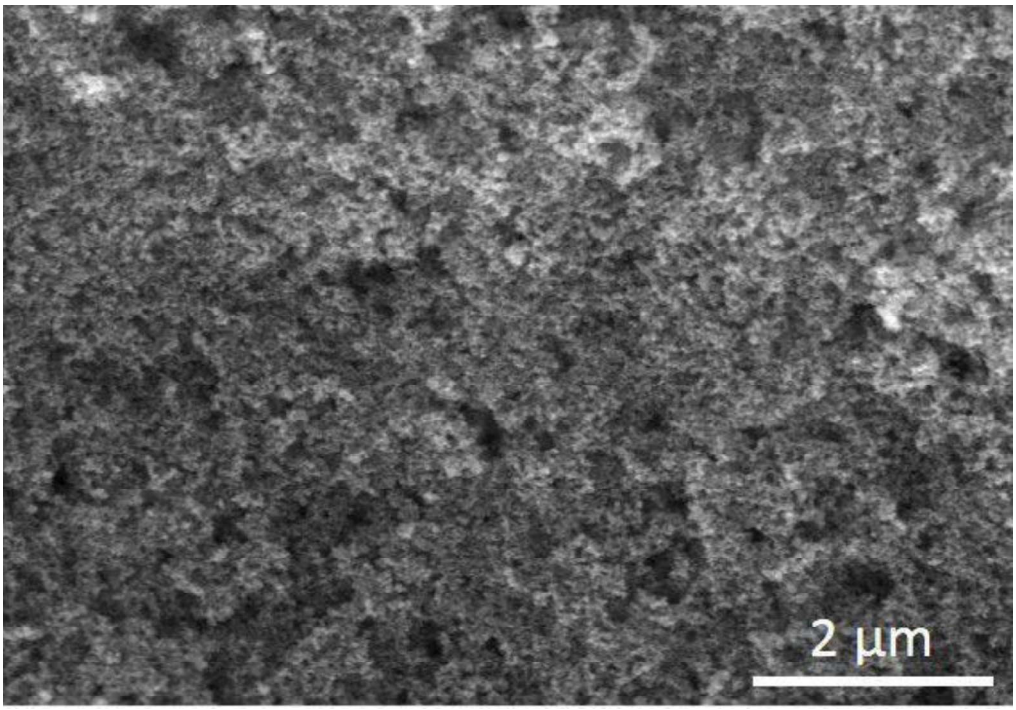

Figure 5.24 Top-view SEM image of S3 photoanode.

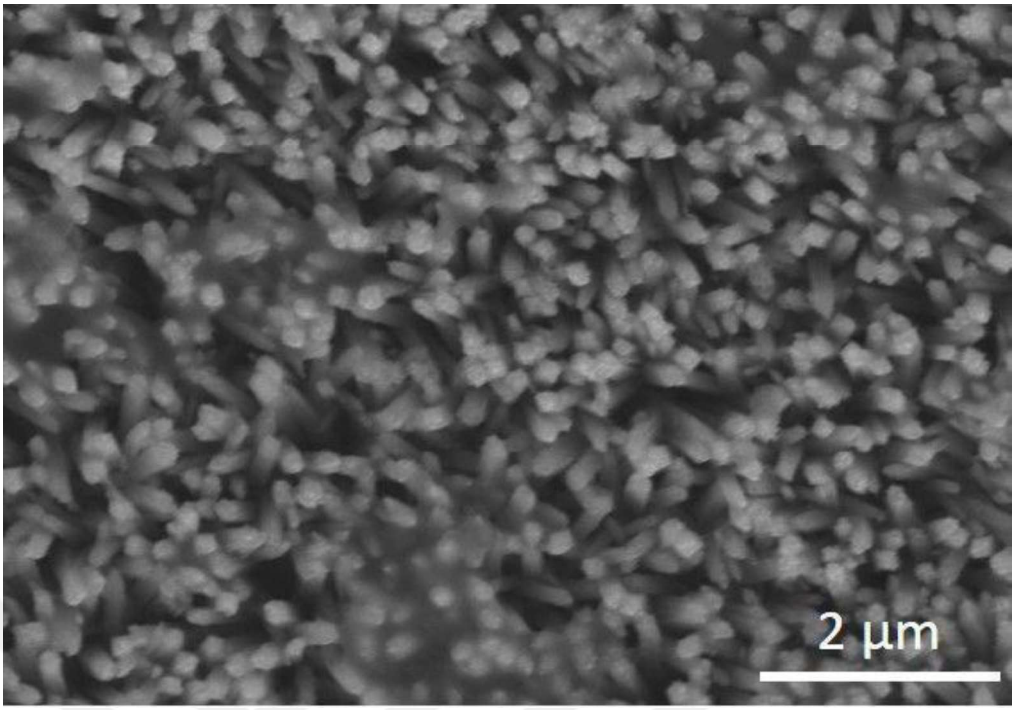

Figure 5.25 Top-view SEM image of S4 photoanode.

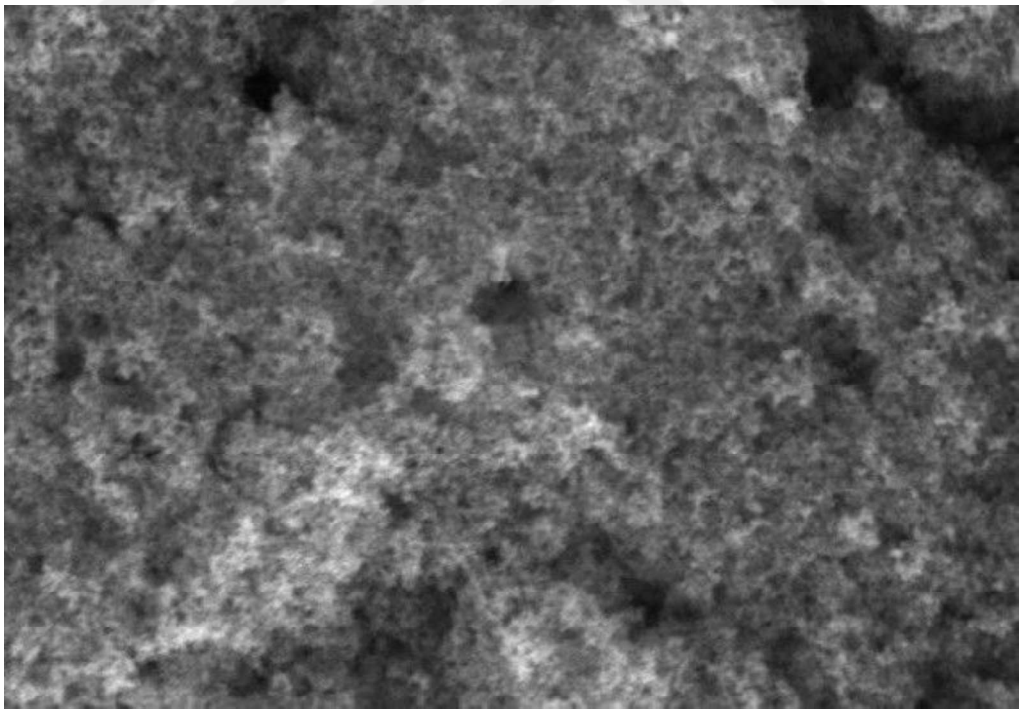

Figure 5.26 Top-view SEM image of S5 photoanode.

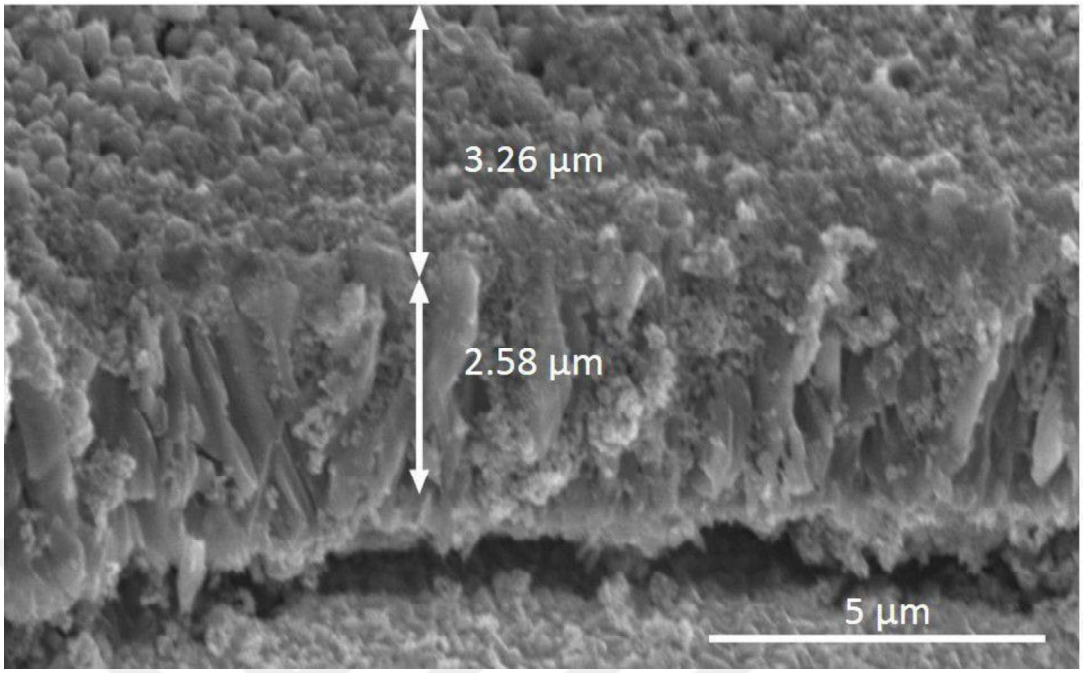

Figure 5.27 Cross-sectional SEM image of S5 photoanode.

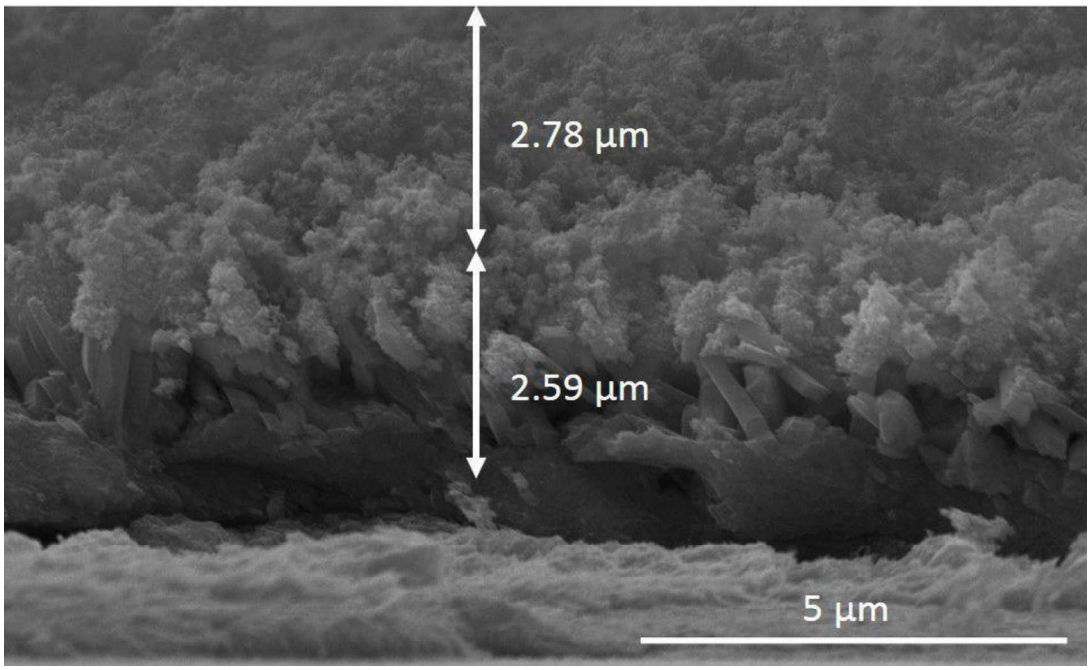

Figure 5.28 Cross-sectional SEM image of S6 photoanode.

5.3.4 Photovoltaic Results of Hybrid Devices

Figure 5.29 and Table 5.6 depict the manufactured devices' photovoltaic performance while illuminated by AM 1.5 artificial light (one sun). The experimental findings show that the S5 has the greatest J_{sc} value. The titanium dioxide NR layer, S6, which was hydrothermally produced on the device, has poor optical characteristics because it limited internal space and dye anchoring points. This situation is reflected in the value of J_{sc} [68]. The lower value of the R_{sh} in the S5 leads to lower value of J_{sc} and V_{oc} [88]. The benefit of NRs in the hybrid S5 structure and the lengthened optical path, however, may cause enhanced reflections to lead to a situation in which photo-generated carriers are stronger than potential recombinations. Despite the larger likelihood of recombinations in the present situation, the harvesting efficiency and value of J_{sc} both dramatically rise. The mismatch of the energy band levels in relation to the phases of TiO_2 is most likely the cause of the J_{sc} value of S6 suffering [133].

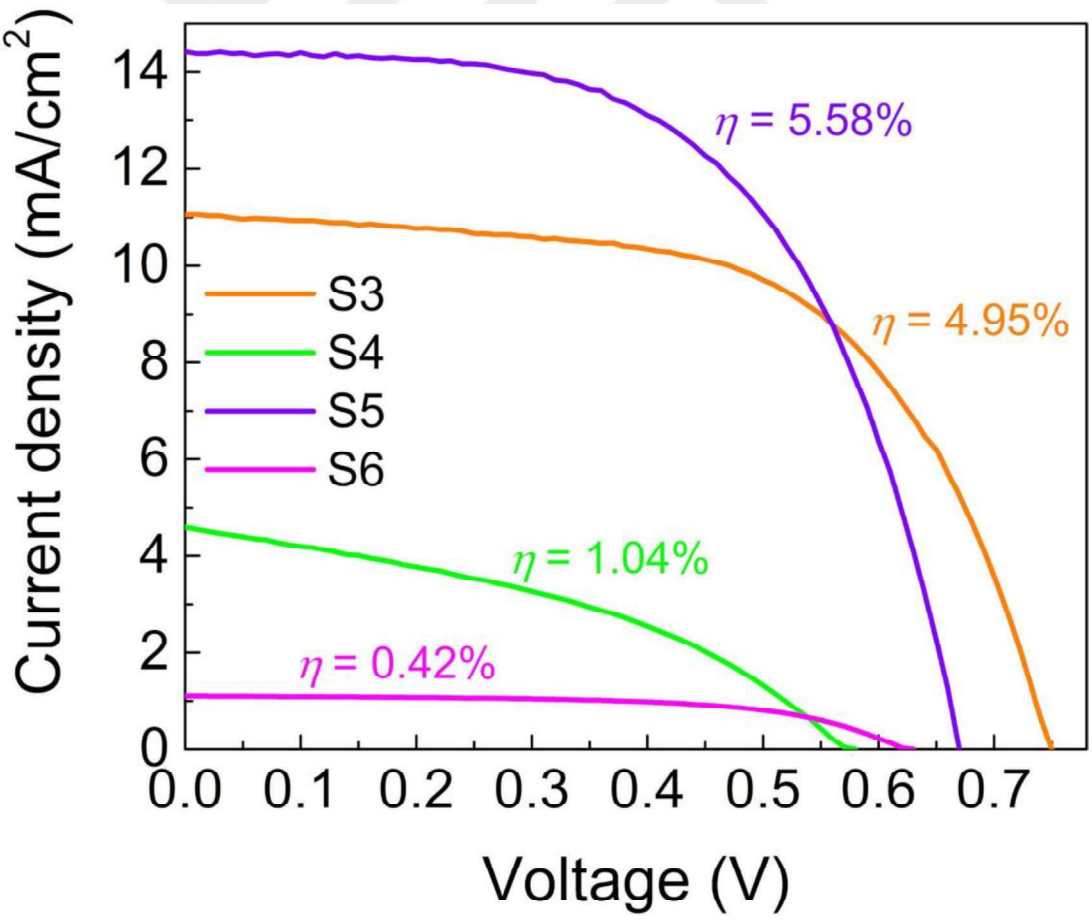

Figure 5.29 Light I-V plots for S3, S4, S5 and S6.

Electrons are prevented to able to reach to the FTO, possibly due to recombination. At the same time, the lower value of R_s supports the high value of J_{sc}. The value of V_{oc} is 0.75, 0.57, and 0. 72, and 0.62 for the S3, S4, S5 and S6, respectively. Leakage current may increase and V_{oc} may decrease for rutile (in TiO_2 NR) due to its lower inherent resistance value compared to anatase [134]. This trend supports the tendency of R_{sh}. Final device performances are obtained as 4.95%, 1.04%, 5.58%, and 0.42% for the S3, S4, S5 and S6, respectively. In S5, the hybrid design and additional BL inter-connectivity, the device efficiency was improved at least around 13% from 4.95% to 5.58%.

Due to the effectiveness of the BL placed into the device configurations, it is possible to compare the devices assembled with and without BL to determine their function. As seen from Table 5.6, especially the R_s becomes higher in the absence of BL in the device configuration, which results in a remarkable degradation in J_{sc}. As Mi and

Table 5.6 I-V characteristics of hybrid devices (standard deviation is calculated with the five batches of the measurements)

Devices	J_{sc} (mA/cm^2)	V_{oc} (V)	FF	η (%)	R_s (Ω cm^2)	R_{sh} (Ω cm^2)
S3	11.00 ± 0.08	0.75 ± 0.01	0.60 ± 0.02	4.95 ± 0.15	15.8	603.7
S4	4.59 ± 0.01	0.57 ± 0.01	0.40 ± 0.00	1.04 ± 0.01	80.3	258.0
S5	14.42 ± 0.10	0.67 ± 0.02	0.58 ± 0.01	5.58± 0.11	20.2	425.8
S6	1.11 ± 0.25	0.62 ± 0.01	0.61 ± 0.04	0.42 ± 0.08	265.3	5850.1

Weng reported, electron transport between the anatase and rutile phases can occur in different directions depending on the CB levels [133]. According to findings of this study, electron migration from rutile to anatase via nanostructures is possible [133]. The fact that the hybrid without BL has a conduction problem supports the idea that the photo-generated electron flow is from rutile to anatase and cannot reach the FTO through the anatase [135]. Because the contact points are predominantly rutile, the transfer of photo-generated electrons to anatase is a form of return and quenching due to the higher recombination possibility [136, 137]. The presence of BL in the device architecture allows the anatase TiO_2 particles to partially fill the voids (interlayer and gap between the aligned rods). This allows for close contact locations with FTO and easy electron transport. A device constructed with the S5 achieves a large performance boost (5.58%) over its analog (0.42%).

5.3.5 EIS Results of Hybrid Devices

EIS measurements are used to assess how the presence of the BL in the device architecture impacts the interfacial resistances within the devices. Figure 5.30 and Figure 5.31 are the corresponds to the Bode and Nyquist plots estimated by EIS measurement applied at V_{oc}.

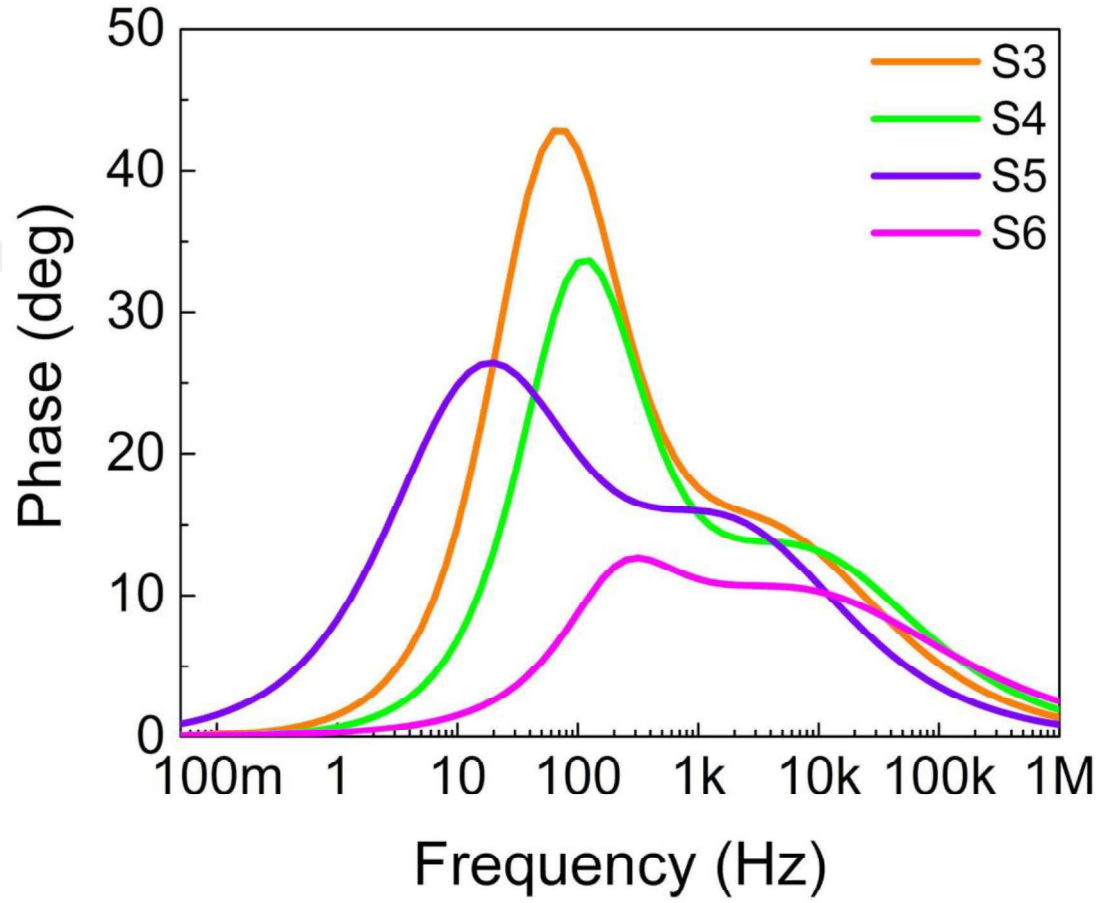

Figure 5.30 Bode plot for S3, S4, S5 and S6 hybrid DSSCs.

Because similar CE and FTO substrates are used to build the devices, the values of R_{s-eis} and R_{ct} vary slightly from device to device. However, the difference of R_{rec} is significant. It reaches the lowest value (14.54 Ω cm^2) for the device assembled without BL (S6), indicating that the largest recombination loss exists for this device [64]. Recombinations are unavoidable since the S6 has an incompatible energy band structure and the lowest R_{rec} value. The high R_{rec} resistance is an essential marker of the prevention of electron transport loss. It can be traced to a decline in the number of

electrons recombined and improved electron transport. The device with TiO_2 NP has a larger Rrec than the S5, maybe hybrid structure has higher defects. The overall results show how important BL is in the hybrid device design.

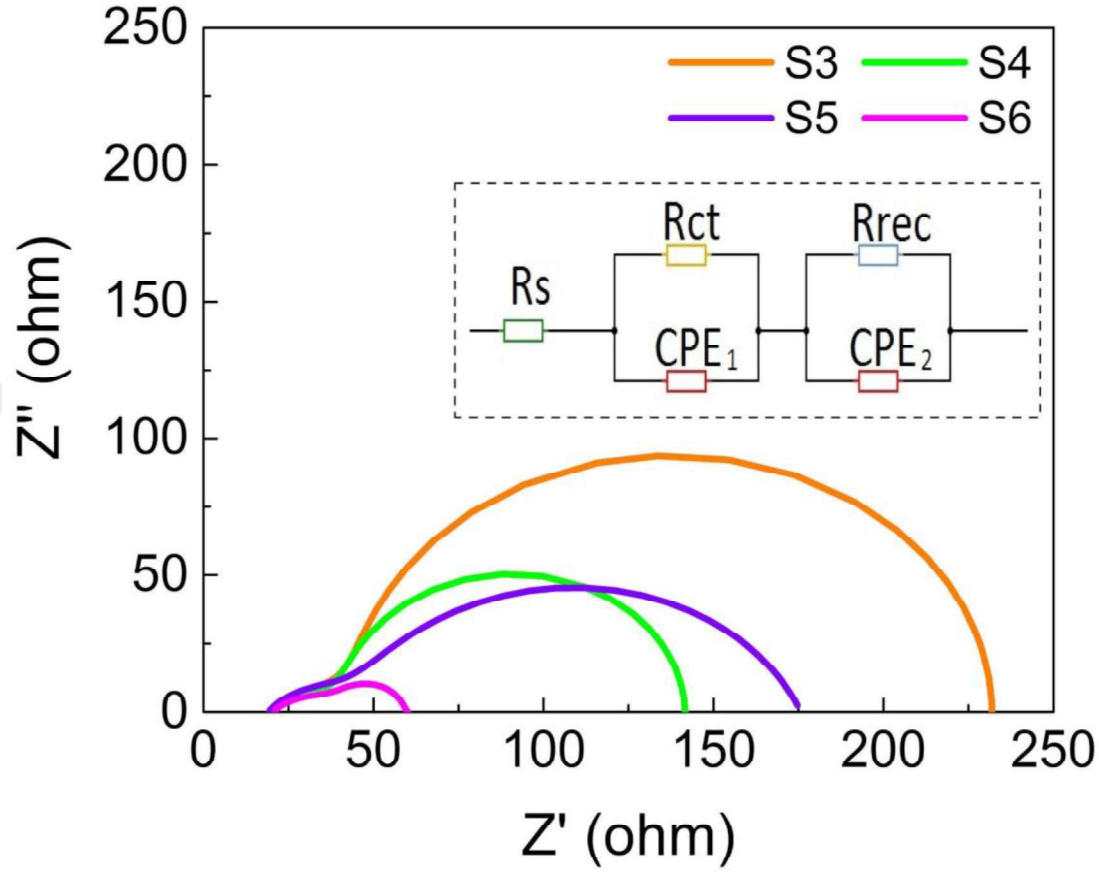

Figure 5.31 Nyquist plot for S3, S4, S5 and S6 hybrid DSSCs. Inset shows the equivalent circuit for the device.

CHAPTER 6

CONCLUSION AND FUTURE SUGGESTIONS

6.1 Conclusion

The goal of this thesis study was to develop well-designed electrodes (CE and photoanode) to further boost the efficiency of DSSCs. The major conclusions are as follows:

The first stage of the thesis comprises two different CE comparisons. While it has strong catalytic activity and optical opacity, which is opaque when compared to CE films with similar optical, electrical, morphological, and catalytic capabilities, its electrical instability is its weak point. The film, which is coated with a chemical process, stands out with its low transmittance and high reflectivity. The particle size measured in SEM is also greater than the other. It also has stronger catalytic activity than its counterpart, as measured by CV, Tafel, and EIS. However, because the electrical stability issue would have an impact on performance, the study continued with the transparent S1 film.

The photoanode layers were developed in a hybrid form later on. Hybrid design contains nanorod and nanoparticle structures. The hydrothermal approach has proven to be both feasible and effective in this regard. The examination and optimization of the core layer has been prioritized as a prerequisite for the hydrothermal layer. According to optical, electrical, and morphological analyses of TiO_2 films formed by chemical bath method, the film obtained at 150 mM and 40 minutes time conditions exhibits good transmittance, low sheet resistance, and low surface roughness. Hydrothermal growth was accomplished upon the seed layer in the subsequent study.

In the last part of the thesis, a hybrid device structure was obtained by combining nanostructures with different morphologies (nanoparticle & nanorod). While it was observed that the 1-dimensional TiO_2 NR layer alone was not sufficient, its combination

with nanoparticles provided a significant increase in device performance.

To construct a hybrid device structure, the TiO_2 NP was combined with a hydrothermally grown TiO_2 NR layer. Even the TiO_2 NR layer alone was not suitable for efficient dye loading, high reflectivity of light and electrical highways of the 1D structures makes them a good candidate for combination. The hybrid structure has higher J_{sc} and efficiency than single NPs and NRs. With the combination of layers containing different phases may cause some transport problems, but the connection was achieved by filling the voids with small particles (by BL application) having an appropriate conduction band energy level. The hybrid device with the BL overwhelmingly outperformed its analogue. The hybrid device exhibited an efficiency of 5.58%, which was higher than that of the devices having only nanoparticles (4.95%) or nanorods (1.04%).

6.2 Suggestions for Future Work

This work on dye-sensitized solar cells is still explorable at both the academical and commercial levels. The following topics demand more research:

* This work includes a comparatively thin photoanode layer. In this respect, it can be combined with a different electrolyte, as it is more often preferred with Cu and Co containing electrolytes for low thickness photoanodes. This might improve the performance of the device more.

* More detailed diversification of experimental conditions can be attempted in the hydrothermal phase. For example, the usage of different acids or additives would enrich the study with different nanostructures. It is believed that the additional steps in the hydrothermal approach, such as etching, will alter the characteristics of the films and the device's performance.

* Another possible study route would be to investigate the efficacy of adding other metal oxide layers to the photoanode in order to improve upon the current levels.

* One of the study's long-term goals is to gradually adapt the photoanode and counter electrode to low temperatures and to be able to coat them on flexible surfaces in order to broaden the application areas.

REFERENCES

[1] IPCC, “Sixth assessment report,” 2022, retrieved July 17, 2022. [Online]. Available: https://www.ipcc.ch/assessment-report/ar6/

[2] Science Media Centre, “Assessment report 6, working group 3,” 2022, retrieved July 17, 2022. [Online]. Available: https://www.sciencemediacentre.org/ expert-reaction-to-assessment-report-6-working-group-3-mitigation-as-published\ -by-the-ipcc/

[3] Our World in Data, “Renewable energy,” 2020, retrieved July 14, 2022. [Online]. Available: https://ourworldindata.org/renewable-energy

[4] Business Insider, “This incredible fact should get you psyched about solar power,” 2015, retrieved July 17, 2022. [Online]. Available: https://www.businessinsider.com/this-is-the-potential-of-solar-power-2015-9?international=true&r=US&IR=T#:~:text=In%20a%20single%20hour%2C%20the,with%2018%20zeroes%20after%20it\protect\leavevmode@ifvmode\kern.1667em\relax

[5] Andualem A. and Demiss S., “Review on dye-sensitized solar cells (dsscs),” *Edelweiss Appli Sci Tech*, vol. 2, pp. 145–150, 2018.

[6] Jean J., Brown P. R., Jaffe R. L., Buonassisi T., and Bulović V., “Pathways for solar photovoltaics,” *Energy & Environmental Science*, vol. 8, no. 4, pp. 1200–1219, 2015.

[7] GlobeNewswire News Room, “Global crystalline silicon solar pv market is projected to grow at a cagr of 13.3% by 2031: Visiongain research inc,” 2021, retrieved July 27, 2022. [Online]. Available: https://www.globenewswire.com/news-release/2021/09/02/2291062/0/en/Global-Crystalline-Silicon-Solar-PV-Market-is-Projected-to-Grow-at-a-CAGR-of-13-3-By-html#:~:text=The%20global%20Crystalline%20Silicon%20Solar,the%20forecast%20period%202021%2D2031.

[8] Google Inc, “Nrel2018,” 2018, retrieved January 14, 2022. [Online]. Available: https://www.nrel.gov/pv/cell-efficiency.html./

[9] Yoshikawa K., Kawasaki H., Yoshida W., Irie T., Konishi K., Nakano K., Uto T., Adachi D., Kanematsu M., Uzu H. *et al.*, “Silicon heterojunction solar cell with interdigitated back contacts for a photoconversion efficiency over 26%,” *Nature energy*, vol. 2, no. 5, pp. 1–8, 2017.

[10] Dimroth F., Grave M., Beutel P., Fiedeler U., Karcher C., Tibbits T. N., Oliva E., Siefer G., Schachtner M., Wekkeli A. *et al.*, “Wafer bonded four-junction gainp/gaas//gainasp/gainas concentrator solar cells with 44.7% efficiency,” *Progress in Photovoltaics: Research and Applications*, vol. 22, no. 3, pp. 277–282, 2014.

[11] Kayes B. M., Nie H., Twist R., Spruytte S. G., Reinhardt F., Kizilyalli I. C., and Higashi G. S., “27.6% conversion efficiency, a new record for single-junction solar cells under 1 sun illumination,” in *2011 37th IEEE Photovoltaic Specialists Conference*. IEEE, 2011, pp. 000 004–000 008.

[12] Qarony W., Hossain M. I., Hossain M. K., Uddin M. J., Haque A., Saad A., and Tsang Y. H., “Efficient amorphous silicon solar cells: characterization, optimization, and optical loss analysis,” *Results in physics*, vol. 7, pp. 4287–4293, 2017.

[13] Energy.gov, “Cadmium telluride,” 2022, retrieved July 27, 2022. [Online]. Available:https://www.energy.gov/eere/solar/cadmium-telluride

[14] Solar Power World, “Miasolé reaches 17.44% efficiency on commercial-sized cigs thin-film solar module,” 2021, retrieved July 27, 2022. [Online]. Available: https://www.solarpowerworldonline.com/2019/07/ miasole-reaches-17-44-efficiency-on-commercial-sized-cigs-thin-film-solar-module/

[15] O’regan B. and Grätzel M., “A low-cost, high-efficiency solar cell based on dye-sensitized colloidal tio 2 films,” *nature*, vol. 353, no. 6346, pp. 737–740, 1991.

[16] Atli A., Atilgan A., and Yildiz A., “Multi-layered tio2 photoanodes from different precursors of nanocrystals for dye-sensitized solar cells,” *Solar Energy*, vol. 173, pp.

752–758, 2018.

[17] Yildiz A., Chouki T., Atli A., Harb M., Verbruggen S. W., Ninakanti R., and Emin S., "Efficient iron phosphide catalyst as a counter electrode in dye-sensitized solar cells," *ACS Applied Energy Materials*, vol. 4, no. 10, pp. 10 618–10 626, 2021.

[18] Atli A., Atilgan A., Altinkaya C., Ozel K., and Yildiz A., "St. lucie cherry, yellow jasmine, and madder berries as novel natural sensitizers for dye-sensitized solar cells," *International Journal of Energy Research*, vol. 43, no. 8, pp. 3914–3922, 2019.

[19] Kocak Y., Atli A., Atilgan A., and Yildiz A., "Extraction method dependent performance of bio-based dye-sensitized solar cells (dsscs)," *Materials Research Express*, vol. 6, no. 9, p. 095512, 2019.

[20] Kocak Y. and Yildiz A., "Carminic acid extracted from cochineal insect as photosensitizer for dye-sensitized solar cells," *International Journal of Energy Research*, vol. 45, no. 11, pp. 16 901–16 907, 2021.

[21] Atilgan A., Kurtulus A. Y., Oktem M. F., and Yildiz A., "W-doped zno transparent conducting nanostructures synthesized by hydrothermal method," *Journal of Materials Science: Materials in Electronics*, vol. 32, no. 14, pp. 19 126–19 135, 2021.

[22] Atli A., Sutcu I., Yildiz Z. K., and Yildiz A., "Optimizing deposition parameters of dsscs composed of blue tio 2," *IEEE Journal of Photovoltaics*, vol. 11, no. 1, pp. 118–123, 2020.

[23] Becquerel E., "On electric effects under the influence of solar radiation," *Compt. Rend.*, vol. 9, p. 561, 1839.

[24] Einstein A., "Zur allgemeinen molekularen theorie der wärme," *Annalen der Physik*, vol. 319, no. 7, pp. 354–362, 1904.

[25] Tomaszewski P. E., "Jan czochralski—father of the czochralski method," *Journal of crystal growth*, vol. 236, no. 1-3, pp. 1–4, 2002.

[26] Raisbeck G., “The solar battery,” *Scientific American*, vol. 193, no. 6, pp. 102–111, 1955.

[27] Prince M., “Silicon solar energy converters,” *Journal of Applied Physics*, vol. 26, no. 5, pp. 534–540, 1955.

[28] Goetzberger A. and Hebling C., “Photovoltaic materials, past, present, future,” *Solar energy materials and solar cells*, vol. 62, no. 1-2, pp. 1–19, 2000.

[29] Nazeeruddin M. K., “Twenty-five years of low-cost solar cells,” *Nature*, vol. 538, no. 7626, pp. 463–464, 2016.

[30] Mardare D., Yildiz A., Girtan M., Manole A., Dobromir M., Irimia M., Adomnitei C., Cornei N., and Luca D., “Surface wettability of titania thin films with increasing nb content,” *Journal of Applied Physics*, vol. 112, no. 7, p. 073502, 2012.

[31] Serin T., Yildiz A., Uzun Ş., Çam E., and Serin N., “Electrical conduction properties of in-doped zno thin films,” *Physica Scripta*, vol. 84, no. 6, p. 065703, 2011.

[32] Nikolova M. P. and Chavali M. S., “Metal oxide nanoparticles as biomedical materials,” *Biomimetics*, vol. 5, no. 2, p. 27, 2020.

[33] Yildiz A., Lisesivdin S., Kasap M., and Mardare D., “High temperature variable-range hopping conductivity in undoped tio2 thin film,” *Optoelectronics and Advanced Materials-Rapid Communications*, vol. 1, no. 10, pp. 531–533, 2007.

[34] Singh M., Duklan N., Singh P., and Sharma J., “Synthesis and photocatalytic activity of anatase tio2 nanoparticles for degradation of methyl orange,” in *AIP Conference Proceedings*, vol. 1953, no. 1. AIP Publishing LLC, 2018, p. 030075.

[35] Dambournet D., Belharouak I., and Amine K., “Tailored preparation methods of tio2 anatase, rutile, brookite: mechanism of formation and electrochemical properties,” *Chemistry of materials*, vol. 22, no. 3, pp. 1173–1179, 2010.

[36] Amano F., Yamamoto A., and Kumagai J., “Highly active rutile tio2 for

photocatalysis under violet light irradiation at 405 nm," *Catalysts*, vol. 12, no. 10, p. 1079, 2022.

[37] Haggerty J. E., Schelhas L. T., Kitchaev D. A., Mangum J. S., Garten L. M., Sun W., Stone K. H., Perkins J. D., Toney M. F., Ceder G. *et al.*, "High-fraction brookite films from amorphous precursors," *Scientific reports*, vol. 7, no. 1, pp. 1–11, 2017.

[38] Wen P., Han Y., and Zhao W., "Influence of tio2 nanocrystals fabricating dye-sensitized solar cell on the absorption spectra of n719 sensitizer," *International Journal of Photoenergy*, vol. 2012, 2012.

[39] Holliman P. J., Mohsen M., Connell A., Davies M. L., Al-Salihi K., Pitak M. B., Tizzard G. J., Coles S. J., Harrington R. W., Clegg W. *et al.*, "Ultra-fast co-sensitization and tri-sensitization of dye-sensitized solar cells with n719, sq1 and triarylamine dyes," *Journal of Materials Chemistry*, vol. 22, no. 26, pp. 13 318–13 327, 2012.

[40] Ilić S. and Paunović V., "Characteristics of curcumin dye used as a sensitizer in dye-sensitized solar cells," *Facta universitatis-series: Electronics and Energetics*, vol. 32, no. 1, pp. 91–104, 2019.

[41] Gao P., Konrad D., Aghazada S., and Nazeeruddin M. K., "Molecular engineering of functional materials for energy and opto-electronic applications," *CHIMIA International Journal for Chemistry*, vol. 69, no. 5, pp. 253–263, 2015.

[42] Iftikhar H., Sonai G. G., Hashmi S. G., Nogueira A. F., and Lund P. D., "Progress on electrolytes development in dye-sensitized solar cells," *Materials*, vol. 12, no. 12, p. 1998, 2019.

[43] Gregg B. A., "Excitonic solar cells," pp. 4688–4698, 2003.

[44] Wu J., Lan Z., Lin J., Huang M., Huang Y., Fan L., Luo G., Lin Y., Xie Y., and Wei Y., "Counter electrodes in dye-sensitized solar cells," *Chemical Society Reviews*, vol. 46, no. 19, pp. 5975–6023, 2017.

[45] Maçaira J., Andrade L., and Mendes A., "Review on nanostructured photoelectrodes for next generation dye-sensitized solar cells," *Renewable and Sustainable Energy Reviews*, vol. 27, pp. 334–349, 2013.

[46] Sharma K., Sharma V., and Sharma S., "Dye-sensitized solar cells: fundamentals and current status," *Nanoscale research letters*, vol. 13, no. 1, pp. 1–46, 2018.

[47] Mandal S., Rao S., and Ramanujam K., "Understanding the photo-electrochemistry of metal-free di and tri substituted thiophene-based organic dyes in dye-sensitized solar cells using dft/td-dft studies," *Ionics*, vol. 23, no. 12, pp. 3545–3554, 2017.

[48] Calogero G., Calandra P., Irrera A., Sinopoli A., Citro I., and Di Marco G., "A new type of transparent and low cost counter-electrode based on platinum nanoparticles for dye-sensitized solar cells," *Energy & Environmental Science*, vol. 4, no. 5, pp. 1838–1844, 2011.

[49] Wang Y., Zhao C., Qin D., Wu M., Liu W., and Ma T., "Transparent flexible pt counter electrodes for high performance dye-sensitized solar cells," *Journal of Materials Chemistry*, vol. 22, no. 41, pp. 22 155–22 159, 2012.

[50] Tsai C.-H., Hsiao Y.-C., and Chuang P.-Y., "Investigation of electrochemically deposited and chemically reduced platinum nanostructured thin films as counter electrodes in dye-sensitized solar cells," *Coatings*, vol. 8, no. 2, p. 56, 2018.

[51] Iefanova A., Gautam U., Poudel P., Davoux D., Nepal J., Mallam V., Qiao Q., Logue B., and Baroughi M. F., "Low cost platinum counter electrode for dye-sensitized solar cells," in *2013 IEEE 39th Photovoltaic Specialists Conference (PVSC)*. IEEE, 2013, pp. 2716–2719.

[52] Wang Y.-C., Wang D.-Y., Jiang Y.-T., Chen H.-A., Chen C.-C., Ho K.-C., Chou H.-L., and Chen C.-W., "Fes2 nanocrystal ink as a catalytic electrode for dye-sensitized solar cells," *Angewandte Chemie*, vol. 125, no. 26, pp. 6826–6830, 2013.

[53] Hashmi G., Miettunen K., Halme J., Asghar I., Vahlman H., Saukkonen T., Huaijin Z., and Lund P., "Comparison of plastic based counter electrodes for dye

sensitized solar cells," *Journal of the Electrochemical Society*, vol. 159, no. 7, p. H656, 2012.

[54] Kim H. and Yang B. L., "Effect of seed layers on tio2 nanorod growth on fto for solar hydrogen generation," *International Journal of Hydrogen Energy*, vol. 40, no. 17, pp. 5807–5814, 2015.

[55] Wang H.-E., Chen Z., Leung Y. H., Luan C., Liu C., Tang Y., Yan C., Zhang W., Zapien J. A., Bello I. *et al.*, "Hydrothermal synthesis of ordered single-crystalline rutile tio 2 nanorod arrays on different substrates," *Applied Physics Letters*, vol. 96, no. 26, p. 263104, 2010.

[56] Wang W., Lin Y., Zhang G., Kang C., Pan Z., Zhong X., and Rao H., "Modification of compact tio2 layer by ticl4-ticl3 mixture treatment and construction of high-efficiency carbon-based cspbi2br perovskite solar cells," *Journal of Energy Chemistry*, vol. 63, pp. 442–451, 2021.

[57] Kalb J., Dorman J. A., Folger A., Gerigk M., Knittel V., Plüisch C. S., Trepka B., Lehr D., Chua E., Goodge B. H. *et al.*, "Influence of substrates and rutile seed layers on the assembly of hydrothermally grown rutile tio2 nanorod arrays," *Journal of Crystal Growth*, vol. 494, pp. 26–35, 2018.

[58] Liao M., Fang L., Xu C., Wu F., Huang Q., and Saleem M., "Effect of seed layer on the growth of rutile tio2 nanorod arrays and their performance in dye-sensitized solar cells," *Materials science in semiconductor processing*, vol. 24, pp. 1–8, 2014.

[59] Jin Z., Wang Y., Chen S., Li G., Wang L., Zhu H., Zhang X., and Liu Y., "Influence of a solution-deposited rutile layer on the morphology of tio 2 nanorod arrays and the performance of nanorod-based dye-sensitized solar cells," *RSC advances*, vol. 6, no. 13, pp. 10 450–10 455, 2016.

[60] Yuan T., Lu H., Dong B., Zhao L., Wan L., Wang S., and Xu Z., "Single-crystalline rutile tio2 nanorod arrays with high surface area for enhanced conversion

efficiency in dye-sensitized solar cells," *Journal of Materials Science: Materials in Electronics*, vol. 26, no. 3, pp. 1332–1337, 2015.

[61] Wan J., Tao L., Wang B., Zhang J., Wang H., and Lund P. D., "A facile method to produce tio2 nanorods for high-efficiency dye solar cells," *Journal of Power Sources*, vol. 438, p. 227012, 2019.

[62] Iraj M., Nayeri F. D., Asl-Soleimani E., and Narimani K., "Controlled growth of vertically aligned tio2 nanorod arrays using the improved hydrothermal method and their application to dye-sensitized solar cells," *Journal of Alloys and Compounds*, vol. 659, pp. 44–50, 2016.

[63] Ghoderao K. P., Jamble S. N., and Kale R. B., "Influence of reaction temperature on hydrothermally grown tio2 nanorods and their performance in dye-sensitized solar cells," *Superlattices and Microstructures*, vol. 124, pp. 121–130, 2018.

[64] Liang J., Zhang G., Yang J., Sun W., and Shi M., "Tio2 hierarchical nanostructures: hydrothermal fabrication and application in dye-sensitized solar cells," *AIP Advances*, vol. 5, no. 1, p. 017141, 2015.

[65] Pawar U. T., Pawar S. A., Kim J.-H., and Patil P. S., "Dye sensitized solar cells based on hydrothermally grown tio2 nanostars over nanorods," *Ceramics International*, vol. 42, no. 7, pp. 8038–8043, 2016.

[66] Ahmad M., Mohan V., and Murakami K., "Hydrothermal growth of bilayered rutile-phased tio2 nanorods/micro-size tio2 flower in highly acidic solution for dye-sensitized solar cell," *Journal of Sol-Gel Science and Technology*, vol. 73, no. 3, pp. 655–659, 2015.

[67] Feng Y., Zhu J., Jiang J., Wang W., Meng G., Wu F., Gao Y., and Huang X., "Building smart tio 2 nanorod networks in/on the film of p25 nanoparticles for high-efficiency dye sensitized solar cells," *RSC Advances*, vol. 4, no. 25, pp. 12 944–12 949, 2014.

[68] Yu C., Zhang J., Yang H., Zhang L., and Gao Y., "Enhanced photovoltaic conversion efficiency of a dye-sensitized solar cell based on tio2 nanoparticle/nanorod array composites," *Journal of Materials Research*, vol. 34, no. 7, pp. 1155–1166, 2019.

[69] Jiang W., Liu H., Yin L., Shi Y., Chen B., Jiang W., and Ding Y., "Fabrication of enhanced electron transport layer by laser scanning technology for dye-sensitized solar cells," *Electrochimica Acta*, vol. 176, pp. 1036–1043, 2015.

[70] Ahmed I., Fakharuddin A., Wali Q., Zainun A. R. B., Ismail J., and Jose R., "Mesoporous titania–vertical nanorod films with interfacial engineering for high performance dye-sensitized solar cells," *Nanotechnology*, vol. 26, no. 10, p. 105401, 2015.

[71] Shobana M., Balraju P., Kumar P. S., Muthukumarasamy N., Yuvakkumar R., and Velauthapillai D., "Investigation on the performance of nanostructure tio2 bi-layer as photoanode for dye sensitized solar cell application," *Sustainable Energy Technologies and Assessments*, vol. 52, p. 102295, 2022.

[72] Atli A. and Yildiz A., "Opaque pt counter electrodes for dye-sensitized solar cells," *International Journal of Energy Research*, vol. 46, no. 5, pp. 6543–6552, 2022.

[73] Naghibi S., Sani M. A. F., and Hosseini H. R. M., "Application of the statistical taguchi method to optimize tio2 nanoparticles synthesis by the hydrothermal assisted sol–gel technique," *Ceramics International*, vol. 40, no. 3, pp. 4193–4201, 2014.

[74] Liu B. and Aydil E. S., "Growth of oriented single-crystalline rutile tio2 nanorods on transparent conducting substrates for dye-sensitized solar cells," *Journal of the American Chemical Society*, vol. 131, no. 11, pp. 3985–3990, 2009.

[75] Nor A. M., Achoi M. F., Mamat M. H., Zabidi M. M., Abdullah S., and Mahmood M. R., "Synthesis of tio2 nanowires via hydrothermal method," *Japanese Journal of Applied Physics*, vol. 51, no. 6S, p. 06FG08, 2012.

[76] Lee C. H., Kim K. H., Jang K. U., Park S. J., and Choi H. W., "Synthesis of tio2

nanotube by hydrothermal method and application for dye-sensitized solar cell," *Molecular Crystals and Liquid Crystals*, vol. 539, no. 1, pp. 125–465, 2011.

[77] Liu X., Wang G., Zhi H., Dong J., Hao J., Zhang X., Wang J., Li D., and Liu B., "Synthesis of the porous zno nanosheets and tio2/zno/fto composite films by a low-temperature hydrothermal method and their applications in photocatalysis and electrochromism," *Coatings*, vol. 12, no. 5, p. 695, 2022.

[78] Feng X., Shankar K., Varghese O. K., Paulose M., Latempa T. J., and Grimes C. A., "Vertically aligned single crystal tio2 nanowire arrays grown directly on transparent conducting oxide coated glass: synthesis details and applications," *Nano letters*, vol. 8, no. 11, pp. 3781–3786, 2008.

[79] Nasir S., Hussein M. Z., Zainal Z., Yusof N. A., Zobir S. A. M., and Alibe I. M., "Potential valorization of by-product materials from oil palm: A review of alternative and sustainable carbon sources for carbon-based nanomaterials synthesis," *BioResources*, vol. 14, no. 1, pp. 2352–2388, 2019.

[80] Hitachi High-Tech GLOBAL, "New schottky fe-sem, su5000 | si news : Hitachi high-tech global," 2022, retrieved July 16, 2022. [Online]. Available: https://www.hitachi-hightech.com/global/sinews/technical_explanation/0644/

[81] Kalantar-zadeh K. and Fry B., *Nanotechnology-Enabled Sensors*. Springer Science & Business Media, 2007.

[82] Yun S., Lund P. D., and Hinsch A., "Stability assessment of alternative platinum free counter electrodes for dye-sensitized solar cells," *Energy & Environmental Science*, vol. 8, no. 12, pp. 3495–3514, 2015.

[83] Comsol, "Analyzing cyclic voltammetry at a microdisk electrode with simulation," 2022, retrieved July 20, 2022. [Online]. Available: https://www.comsol.com/blogs/ analyzing-cyclic-voltammetry-at-a-microdisk-electrode-with-simulation/

[84] Gamry, "www.gamry.com," 2022, retrieved July 20, 2022. [Online]. Available: https://www.gamry.com/assets/Uploads/Interface1000-Brochure.pdf

[85] Maiaugree W., Lowpa S., Towannang M., Rutphonsan P., Tangtrakarn A., Pimanpang S., Maiaugree P., Ratchapolthavisin N., Sang-Aroon W., Jarernboon W. *et al.*, "A dye sensitized solar cell using natural counter electrode and natural dye derived from mangosteen peel waste," *Scientific reports*, vol. 5, no. 1, pp. 1–12, 2015.

[86] Lee B., Buchholz D. B., and Chang R., "An all carbon counter electrode for dye sensitized solar cells," *Energy & Environmental Science*, vol. 5, no. 5, pp. 6941–6952, 2012.

[87] Tektronix, "I-v characterization of photovoltaic cells and panels using the keithley 2450 or 2460 sourcemeter® smu instrument," 2022, retrieved August 02, 2022. [Online]. Available: https://www.tek.com/en/documents/application-note/ i-v-characterization-photovoltaic-cells-and-panels-using-keithley-2450-or

[88] Fegade U., Lin Y.-C., Lin C.-C., Wu R.-J., Alshahrani B., Alshahrani T., Al-Ahmed A., Khan F., Khan M. T., Ahmad N. *et al.*, "Spinel oxide incorporated photoanode for better power conversion efficiency in dye-sensitized solar cells," *Optik*, vol. 247, p. 167976, 2021.

[89] Wang Y., Zhang L., Deng K., Chen X., and Zou Z., "Low temperature synthesis and photocatalytic activity of rutile tio2 nanorod superstructures," *The Journal of Physical Chemistry C*, vol. 111, no. 6, pp. 2709–2714, 2007.

[90] Khemthong P., Photai P., and Grisdanurak N., "Structural properties of cuo/tio2 nanorod in relation to their catalytic activity for simultaneous hydrogen production under solar light," *international journal of hydrogen energy*, vol. 38, no. 36, pp. 15 992–16 001, 2013.

[91] Lu H., Tian W., Guo J., and Li L., "Interface engineering through atomic layer deposition towards highly improved performance of dye-sensitized solar cells," *Scientific reports*, vol. 5, no. 1, pp. 1–12, 2015.

[92] Wong D. K.-P., Ku C.-H., Chen Y.-R., Chen G.-R., and Wu J.-J., "Enhancing electron collection efficiency and effective diffusion length in dye-sensitized solar

cells," *ChemPhysChem*, vol. 10, no. 15, pp. 2698–2702, 2009.

[93] Spurr R. A. and Myers H., "Quantitative analysis of anatase-rutile mixtures with an x-ray diffractometer," *Analytical chemistry*, vol. 29, no. 5, pp. 760–762, 1957.

[94] Yildiz A., Serin N., Kasap M., Serin T., and Mardare D., "The thickness effect on the electrical conduction mechanism in titanium oxide thin films," *Journal of Alloys and Compounds*, vol. 493, no. 1-2, pp. 227–232, 2010.

[95] Nath N. C. D., Lee H. J., Choi W.-Y., and Lee J.-J., "Electrochemical approach to enhance the open-circuit voltage (voc) of dye-sensitized solar cells (dsscs)," *Electrochimica Acta*, vol. 109, pp. 39–45, 2013.

[96] Lee K.-M., Chen P.-Y., Hsu C.-Y., Huang J.-H., Ho W.-H., Chen H.-C., and Ho K.-C., "A high-performance counter electrode based on poly (3, 4-alkylenedioxythiophene) for dye-sensitized solar cells," *Journal of Power Sources*, vol. 188, no. 1, pp. 313–318, 2009.

[97] Mary C., Senthilkumar M., Manobalaji G., and Babu S. M., "Surface-treated cu2znsns4 nanoflakes as pt-free inexpensive and effective counter electrode in dssc," *Journal of Materials Science: Materials in Electronics*, vol. 31, no. 20, pp. 18 164–18 174, 2020.

[98] Lisesivdin S., Demirezen S., Caliskan M., Yildiz A., Kasap M., Ozcelik S., and Ozbay E., "Growth parameter investigation of al0. 25ga0. 75n/gan/aln heterostructures with hall effect measurements," *Semiconductor science and Technology*, vol. 23, no. 9, p. 095008, 2008.

[99] Lisesivdin S., Yildiz A., and Kasap M., "Optimization of alloy composition, interlayer and barrier thicknesses in alxga1-xn/(aln)/gan high electron mobility transistors," *Optoelectronics and Advanced Materials-Rapid Communications*, vol. 1, no. 9, pp. 467–470, 2007.

[100] Antonelou A., Syrrokostas G., Sygellou L., Leftheriotis G., Dracopoulos V.,

and Yannopoulos S. N., “Facile, substrate-scale growth of mono-and few-layer homogeneous mos2 films on mo foils with enhanced catalytic activity as counter electrodes in dsscs,” *Nanotechnology*, vol. 27, no. 4, p. 045404, 2015.

[101] Moradi-Haji Jafan M., Zamani-Meymian M.-R., Rahimi R., and Rabbani M., “The effect of solvents and the thickness on structural, optical and electrical properties of ito thin films prepared by a sol–gel spin-coating process,” *Journal of Nanostructure in Chemistry*, vol. 4, no. 1, pp. 1–9, 2014.

[102] Duan X., Gao Z., Chang J., Wu D., Ma P., He J., Xu F., Gao S., and Jiang K., “Cos2–graphene composite as efficient catalytic counter electrode for dye-sensitized solar cell,” *Electrochimica Acta*, vol. 114, pp. 173–179, 2013.

[103] Chen X., Ding J., Li Y., Wu Y., Zhuang G., Zhang C., Zhang Z., Zhu C., and Yang P., “Size-controllable synthesis of nicose 2 microspheres as a counter electrode for dye-sensitized solar cells,” *RSC advances*, vol. 8, no. 46, pp. 26 047–26 055, 2018.

[104] Wu M.-S., Chung C.-J., and Ceng Z.-Z., “Cyclic voltammetric deposition of discrete nickel phosphide clusters with mesoporous nanoparticles on fluorine-doped tin oxide glass as a counter electrode for dye-sensitized solar cells,” *RSC advances*, vol. 5, no. 6, pp. 4561–4567, 2015.

[105] Jain V. K. and Kulshreshtha A. P., “Indium-tin-oxide transparent conducting coatings on silicon solar cells and their “figure of merit”,” *Solar Energy Materials*, vol. 4, no. 2, pp. 151–158, 1981.

[106] Fraser D. and Cook H., “Highly conductive, transparent films of sputtered in2-x sn x o 3- y,” *Journal of the Electrochemical Society*, vol. 119, no. 10, p. 1368, 1972.

[107] Gordon R. G., “Criteria for choosing transparent conductors,” *MRS bulletin*, vol. 25, no. 8, pp. 52–57, 2000.

[108] Haacke G., “New figure of merit for transparent conductors,” *Journal of Applied Physics*, vol. 47, no. 9, pp. 4086–4089, 1976.

[109] Atli, A., & Yildiz, A., “Hybrid TiO_2 nanorods combined with a buffer layer

for dye-sensitized solar cells", *Applied Solar Energy*, vol. 58, no. 3, 2022 (accepted).

[110] Yang C.-C., Zhang H. Q., and Zheng Y. R., "Dssc with a novel pt counter electrodes using pulsed electroplating techniques," *Current Applied Physics*, vol. 11, no. 1, pp. S147–S153, 2011.

[111] Koo B.-K., Lee D.-Y., Kim H.-J., Lee W.-J., Song J.-S., and Kim H.-J., "Seasoning effect of dye-sensitized solar cells with different counter electrodes," *Journal of Electroceramics*, vol. 17, no. 1, pp. 79–82, 2006.

[112] Yang J., Bao C., Zhu K., Yu T., Li F., Liu J., Li Z., and Zou Z., "High catalytic activity and stability of nickel sulfide and cobalt sulfide hierarchical nanospheres on the counter electrodes for dye-sensitized solar cells," *Chemical Communications*, vol. 50, no. 37, pp. 4824–4826, 2014.

[113] Yun S., Zhang H., Pu H., Chen J., Hagfeldt A., and Ma T., "Metal oxide/carbide/carbon nanocomposites: in situ synthesis, characterization, calculation, and their application as an efficient counter electrode catalyst for dye-sensitized solar cells," *Advanced Energy Materials*, vol. 3, no. 11, pp. 1407–1412, 2013.

[114] Latif H., Liu J., Mo D., Wang R., Zeng J., Zhai P., and Sattar A., "Effect of target morphology on morphological, optical and electrical properties of fto thin film deposited by pulsed laser deposition for mapbbr3 perovskite solar cell," *Surfaces and Interfaces*, vol. 24, p. 101117, 2021.

[115] Krishnapriya R., Praneetha S., Rabel A. M., and Murugan A. V., "Energy efficient, one-step microwave-solvothermal synthesis of a highly electro-catalytic thiospinel nico 2 s 4/graphene nanohybrid as a novel sustainable counter electrode material for pt-free dye-sensitized solar cells," *Journal of Materials Chemistry C*, vol. 5, no. 12, pp. 3146–3155, 2017.

[116] Qiao Q., "Carbon nanostructures as low cost counter electrode for dye-sensitized solar cells," *Solar Cells: Dye-Sensitized Devices*, p. 457, 2011.

[117] Elbohy H., Aboagye A., Sigdel S., Wang Q., Sayyad M. H., Zhang L., and Qiao

Q., “Graphene-embedded carbon nanofibers decorated with pt nanoneedles for high efficiency dye-sensitized solar cells,” *Journal of Materials Chemistry A*, vol. 3, no. 34, pp. 17 721–17 727, 2015.

[118] Murugadoss V., Arunachalam S., Elayappan V., and Angaiah S., “Development of electrospun pan/cos nanocomposite membrane electrolyte for high-performance dssc,” *Ionics*, vol. 24, no. 12, pp. 4071–4080, 2018.

[119] Hauch A. and Georg A., “Diffusion in the electrolyte and charge-transfer reaction at the platinum electrode in dye-sensitized solar cells,” *Electrochimica acta*, vol. 46, no. 22, pp. 3457–3466, 2001.

[120] Tang Z., Tang Q., Wu J., Li Y., Liu Q., Zheng M., Xiao Y., Yue G., Huang M., and Lin J., “Template-free synthesis of a hierarchical flower-like platinum counter electrode and its application in dye-sensitized solar cells,” *RSC advances*, vol. 2, no. 12, pp. 5034–5037, 2012.

[121] Bhardwaj S., Pal A., Chatterjee K., Rana T. H., Bhattacharya G., Roy S. S., Chowdhury P., Sharma G. D., and Biswas S., “Significant enhancement of power conversion efficiency of dye-sensitized solar cells by the incorporation of tio2–au nanocomposite in tio2 photoanode,” *Journal of materials science*, vol. 53, no. 11, pp. 8460–8473, 2018.

[122] Cho S. I., Sung H. K., Lee S.-J., Kim W. H., Kim D.-H., and Han Y. S., “Photovoltaic performance of dye-sensitized solar cells containing zno microrods,” *Nanomaterials*, vol. 9, no. 12, p. 1645, 2019.

[123] Saad P. S. M., Sutan H. B., Shariffudin S. S., Hashim H., and Noor U. M., “Tio2 thin film via sol-gel method: Investigation on molarity effect,” in *IOP Conference Series: Materials Science and Engineering*, vol. 99, no. 1. IOP Publishing, 2015, p. 012006.

[124] Lin J., Nattestad A., Yu H., Bai Y., Wang L., Dou S. X., and Kim J. H., “Highly

connected hierarchical textured tio 2 spheres as photoanodes for dye-sensitized solar cells," *Journal of Materials Chemistry A*, vol. 2, no. 23, pp. 8902–8909, 2014.

[125] Nonomura K., Vlachopoulos N., Unger E., Häggman L., Hagfeldt A., and Boschloo G., "Blocking the charge recombination with diiodide radicals by tio2 compact layer in dye-sensitized solar cells," *Journal of The Electrochemical Society*, vol. 166, no. 9, p. B3203, 2019.

[126] Thomas R., Mathavan T., Jothirajan M., Somaily H., Zahran H., and Yahia I., "An effect of lanthanum doping on physical characteristics of fto thin films coated by nebulizer spray pyrolysis technique," *Optical Materials*, vol. 99, p. 109518, 2020.

[127] Qudsia S., Dahlstrom S., Ahlang C., Rosqvist E., Nyman M., Peltonen J., Osterbacka R., and Smatt J.-H., "Role of surface coverage and film quality of the tio2 electron selective layer for optimal hole-blocking properties," *ACS omega*, vol. 7, no. 14, pp. 11 688–11 695, 2022.

[128] Sharif N. F. M., Shafie S., Kadir M. A., Hasan W. W., Mustafa M. N., and Samaila B., "The effect of titanium (iv) chloride surface treatment to enhance charge transport and performance of dye-sensitized solar cell," *Results in Physics*, vol. 15, p. 102725, 2019.

[129] Yamakata A. and Vequizo J. J. M., "Curious behaviors of photogenerated electrons and holes at the defects on anatase, rutile, and brookite tio2 powders: A review," *Journal of Photochemistry and Photobiology C: Photochemistry Reviews*, vol. 40, pp. 234–243, 2019.

[130] Ali H., Ismail N., Hegazy A., and Mekewi M., "A novel photoelectrode from tio2-wo3 nanoarrays grown on fto for solar water splitting," *Electrochimica Acta*, vol. 150, pp. 314–319, 2014.

[131] Hanaor D. A. and Sorrell C. C., "Review of the anatase to rutile phase